2013

Coupling between spin, lattice, and charge at the surface of complex transition metal compounds

Guorong Li
Louisiana State University and Agricultural and Mechanical College

COUPLING BETWEEN SPIN, LATTICE, AND CHARGE AT THE SURFACE OF COMPLEX TRANSITION METAL COMPOUNDS

A Dissertation

Submitted to the Graduate Faculty of the
Louisiana State University and
Agricultural and Mechanical College
in partial fulfillment of the
requirements for the degree of
Doctor of Philosophy

in

The Department of Physics and Astronomy

by
Guorong Li
B.S. in Physics, Peking University, 2007
August 2013

Acknowledgments

I am grateful to my advisor, Professor Ward Plummer, for providing me with the opportunity to carry out fundamental research in strongly correlated electronic system field in Louisiana State University. I want to thank him for the doors he has opened and the passion he has instilled. I greatly benefit from his detailed guidance and scientific insight throughout my Ph.D study. I sincerely appreciate his instructions and help in assisting me to finish my dissertation. I also thank Professor Jiandi Zhang and Professor Rongying Jin for the vivid explanations of physics puzzles and help in writing my papers and dissertation. I would also like to acknowledge my committee: Professor Mark Jarrell and Professor Patrick Gilmer for their advice and help on my dissertation. I would like to thank Dr. Von Braun Nascimento for the help in LEED theoretical calculation and experiment.

I send my thanks to collaborators: Prof. Vincent Meunier, Liangbo Liang at Rensselaer Polytechnic Institute for providing theoretical support; Dr. Qing Li, Dr. Minghu Pan at Oak Ridge National Laboratory for STM/S experiment; Prof. Vidya Madhavan, Dr.Yoshinori Okada, Daniel Walker, Wenwen Zhou at Boston College for liquid helium temperature STM/S experiments.

I feel grateful to my STM labmate Dr. Xiaobo He and Dr. Jisun Kim. I send my thanks to all my colleagues who were or are in LSU: Dr. Jing Teng, Dr. Zhaoliang Diao, Dr. Biao Hu, Dr. Yiming Xiong, Dr. Amar B. Karki, Jianneng Li, Zhenyu Diao, Chen Chen, Fangyang Liu, Dr. Junsoo Shin, Dalgis Mesa, Yi Li, Gaomin Wang, Lin Li, and Lina Chen. I benefit from the people I worked with at their user projects: Dr. Li Liu, Dr. P.C. Snijders, and Nan-Hsin Yu. I also thank LSU electronic shop and machine shop for their help: Randy Gould, Douglas smith, Donnie Olano, Vincent Vaughn, Brandon Amos, and so on. Last, I want thank

LSU faculties who taught me or asked me questions either in classroom, or in lab, or in presentation. I want thank all secretaries in LSU main office for helping me with paperwork and supporting me with all the activities I have in the department: to name a few, Arnell Nelson, Shemeka Ezeff, Ophelia Dudley. Thanks to physics department, thanks to Dr. Britt Thomas and Dr. Peter Kelleher at LSU Office of Intellectual Property and thanks to LSU.

I want to thank my girlfriend for her supports. But my final and most heartfelt acknowledgement must go to my parents. I greatly thank them for the endless love and supporting and caring for me all of my life.

Table of Contents

List of Tables

List of Figures

Abstract

Understanding and controlling the complexity that develops in complex transition metal compounds such as high-Tc superconductivity, "colossal" magnetoresistance in manganites, and heavy-fermion compounds, is one of the grand challenges of the 21st century. The exotic properties displayed by these compounds are closely related to the coexistence of nearly degenerate states, coupling simultaneously several active degrees of freedom such as the charge, lattice, orbital, and spin. In this work, we have focused on two systems, one is the newly discovered Fe-based superconducting compounds ((Ba, Ca)$(Fe_{1-x}Co_x)_2As_2$, $FeTe_{1-x}Se_x$) and the other one is the doped Ruddleden-Popper (RP) ruthenates ($Sr_3(Ru_{1-x}Mn_x)_2O_7$). The materials community was astonished by the discovery of superconductivity with a critical temperature exceeding 55 K in the iron-based superconductors in 2008. This new family of high T_c superconductors with layered structure without Cu has opened up a completely new venue for understanding not only high T_c superconductors but in general the coupling between lattice, charge, orbital and spin. While ruthenates is a prototype of strong correlated electron materials (CEMs) and Mn-doping in $Sr_3(Ru_{1-x}Mn_x)_2O_7$ have induced a rich coupled phase diagrams. We approach from the surface to study their geometric and electronic structure because the symmetry breaking offers great opportunities to tune the balance of the coupling. We applied Low energy electron diffraction (LEED) and its Intensity-voltage (I-V) analysis to quantitatively characterize the detail surface structure from momentum space. Then we used low and variable temperature scanning tunneling microscopy/spectroscopy (STM/S) to study surface electronic structure from real space. At last, spin-polarized density functional theory (DFT) calculations were utilized to enhance our understanding of the experimental data, thus providing a

new prospective of our discovery. Our results on the domain surface of $BaFe_2As_2$ show that the strong spin-lattice coupling at the surface results in the coexistence of structure and spin antiphase domain boundaries with C_2 symmetry. For the stripe surface of (Ba, Ca)$(Fe_{1-x}Co_x)_2As_2$, we determined the surface structure which is proved to be stabilized by bulk spin ordering through spin-lattice-charge coupling. Superconductivity has also been observed on stripe surface indicating a spatial-resolved coexisting of anti-ferromagnetic and superconducting order. On $FeTe_{1-x}Se_x$ system, we observed a nano-scale chemical phase separation of Te and Se atoms thus the optimally doped superconductor is chemically inhomogeneous but electronically homogeneous, in contrast to many CEMs. However, using STM on a different system, Mn-dopants in $Sr_3(Ru_{1-x}Mn_x)_2O_7$ were shown to homogeneously (random) distribute on the surface in micro-scale but maybe phase separated in macro-scale. We also discovered a left- and right- chirality of the structural rotation of MnO_6, thus to understand the correlation between the magnetic dopants. Our approach of using state-of-the-art surface techniques to study the manifestation of broken symmetry in these complex transition metal compounds, especially the iron pnictides and ruthernate offered the community a fresh look at the underlying physics.

Chapter 1
Introduction

1.1 Coupling between spin, lattice and charge

The past few decades have witnessed the discovery of new materials with exotic properties, which has led to an explosion experimental and theoretical activity. This is especially true for complex transition metal compounds. Cuprates show a zero resistance up to 138K [1] and newly discovered (2008) Fe-based superconductors have opened a completely new venue to the mystery High Temperature superconductors (HTSC) [2]. Manganites exhibit "colossal" magneto-resistance where several magnitude of resistance variation induced by small change of the magnetic field [3]. Heavy-fermions compounds host electrons which behave thousands times heavier than their actual mass [4]. Single layered ruthenate is a superconductor [5] while double layered ruthenate shows quantum critical behavior. Topological insulators show a metallic surface while bulk keeps insulating [6].

Many of these diverse properties have their origin in electron-electron interaction, whose strength categorized many of these compounds as correlated electron materials (CEMs). In convention metals, electrons travel freely and barely interact with each other. In contrast, in these complex materials the electrons interact with each other and equally important with several other degrees of freedom such as spin, lattice, and orbital. Figure 1.1 schematically illustrates the coupling in CEMs. In these materials, remarkable changes in physical properties occur with the application of an external stimulus due to the many competing low lying excited states. Such stimulus on one degree of freedom will affect the others, offering rich phase diagrams, illustrated in Fig. 1.2.

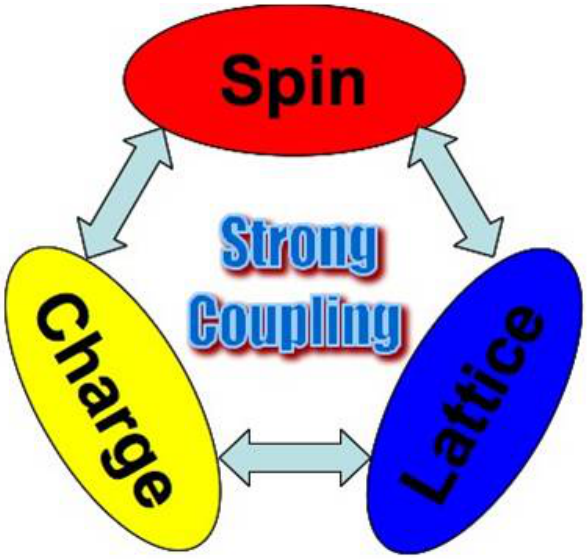

FIGURE 1.1. Coupling between lattice, charge and spin in CEMs.

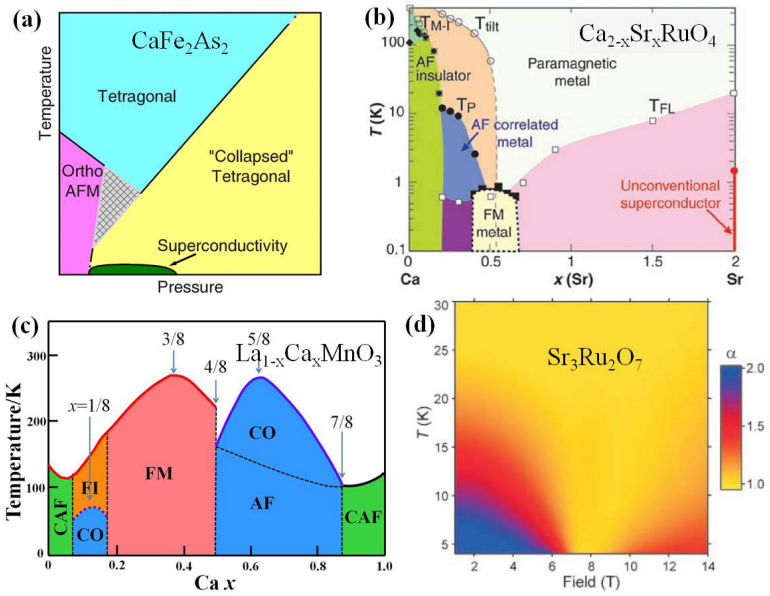

FIGURE 1.2. Phase diagrams of several examples of complex transitional metal compounds. (a): Temperature-Pressure phase diagram of $CaFe_2As_2$ [7]. (b): Temperature-Doping phase diagram of $Ca_{2-x}Sr_xRuO_4$ [9]. (c): Temperature-Doping phase diagram of $La_{1-x}Sr_xMnO_3$ [10]. (d) : Temperature-magnetic field phase diagram of $Sr_3Ru_2O_7$ [6]. Each panel is adapted from the reference cited

Applying external pressure is a powerful way to tune the lattice degrees of freedom, thus dramatically changing the system behaviors. Fig. 1.2a shows that superconductivity arises as the pressure suppress the orthorhombic anti-ferromagnetic (AFM) phase in $CaFe_2As_2$, one of the parent compounds in Fe-based superconductors [7]. When the application of a small pressure below 0.35 GPa, the tetragonal to orthorhombic structural transition temperature decreases with increasing pressure. For example, pressure suppresses the distinct resistivity signature of the high-temperature structural and magnetic phase transition from 170 K at ambient pressure to 128 K at 0.35 GPa [8]. When pressure is above 0.35 Gpa, there is no magnetic peak in neutron scattering scan and the c axis at low temperature collapses by as large as 1.0 $\mathring{A}$ while the in-plane lattice remains tetragonal, i. e. a non-magnetic collapsed tetragonal phase [7]. Superconductivity emerges with transition temperature up to 12 K for pressures between 0.23 and 0.86 GPa [7].

Substituting one element in the parent compound with another of different size but with the same valence (isovalent) induces disorder and strain into the system, which also tunes the properties. Fig. 1.2b is the phase diagram for single layer ruthenate with isovalent doping controlling the bandwidth rather than carrier concentration [9, 11, 12]. The system evolves from a superconducting (SC) state at x=2.0 to an AFM insulator at x=0.0. Between the end points are several distinct phases. The driving force for the different structural transitions observed in $Ca_{2-x}Sr_xRuO_4$ (CSRO) is the relative size of the Ca and Sr cations (R_{Ca} = 1.18 $\mathring{A}$, R_{Sr} = 1.31 $\mathring{A}$)[153, 14]. As Ca is added to Sr_2RuO_4 the lattice parameters shrink due to the smaller cation. The size of the RuO_6 octahedron appears robust throughout the family and the shrinking lattice induces a rotation in order to maintain a nearly uniform RuO_6 volume. Rotation of RuO_6 octahedral dramatically changes the electronic bands as well as the orbital occupation. Thus, it

provides a family of oxides where competition and complexity can be studied by such tuning.

If the element being substituted has a different valence than the host element, then there are two effects, one related to size difference and the other band filling (emptying). Figure 1.2c shows that replacing La^{3+} with Ca^{2+} not only induced lattice distortion but also doped additional holes, offering a rich phase diagram in polycrystalline $La_{1-x}Ca_xMnO_3$ [10]. Both the band-width and band filling are tuned by such doping. Overall the doping, the structure remains orthorhombic at all temperature and paramagnetic insulator at high temperature. This allows variable stable competing phases with very close energy at low temperature. In $0<x<0.1$, the super-exchange interaction leads to AFM order and the magnetic moment increases slightly with doping. For $0.1<x<0.2$, the system undergoes two transitions while cooling, one into ferromagnetic insulating states and the other go into a charge-ordering state. For $0.2<x<0.5$, the low temperature phase is ferromagnetic metal. For $0.5<x<0.9$, the system shows a charge-ordered insulator phase then follow with CE type AFM phase with a checkerboard arrangements of spins [10]. At the end of the doping phase diagram, for $0.9<x<1.0$, the system is an AFM insulator. Such a rich phase diagram indicates that the temperature and doping could greatly tune the system behaviors.

In the bilayer ruthenate $Sr_3Ru_2O_7$, an important tuning parameter towards a quantum critical point (QCP) is magnetic field. Fig. 1.2d shows that bilayer ruthenate $Sr_3Ru_2O_7$ exhibits behavior consistent with proximity to a metamagnetic (i.e., magnetic field-tuned) QCP [6]. The magnetic field is applied along c axis then high temperature resistivity near metamagnetic transition was measured. The resistivity was fitted with expression $\rho=\rho_{res}+A\times T^{\alpha}$ then the exponent $^{\alpha}$ value was obtained. The color plot shows the temperature and field evolution of the expo-

nent, α. The expected Fermi liquid has a α value of 2 and it is seen at the low field and temperature below 10 K. When the field is closed to metamagentic field of 7.8 T, $^{\alpha}$ close to 1 persists down to 4.5 K, and then rises again as the field increases. Such convenience of having a QCP for which the tuning parameter is the magnetic field attracts many activities in the community.

In these systems all the degrees of freedom are closely coupled so that there are multiple responses. For example, doping not only changes the carrier concentration but also induces lattice disorder. The challenge is how to experimentally isolate a single coupling channel and probe the relevant degree of freedom. In an ideal system we could have strong coupling between two of the degree of freedom. Experience shows that the coupling can be manipulated by creating an environment of broken symmetry, especially when the system exhibits properties associated with reduced dimensionality.

1.2 Systems with reduced dimensionality

The dimensionality is dictated by the size or the value in a certain direction of the object is several magnitudes larger/smaller compared to an appropriate length scale for the phenomena being discussed. Thus, a crystal may be viewed as three dimensional (3D) in size but two dimensional (2D) in its electronic transport property if there is a much less conductivity along c axis. Here reduced dimensionality refers to two, one or zero dimensions. For example, high T_c superconductor cuprate is a 2D system because the superconductivity occurs in the CuO_2 layer. The coherence length for a normal superconductor like Al (T_c=1.14 K) is isotropic and very long ($\sim 10^4$ $\mathring{A}$) while $HgBa_2Ca_2Cu_3O_{8+x}$ [15] has much shorter $\sim 50\mathring{A}$ in the plane and $\sim 10\mathring{A}$ perpendicular to the CuO_2, which is less than the 15.86 $\mathring{A}$ lattice spacing.

Ruddleden-Popper (RP) ruthenates $Sr_{n+1}Ru_nO_{3n+1}$ with $n = 1, 2, 3, ..., \infty$ is a prototype of strongly CEMs, which displays a range of dimensionality. RP series originally refer to compounds with the layered perovskite structures. Figure 1.3a shows crystal structures of RP ruthenates series. The key structure is the RuO_6 octahedron. The progression from n=1→2→3→ ... ∞ defines the number of Ru-O layers with a bridging oxygen. These materials show an interesting n-dependence of their physical properties and a wide range of complex behaviors including metal-insulator transition, giant magneto-resistance, superconductivity, ferromagnetism. AFM, and metamagnetism [121].

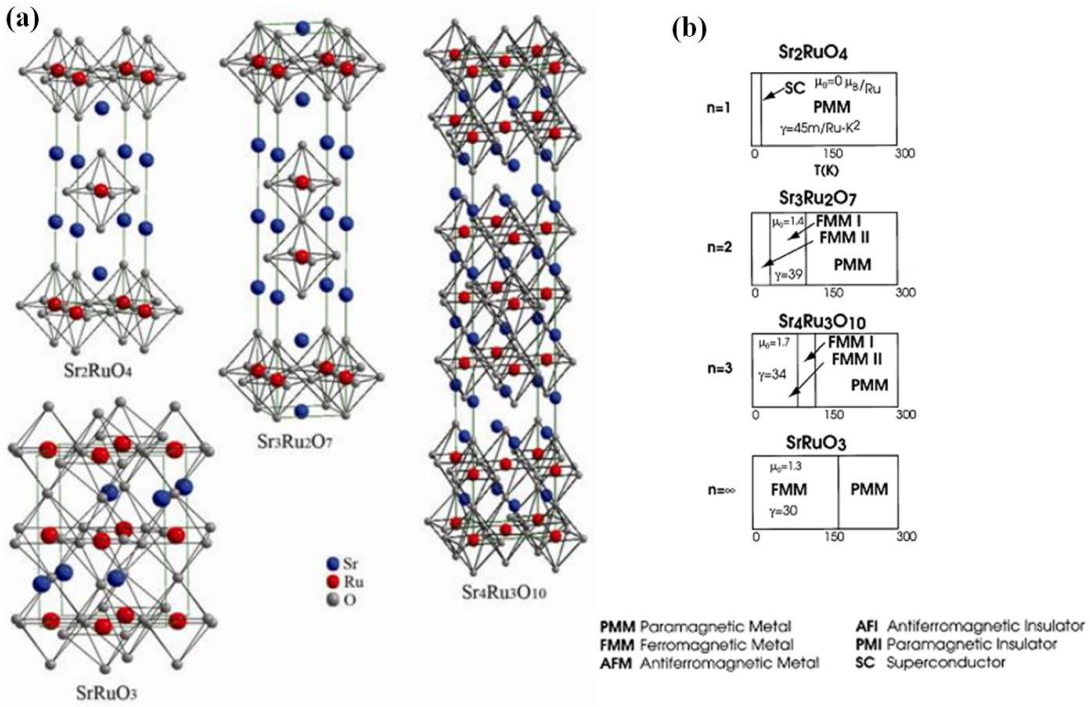

FIGURE 1.3. Crystal structure for RP series ruthenates and their phase diagrams.

Dimensionality becomes important throughout the series as the number of exchange interactions per transition metal ion systematically decreases from 6 for $n = \infty$ to 16/3 for $n = 3$, to 5 for $n = 2$, and finally 4 for $n = 1$. As a result, the exchange interactions and conductivity perpendicular to the Ru-O planes signifi-

cantly reduces as the in-plane conductivity of Ru-O layer increases. For example, when $n = \infty$, $SrRuO_3$ shows 3D behavior, but the resistivity anisotropy in the layered RP compounds incresed to c/ab > 500 in double layered Sr_2RuO_4. This n-dependence features impact the coupling throughout the series, giving rise to the extraordinarily systematic changes in magnetic and transport properties of these ruthenates. Fig. 1.3b summarizes the complex properties of RP ruthenate series in a schematic way.

1.3 Stimulus of creating a surface with broken symmetry

Creating a surface induces perturbation to local density of states (LDOS)

Creating a surface breaks translational symmetry thus inducing perturbation into the system. Either a green's function or a tight-binding Hamiltonian demonstrates the electronic structure at or near surface deviates from the bulk [17, 18]. For example, in tight-binding model, the local density of states, at some atomic site r:

$$n(E, r) = \sum_n |\psi_n(r)|^2 \delta(E - E_n) \tag{1.1}$$

The most common basis for the tight-binding Hamiltonian is the following localized atomic states

$$\langle m, R_i | n, R_j \rangle = \delta_{mn} \delta R_i R_j \tag{1.2}$$

For electron states of type m, n on atomic sites R_i and R_j, and

$$\langle m, R_i | H | n, R_j \rangle \neq 0 \tag{1.3}$$

Only if R_i-R_j is mall, i.e. R_i and R_j are near-neighbour lattice sites. For s-bands there is one electron s-state per atomic site and five d-bands electron states. To simplify the problem, only nearest-neighbour interaction have been included with the exception that of the *bcc* structure where the second-nearest-neighbours are also important. The first indication is that surface has less nearest neighbors than the bulk. In other words, the absence of half of the atomic sites and their electron states will alter the weightings of the combination of atomic orbitals.

Indeed, Fig. 1.4 shows the local density of states at and below (100) surface of a simple cubic s-band. It is clear that the band at the surface layer is narrower than bulk. This effect becomes minimal two layers below the surface. Calculation on (111) or (110) surface gives same conclusion. Surface expansion, plane by plane, means a decrease in nearest neighbor overlaps for the atoms near the surface. It is argued that this will further reduce the surface bandwidth compared to bulk-truncated surface. If the band-width decreases the system will be more correlated. Thus, the creating a surface impacts the local density of states (LDOS) at the top two layers of crystal, after which the LDOS will return to bulk. This disturbs the balance between competing ground states at the surface of CEMs, thus offering a different way to tune the system.

Surface phase transition

The creation of a surface will tip the coupling of the different degrees of freedom, resulting in a different phase diagram at the surface. Surface structural transitions include surface reconstruction, surface melting or surface segregation and a similar structural transition with the bulk but at different temperature. Magnetically, the surface might have a different Curie temperature [19]. Electronically, the surface might have charge density waves [20] or metal insulator transition at a different temperature than the bulk [21].

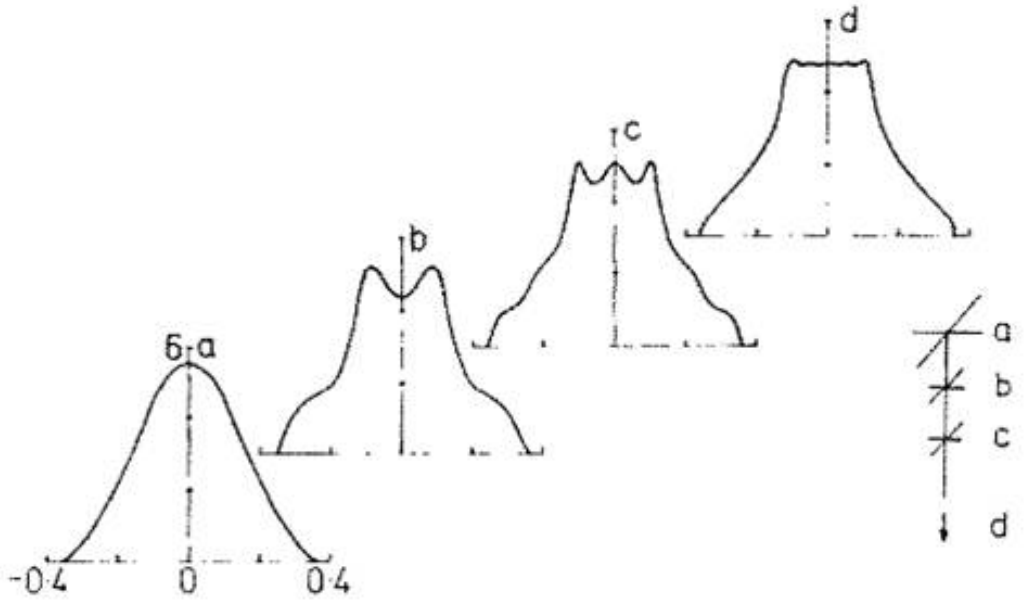

FIGURE 1.4. The local density of states at a (100) surface atom (z=5), sub-surface atoms and a bulk atoms (z=6) for a simple cubic tight binding s-band. (z is the number of nearest neighbors)

The disturbed balance is indicated in Fig. 1.5a by comparing surface and bulk phase diagram of $Ba(Fe_{1-x}Co_x)_2As_2$, one of the Fe-based superconducting compounds. One of the most intriguing aspects of these new compounds is the strong coupling between spin and lattice, offering a wonderful platform to study and manipulate their relationship. The parent compounds (no disorder induced by doping) of the $A122$ family (alkaline earth $(A)Fe_2As_2$) exhibit a coupled magnetic and structural transition from the low temperature antiferromagnetic orthorhombic phase to a high temperature paramagnetic tetragonal phase [22, 167, 24], which has the signature of being first order in the bulk. Doping the parent compound (Co for Fe) lowers the transition temperatures and at $x \sim 2.2\%$, there seems to be a tri-critical point beyond which the magnetic transition becomes second order [22, 167, 24]. The strong spin-lattice coupling in these systems [24, 25, 26, 27], along with the presence of a tri-critical point, creates an environment where either strongly first-order or nearly second-order phase transitions may be observed.

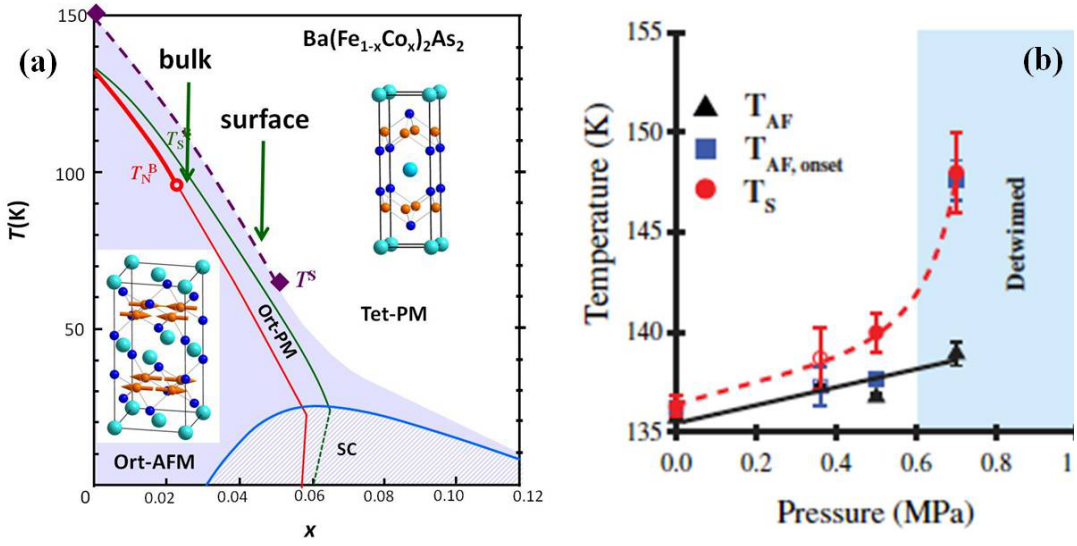

FIGURE 1.5. Surface and bulk temperature-doping phase diagram of $Ba(Fe_{1-x}Co_x)_2As_2$[28] and its bulk temperature-pressure phase diagram[26].

Surface properties mirror bulk under extremely conditions such as uniaxial pressure in this case. Fig. 1.5b shows a neutron scattering study of the effect of uniaxial pressure on the coupled structural/magnetic phase transition in $BaFe_2As_2$. Application of a critical pressure of 0.7 *MPa*, beyond the pressure needed to detwin the sample, dramatically increases the structural transition temperature ($\sim$147 K) accompanied by the onset of long-range magnetic ordering at the same temperature. Cleaving $Ba(Fe_{1-x}Co_x)_2As_2$ surface shows an appreciably higher structural transition temperature than the bulk [28]. Fig. 1.5a also show the proposed surface phase diagram from surface technique electron energy loss spectroscopy (EELS) measurements on the temperature dependence of two phonon modes for two compositions of $Ba(Fe_{1-x}Co_x)_2As_2$ with $x = 0$ and $x = 0.05$. The rate of change of phonon frequency with temperature is gigantic, two orders of magnitude larger than in the bulk. This behavior cannot be explained using conventional models of anharmonicity or electron-phonon coupling; instead, it requires that a large surface spin-charge-lattice coupling be included. Furthermore, the higher surface-

phase-transition temperature driven by surface stabilization of the low temperature orthorhombic phase seems to turn the first-order transition (bulk) into the second-order type, equivalent to what is observed in the bulk by applying a uniaxial pressure.

Thus, creating a surface by cleaving these layered materials is a controlled way to tip the balance between competing phases, providing a unique opportunity to study the subtle aspects of the interactions between lattice,spin and charge.

1.4 Surface tools: STM, LEED, and EELS

Surface techniques have proven to be extremely useful in study of complex transition metal compounds. In last 20 years, many advanced and complementary surface techniques, such as Scanning Tunneling Microscopy/Spectroscopy (STM/S) [29], Low Energy Electron Diffraction (LEED), Angle Resolved Photoemission Spectroscopy (ARPES) [30], Electron Energy Loss Spectroscopy (EELS) [31] etc., have played remarkable roles in understanding of CEMs in conjunction with bulk sensitive probes such as neutron scattering and transport. STM is able to image the surface topography in atomic resolution as well as probe the local electronic structure using STS. LEED allows a momentum space diffraction pattern which contains information about the geometric symmetry of the surface as well as detail surface structure using its intensity *vs* voltage (I-V) analysis. ARPES is capable of probing the electronic structure below Fermi surface with momentum resolution. Last, EELS is able to see the lattice dynamical behavior and electronic properties from the probing of phonon modes and Drude weight. They are complementary to each other and the combination of two has shown a great opportunity to investigate the physics problem from all aspects. For example, the contribution from both ARPES and STM/S studies has tremendously advanced the studies of the

electronic structures and properties of cuprates including superconducting gap and pairing symmetry, and electronic inhomogeneous [29, 30].

1.4.1 Combination of STM, LEED and first-principle calculation: example of Sr_2RuO_4

The combination of STM and LEED has successfully clarified the geometric and electronic structure at the surface of Sr_2RuO_4 (See Fig. 1.2b) [32]. Fig. 1.6 shows the single layer ruthenate crystal structure without any distortion, i.e. bulk truncated. The termination plane is Sr-O layer since the bonding of RuO_6 is strongest. Fig. 1.6d shows a top view of the bulk-truncated surface and with tetragonal (1×1) unit cell. However, the surface is different from the bulk and reconstructed with $(\sqrt{2}\times\sqrt{2})$R45° order. LEED pattern (Fig. 1.6b) shows additional fractional spots, which correspond to $(\sqrt{2}\times\sqrt{2})$R45° order. Certain fractional spots were extinct at all energies, presenting glide line symmetry. The surface has a *p4gm* plane group symmetry, which is associated with octahedral rotation. Thus, a top view of the surface structure in Fig. 1.6e would be expected with two identical Sr sites and two octahedral sites in one $(\sqrt{2}\times\sqrt{2})$R45° surface unit cell, where the left-handed site in the corner and the right-handed site in the center. This structure is different from the bulk, which does not have octahedral rotation.

STM images (Fig. 1.6c) have a C_{4v} symmetry topography with half of the Sr atoms visible and the other half invisible. Thus, the surface unit cell is the $(\sqrt{2}\times\sqrt{2})$R45° green square rather than the (1×1) red square, consistent with the schematic view in Fig. 1.6e. Since STM does not reveal subsurface atomic information, a quantitative analysis of the LEED beam intensity as a function of beam voltage was undertaken. This analysis can tell a detail surface structure. Pendry R_p factor was used to measure how good the fitting between theoretical IV curves and experimental data. R_p less than 0.3 represents a good fitting. The best fit with

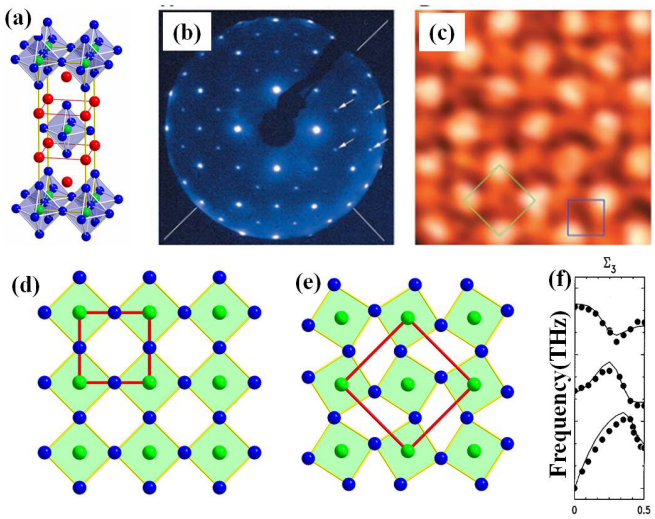

FIGURE 1.6. Surface structure of Sr_2RuO_4. (a) bulk crystal structure (b) LEED pattern and (c) STM topography. (d) Bulk-truncated surface top view. (e). Actual surface structure with octahedral rotation in ort-(1×1) surface unit cell. (f) The phone mode associate with octahedral rotation.

R-factor=0.16 to experimental spectra was obtained for a surface structure with the octahedra rotated by 9° ± 3° around the c axis. However, there is no buckling of Sr atoms thus the mystery is why Sr atoms in the $(\sqrt{2}\times\sqrt{2})$R45° unit cell at STM topography are different. In the chapter 6 of this thesis, we will further discuss this issue.

The static structure at the surface is actually the displacement pattern of the Σ3 bulk phonon mode at the zone boundary [33]. The Σ3 bulk phonon branches, ends at the (0.5, 0.5, 0) zone boundary, is the mode corresponding to RuO_6 rotation around c. In Fig. 1.6f, the bulk phonon dispersion shows a softening of the mode at the zone boundary. Due to the soft mode behavior of the Σ3 RuO_6 rotational mode, the surface reconstruction is attributed to the freezing of the Σ3 mode at the surface. Theoretically, the optimized structure for a nonmagnetic surface is a surface layer with octahedra rotated by 6.5° (Fig. 1.7a). This reconstruction, driven by compressive strain in the RuO_2 layers, lowers the energy by 14 meV per formula unit (f.u.). The FM ordering stabilizes the distortion further and increases

the rotation angle to 9° (Fig. 1.7) to gain additional energy of 51 meV/f.u. The ferromagnetic (FM) ground state has an exchange splitting of 0.5 eV for Ru 4d bands at the surface and the magnetic moment on each Ru atom is 1.0 μ_B (Bohr magneton). Thus, the surface is FM ordered. A STS study at this surface with a mK STM indicates that the surface has no superconducting gap which is possible killed by the FM ordering, see Fig. 1.7b [34].

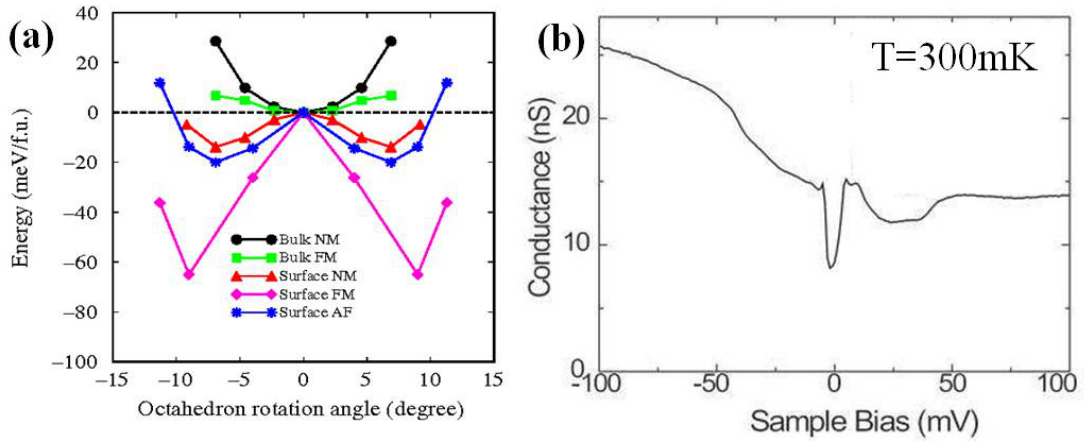

FIGURE 1.7. Surface electronic properties of Sr_2RuO_4. (a) DFT calculation shows that an FM ordered surface has lowest energy when octahedral rotation is 9°, which is the exactly angle determined from LEED IV analysis [32]. (b) a mK STM spectroscopy shows no superconducting gap at such surface [34]

1.4.2 Combination of STM, LEED, and EELS and first principle calculation: example of $(Sr_{2-x}Ca_x)RuO_4$

While the Sr-based single layer ruthenate is always metallic with a ferromagnetic component, the Ca-based ruthenates often involve metal-to-insulator (MIT) transitions and show antiferromagnetic instabilities. A combination of these two systems leads to exotic behavior as shown in Fig. 1.2b bulk phase diagram. Ca^{2+} replacement of Sr^{2+} gradually enhances the rotational and tilt distortion of the RuO_6 octahedra, starting with a tetragonal *I4/mmm* structure for Sr_2RuO_4, leading to an *I41/acd* structure for $Ca_{1.5}Sr_{0.5}RuO_4$, and ending with an orthorhombic *S-Pbca* structure for Ca_2RuO_4 [9]. The surface of Sr_2RuO_4 has been shown octahedral

rotation which is absent in the bulk. The octahedra in the bulk of $Ca_{1.9}Sr_{0.1}RuO_4$ is both rotated and tilted.

Bulk studies have demonstrated that the Mott transition in the Ca-rich doping regime is intimately related to a structural transition. When the system changes from a metallic to a Mott insulating phase on cooling, a concomitant structural transition to a more distorted orthorhombic phase is observed in the bulk. In sharp contrast, a combination of LEED, STM and EELS show that the Mott transition on a freshly cleaved surface of $Ca_{1.9}Sr_{0.1}RuO_4$ occurs without an accompanying lattice distortion [21]. Thus, surface has shown a purely electronic, Mott metal-to-insulator transition.

Figure 1.8a illustrates that the bulk MIT occurs at T_c = 154 K (c: critical), as shown by the abrupt change of the bulk electrical resistivity, whereas the surface transition occurs at $T_{c,s}$ =130 K (s, surface), as indicated by the opening of the energy gap measured by scanning tunneling spectroscopy (STS). Figure 1.8b shows data extract from EELS spectra indicating a sudden drop of the Drude weight accompanied by an energy shift, a rapid increase in intensity, and an abrupt linewidth reduction of the surface phonon at the temperature $T_{c,s}$ = 130 K. All of above are hallmarks of a surface Mott MIT. The surface MIT temperature is more than 20 K lower than T_c (154 K) in the bulk.

This finding is counterintuitive, because the conventional picture suggests that e-e correlation effects should be stronger at the surface than in the bulk as a result of the reduce band width (discussed earlier), thus stabilizing the Mott insulating phase and pushing the Mott transition to higher temperatures at the surface as compared to the bulk. The bulk first-order Mott MIT in $Ca_{1.9}Sr_{0.1}RuO_4$ is accompanied by an abrupt lattice distortion. The difference of tilt angle in the bulk from low temperature cross bulk MIT transition to high temperature is around $\sim 4^\circ$

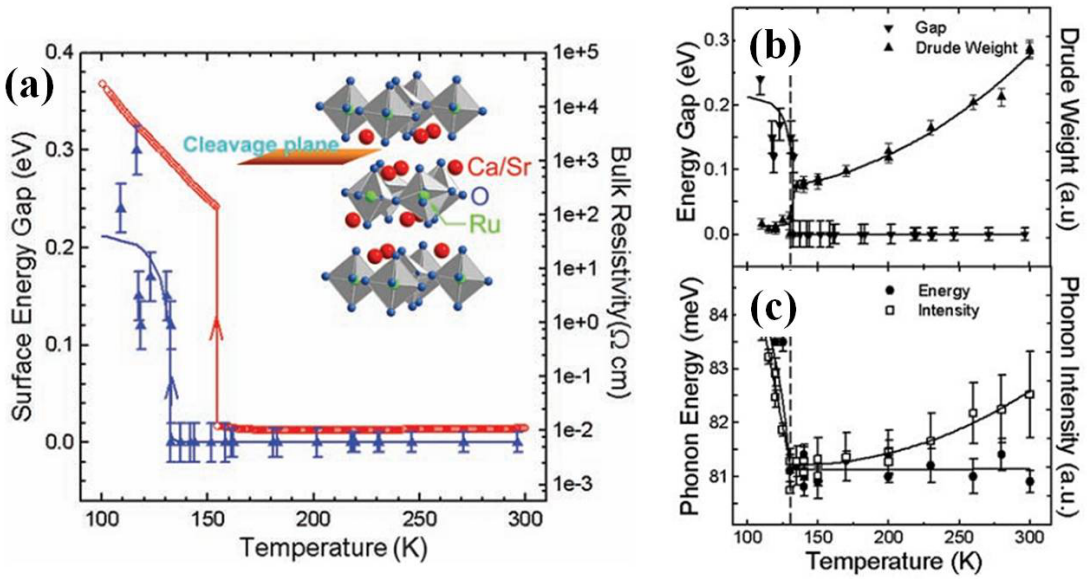

FIGURE 1.8. Electronic driven surface MIT transition in $Ca_{1.9}Sr_{0.1}RuO_4$ [21].(a): T dependence of bulk resistivity curve and surface energy gap. (b): T dependence of the energy gap determined by the STS spectra and the Drude weight obtained from the HREELS spectra and (c): T dependence of the energy and intensity of the optical phonon measured with HREELS at the surface of $Ca_{1.9}Sr_{0.1}RuO_4$.

while rotation angle keeps nearly constant. The surface lattice structure can be determined by LEED I-V analysis.

LEED pattern for $Ca_{1.9}Sr_{0.1}RuO_4$ in Fig. 1.9 shows a single glide line compare to LEED pattern for Sr_2RuO_4, indicating a $p(1\times1)$ [001] surface of a bulk-terminated orthorhombic structure. This orthorhombic structure (with *Pbca* space group symmetry) is characterized by a static tilt and rotational distortions of RuO_6 octahedra from the simple cubic perovskite phase. However, the analysis of the LEED I-V data shows that surface structure remains static across both the bulk and surface MIT except for a very gradual thermal relaxation. Thus, the MIT observed from STS and EELS is purely driven by e-e interactions.

As shown in Fig. 1.9b, the largest surface relaxation is the inward motion of the top Ca/Sr ions (which remains the same at both high and low temperature). This relaxation impedes the structural transition that occurs in the bulk at T_c. A first

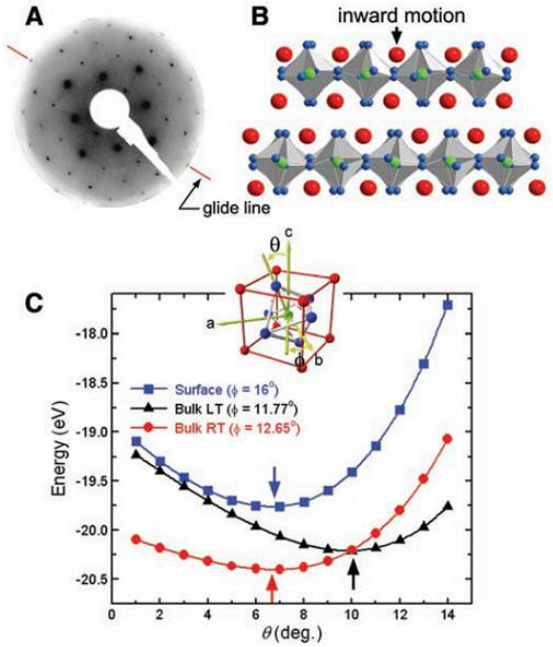

FIGURE 1.9. Surface structure of $Ca_{1.9}Sr_{0.1}RuO_4$. (a): LEED pattern at RT at 170 eV. (b). Schematic view of determined surface structure with 0.13 $\AA$ Ca inward motion. (c): The calculated total energy versus RuO_6 tilt angle for three different lattice structures

principle calculation has confirmed two stable bulk lattice structures in Fig. 1.9c; one with a tilt angle of $\sim 6.5^\circ$ for the metallic phase and the other with a tilt angle of $\sim 10^\circ$ for the insulating phase. To simulate the situation of the surface, an enhanced buckling of the Ca/Sr-O plane is included in a bulk calculation. As shown in Fig. 1.9c, this enhanced buckling pins the tilt angle at $\sim 7^\circ$, making the increased tilt energetically unfavorable and inhibiting the structural transition.

Finally, the surface phase diagram of $Ca_{1-x}Sr_xRuO_4$ is shown in Fig. 1.10. Surface electronic Mott transition tempeature is higher than bulk transition temperature for systematically increase the doping. Where between the surface and bulk transition temperature, it is a phase associated with tilt instability [35].

In summary, we have shown examples of using STM, LEED, EELS and first principle calculation to study the exotic behaviors of transitional metal compounds. Another important tool is angle resolved photoemission spectroscopy which could

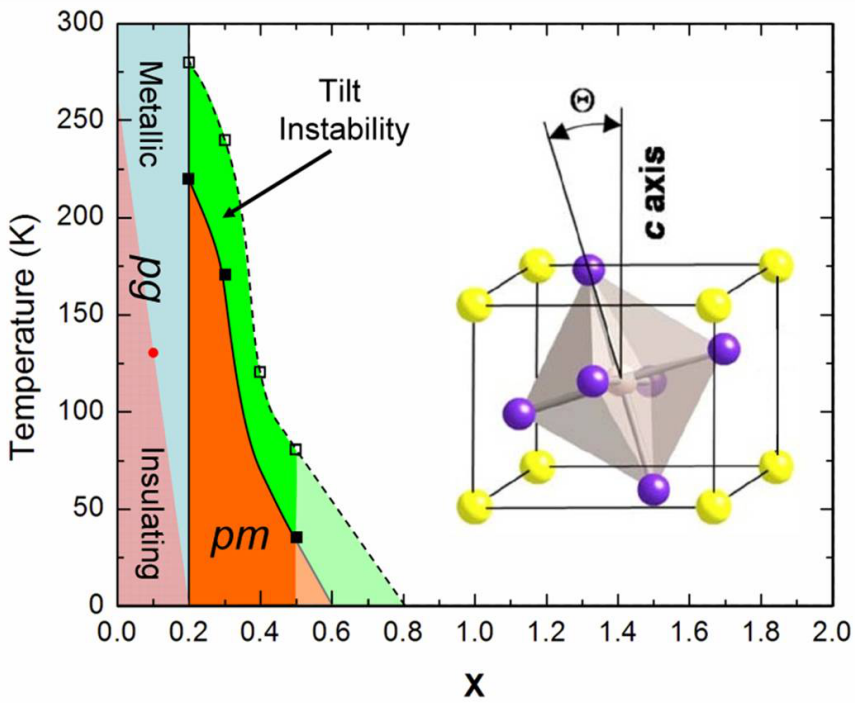

FIGURE 1.10. Surface phase diagram of $Ca_{1.9}Sr_{0.1}RuO_4$. Inset shows the tilt distortion.

image the Fermi surface in momentum space for the filled states. STS imaging provides a real-space quasi-particle interference pattern at both above and below surface, thus as a complementary tool to study the electronic structure of the materials.

1.5 Focus of this thesis

I have explored four different layered transitional metal compounds: three are the newly discovered Fe-based superconducting compounds including $FeTe_{1-x}Se_x$, $Ca(Fe_{1-x}Co_x)_2As_2$ and $Ba(Fe_{1-x}Co_x)_2As_2$; the other one is the doped Ruddleden-Popper (RP) ruthenates $Sr_3(Ru_{1-x}Mn_x)_2O_7$. All show rich phase diagrams with competing phases indicating the coupling between spin, lattice and charge. One of the first issues for surface studies is whether an atomic flat clean surface can be prepared. Both the Fe-based superconducting compounds and RP ruthenates

are layered structure, thus the samples can be cleaved between the weak bonded layers.

1.5.1 Fe-based superconducting compounds

Figure 1.11a shows structural models for the most common four families of Fe-based superconductors, "1111"(i. e. LaFeAsO), "122" (i. e. $BaFe_2As_2$), "111" (i. e. LiFeAs) and "11" (i. e. As free system, FeSe) [37]. Structurally, they share the common building block FeX trilayer consisting a square array of Fe sandwiched between two checkerboard layers of X plane, where X = As, P, S, Se, or Te, see Fig. 1.11b. These tri-layers are separated by intermediate layers consisting of alkali, alkaline-earth, or rare-earth atoms and oxygen/fluorine. Like CuO_2 layer in cuprate, the FeX tri-layer is the superconducting layer, thus it is the key structure.

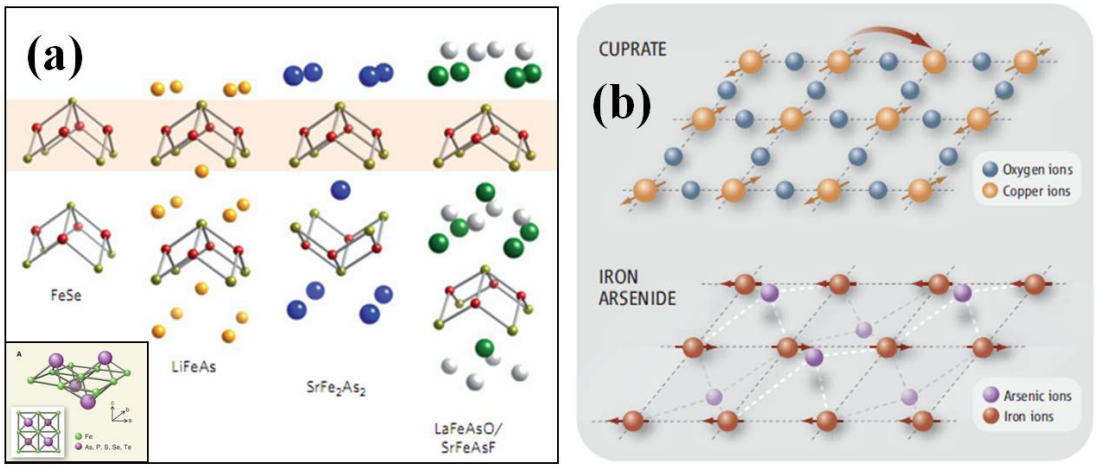

FIGURE 1.11. (a) The family of Fe-based superconducting compounds, inset shows the FeX structure. (b) Comparison of Fe-based superconducting compounds to Cuprate. Figures are adapted from reference [36, 37, 38].

Similar to cuprates, Fe-based superconductors are derived from AFM ordered non-superconducting parent compounds (see Fig.1.12). This AFM order forms below a structural transition at a temperature $T_s \sim$ 150 K - 200 K depending on the compound, and is apparent in many probe techniques [39]. To become superconducting, these parent compounds must be doped, typically by substitution of

A (e.g. by K) or substitution of Fe (e.g. by Co) in $A\mathrm{Fe_2As_2}$ (A = Ba, Sr, Ca), leading to T_c currently as high as 38 K and 20 K respectively [40, 41]. Doping not only changes carriers' concentrations, but also suppresses AFM order to induce superconductivity. The superconductivity typically arise as the AFM transition vanishes in "1111" but can be coexist in "122" system, suggesting the competition between the two states.

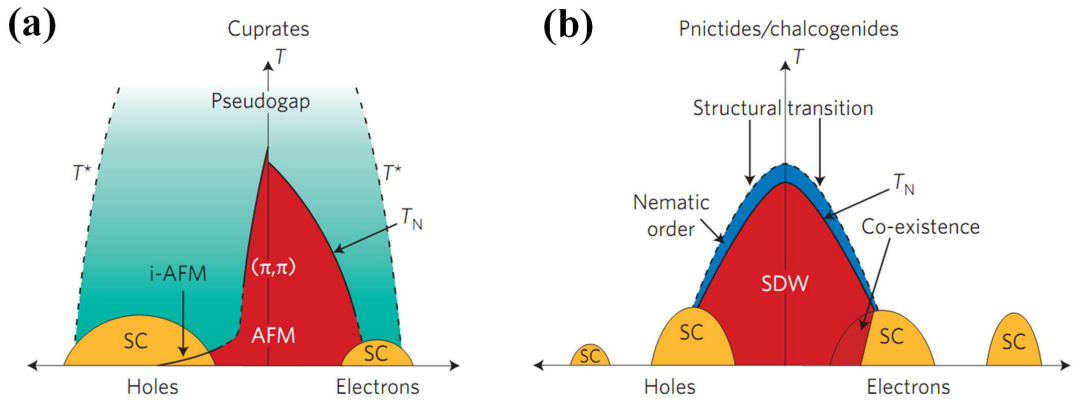

FIGURE 1.12. Schematic phase diagrams of the cuprates (a) and Fe-based SC compounds (b) on hole- or electron-doping. Figure adapted from reference [42]

However, as more data becomes available for the iron-based compounds, it is becoming clear that the members of this family behave rather differently from the cuprates. The AFM ground state of the Fe-based parent compounds is metallic but Mott insulating for the cuprates. The small magnetic moments [43] and the characteristic of electronic structure probed by photoemission measurements [44] indicate that the Fe bands are like an itinerant metal not localized as in the cuprates. While cuprates such as $\mathrm{La_{2-x}Sr_xCuO_4}$ undergo a structural transition [45], there is no evidence for the coupling between structure and AFM ordering. In iron based compounds, there is complex coupling between lattice and spin degrees of freedom: a structural transition from high temperature tetragonal to a low

temperature orthorhombic phase is always accompanied by a magnetic transition within a narrow temperature window.

This thesis, on compounds (Ba,Ca)$(Fe_{1-x}Co_x)_2As_2$ using scanning tunneling microscopy (STM) and low energy electron diffraction (LEED), reveals two surface phases: (1×2) and $(\sqrt{2}\times\sqrt{2})$R45° surfaces. STM reveals π-phase shifted domains between $(\sqrt{2}\times\sqrt{2})$R45° structures. The symmetry of the associated domain walls is lower than the lattice symmetry expected from the bulk or seen by STM within a single domain. It is argued in this thesis that this is a result of the strong coupling between AFM ordered spins and electrons at the surface, which causes the coexistence of an antiphase spin domain boundary with the antiphase structural boundary. While at stripe phase, the termination is a 50% A layer for both compounds with qualitatively the same structure. Compared to bulk, the surface A layer has a large inward relaxation ($\sim 0.5\mathring{A}$), and the underneath As-Fe_2-As layer displays a significant buckling. The calculations show that the stripe-ordered surface is stabilized by the bulk spin ordering through the spin-lattice coupling. Further, the superconducting gap was found on the same surface at low temperature, indicating a coexisting of AFM and SC order.

1.5.2 Mn-doped $Sr_3Ru_2O_7$

As Figure 1.3 illustrated, ruthernate family show a dimensionality dependence of their physical properties and a wide range of complex and unusual phenomena including metal-insulator transition, superconductivity, quantum phase transition, giant magnetoresistance, ferromagnetism, antiferromagentism and electronic nematic behavior [5, 49, 50, 51, 52]. The bi-layer and metallic $Sr_3Ru_2O_7$ is of particular interest due to the observation of quantum critical behavior (see Fig. 1.2d) related to its metamagnetic transition and strong magnetic fluctuations [6]. Applying a magnetic field can tune the properties of $Sr_3Ru_2O_7$. In Fig. 1.13(a) shows

the metamagenestim behavior. For magnetic fields applied in the ab plane, a rapid superlinear rise in the magnetization is seen with a characteristic field of approximately 5.5 T [47]. This field is close to the quantum critical point in Fig. 1.2d and the critical fluctuation near the QCP plays important role in determine the properties of metallic state in Fig. 1.13a. Figure 1.13b shows that near the vicinity of a metamagnetic quantum critical point, the high-purity strontium ruthenate $Sr_3Ru_2O_7$ possesses a large magnetoresistive anisotropy [46]. It is argued that such one unidirectional electronic behavior is consistent with the existence of an electronic nematic fluid [46]. Further, STM experiments explore the local spectroscopic signatures of metamagnetic criticality in $Sr_3Ru_2O_7$ [48]. The singular feature in the tunneling spectrum was found close to the Fermi level, shown in Fig. 1.13c. The general trend is for spectral weight to be transferred asymmetrically from the peaks at -3 mV and +4 mV into smaller features near -1 mV and 2 mV, respectively. When the field is higher than 8 T, the trend changed and the minimum of LDOS at E_F are quickly been filled.

Doping offers another way to tune the properties of $Sr_3Ru_2O_7$. While doping with a few percent of non-magnetic ions such as Ti only changes the carrier concentration, replacing a few percent of Ru with another transition-metal ion like Mn which is magnetic, results a MIT at T_{MIT} from metallic character at high temperatures to insulating behavior at low temperature. In this thesis, the surface of $Sr_3(Ru_{1-x}Mn_x)_2O_7$ was investigated using LEED and STM/S for x=0.0, 0.06 and 0.16. The LEED patterns were consistent with a surface with both rotation and tilt, where the rotation seems to be independent of x but the tilt decrease rapidly with increasing x. STM was utilized to imaged the Mn sites which exhibited a right- and left- hand chirality expected from the bulk orthorhombic unit cell. Statistically the location of the Mn is random and there is no correlation between the

right and left rotated Mn sites. STS shows that the surface is metallic at all values of x, in contrast to the bulk. A careful examination of the STM images shows a C_{2v} symmetry compared to C_{4v} in the bulk, which is due to the tilt. The manifestation of the tilt induced broken symmetry on the bias dependent STM and STS images will be discussed.

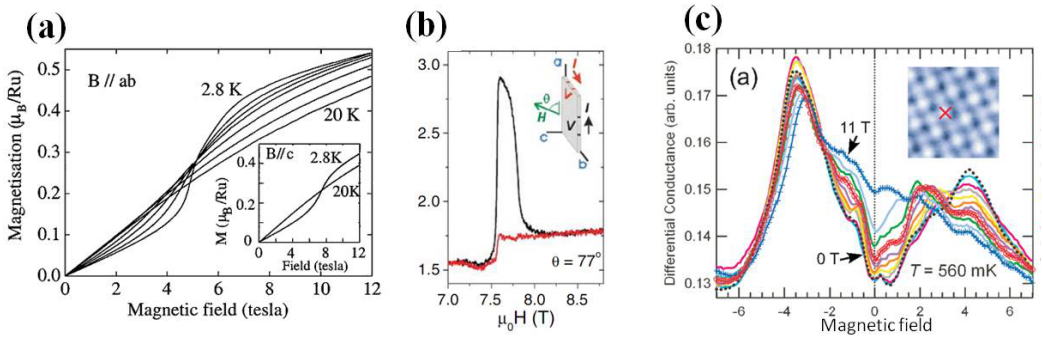

FIGURE 1.13. (a) The magnetization of single crystal $Sr_3Ru_2O_7$ for magnetic fields applied in the ab plane. (b) The magnetoresistive anisotropy measured from a and b direction. (c) STM spectroscopies taken under different magnetic field up to 11T. Figures are adapted from reference [46, 47, 48].

Chapter 2

Experimental Techniques and Analytical Procedures

Two main surface techniques were used in this thesis. One is scanning tunneling microscopy/spectroscopy (STM/S) and the other is low energy electron diffraction (LEED). STM/S is able to probe the real-space local symmetry and electronic structure while LEED with its intensity versus voltage (I-V) analysis are able to probe the lattice symmetry and structure, see Fig. 2.1. They are complementary to each other that STM/S sees electrons while LEED sees ion cores. This chapter will introduce the principle of each technique, experimental methods, the interpretation of the data, as well as the instruments.

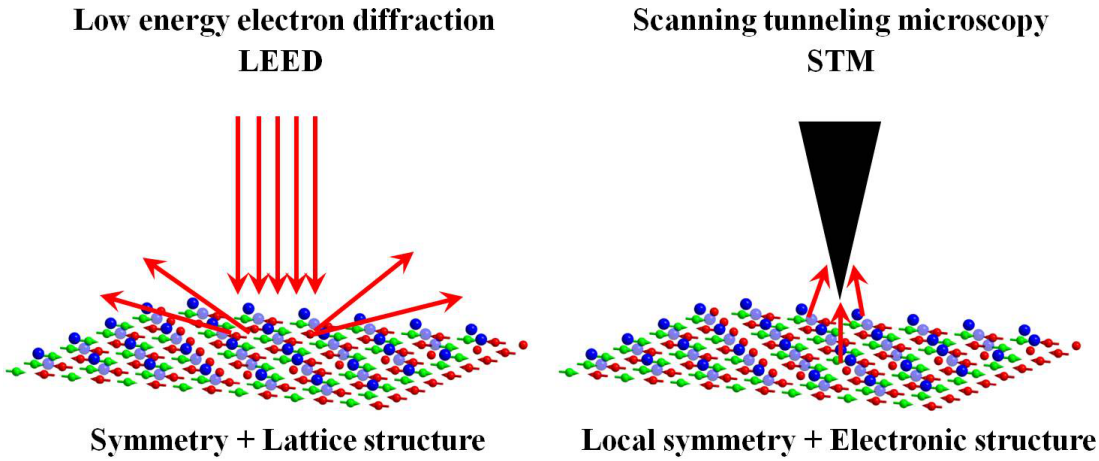

FIGURE 2.1. (a) STM sees electrons in real space (b) LEED sees ion cores in momentum space

2.1 Scanning Tunneling Microscopy/Spectroscopy

2.1.1 Principles

The scanning tunneling microscope (STM) was invented in 1981 by Binnig and Rohrer at IBM research laboratory [53], for which they shared 1986 Nobel Prize.

The instrument consists a tip scanning on a conducting sample to sense the structure of the surface. To some extent, the concept is similar to Braille-reading where the reader's fingers detect the impressed characters (Fig. 2.2a). For scanning probe microscope (SPM), a fine and sharp tip is used to detect the surface topography (Fig. 2.2b). Depends on which interaction between the tip and the sample is employed for imaging, the SPM can be specific to STM using the principle of quantum tunneling, or atomic force microscope (AFM) using all kinds of atomic forces such as mechanical contact force, van der Waals forces, magnetic forces in magnetic force microscope (MFM).

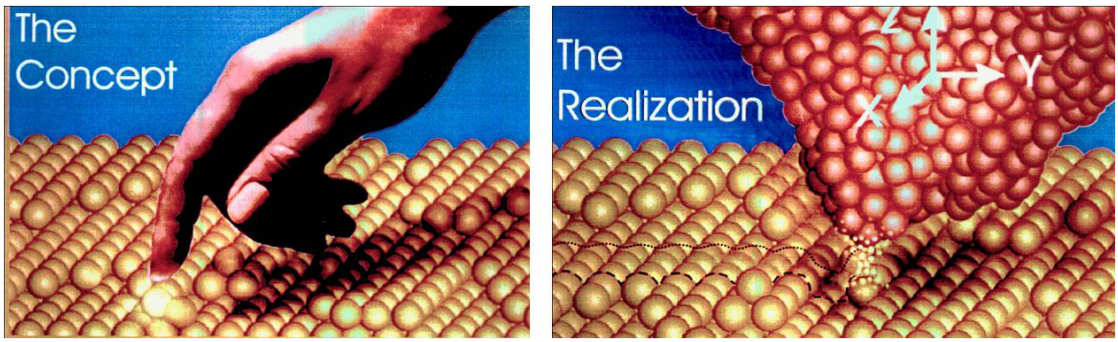

FIGURE 2.2. The concept (a) and realization (b) of STM imaging. Figure adapted from reference [54].

In STM, when applying a voltage between the tip and the sample, whose distance is down to nanometer or sub-nanometer scale, a tunneling current will flow. By keeping the current constant while scanning, a feedback loop will control the vertical movements of the tip. Recording the vertical height as a function of location (x, y) gives a two dimension topographic image. This is illustrated schematically in Fig. 2.3.

For simplicity, we use an elementary one-dimensional model to describe the quantum tunneling. A electron is trapped in a quantum rectangular potential well

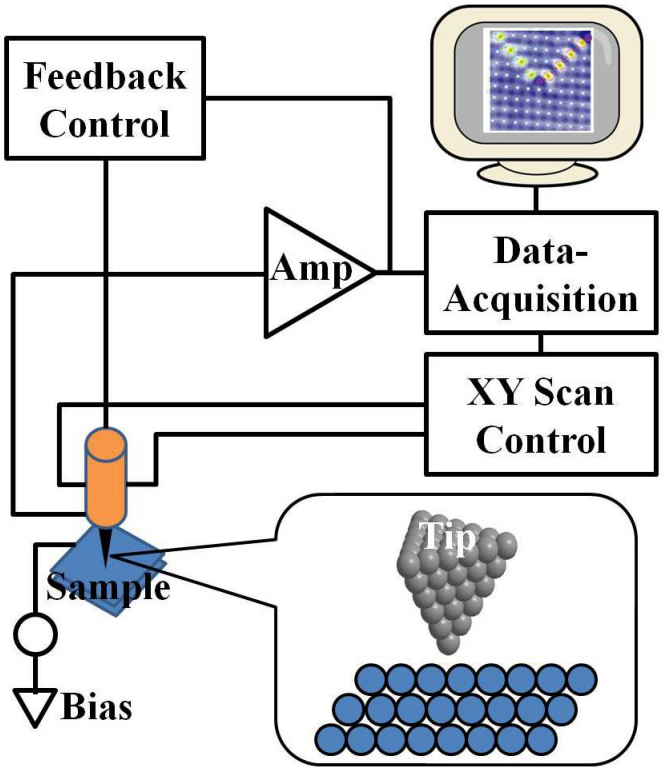

FIGURE 2.3. The schematic diagram of STM

with barrier *U(z)*(see Fig. 2.4). In quantum mechanics, the state of an electron is described by a wave function ψ and its behavior satisfies Schrdinger's equation:

$$-\frac{\hbar^2}{2m}\frac{d^2}{dz^2}\psi(z) + U(z)\psi(z) = E\psi(z) \tag{2.1}$$

In the classically forbidden region where *U(z)*>*E*, the Eq. 2.1 has a solution:

$$\psi(z) = \psi(0)e^{-kz} \tag{2.2}$$

where $k = \frac{\sqrt{2m(U-E)}}{\hbar} = \frac{\sqrt{2m\varphi}}{\hbar}$ is the decay constant and φ is the apparent barrier height (ABH).

It describes that the state of the electron decays in the *z+* direction. The probability density of observing an electron at z is proportional to $\|\psi(0)\|^2 \mathrm{e}^{-2kz}$, which is nonzero in the barrier region, indicating a nonzero probability to penetrate a barrier which is higher than its energy, i. e. a quantum tunneling process. The ABH is

defined as *U-E*, which is related to work function. Work function of a metal surface is defined as the minimum energy required to remove an electron from the bulk to the vacuum level. The ABH includes not only work function but also any modification to the tunneling barrier due to the crystallographic orientation, sample local topography, tip-sample angle, etc.

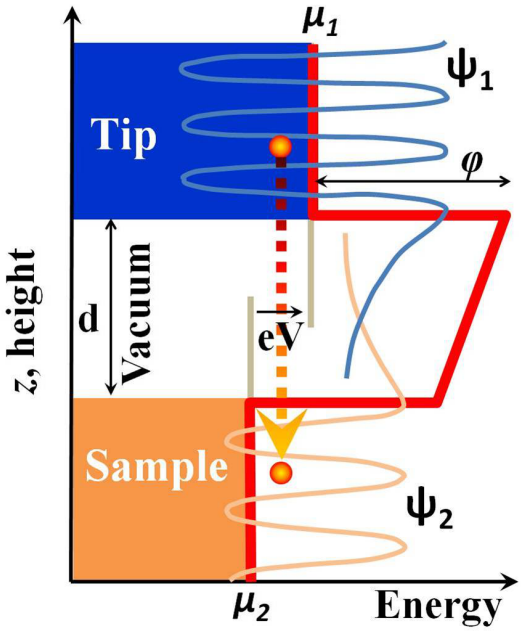

FIGURE 2.4. The schematic model of quantum tunneling of current

Obviously, if there is no bias voltage applied to the system, there will be no net tunneling current, simply because the quantum tunneling process is two way process, see Fig. 2.4. Applying a bias voltage allows an unbalanced tunneling process thus a net current occurs. By including all the states in the energy interval eV, the tunneling current is

$$I = I_0 e^{2kW} \propto \sum_{En=E_F-eV}^{E_F} |\psi_n(0)|^2 e^{-2kW} \tag{2.3}$$

with W as the vacuum gap between the tip and the sample. Here the tip was assumed to have constant density of states (DOS) near Fermi surface thus was

ignored for simplicity. This negative exponential relationship between the current and the tip-sample distance is the key for atomic resolution. For example, with a typical work function 4 eV, the decay constant k is about 1 $\mathring{A}^{-1}$. According to equation 2.3, the current decays about e^2=7.4 times per $\mathring{A}$. Thus, any topographic height difference will be amplified, i.e. a response of large current change, giving resolution in z direction up to pico-meter (10^{-15}m). This is the reason for the STM capability of atomic resolution.

If the tunneling junction bias V is small enough, the density of states can be conveniently written in terms of the local density of states (LDOS) at the Fermi level. At a location z and energy E, the LDOS or $\rho_S(z,E)$ of the sample is defined as

$$LDOS(z,E) = \rho_s(z,E) = \sum_{E_n=E_F-\epsilon}^{E} |\psi_n(z)|^2 = \sum_{E_n=E_F-\epsilon}^{E} |\psi_n(0)|^2 e^{-2kW} \tag{2.4}$$

for sufficient small E. The LDOS is the number of electrons per unit volume per unit energy, at a given point in space and a given energy. Obviously

$$I \propto \sum_{E_n=E_F-eV}^{E_F} LDOS(W,E) \tag{2.5}$$

Thus:

$$\frac{dI}{dV} \propto LDOS(W,E) \tag{2.6}$$

This relationship shows the capability of STM to investigate the electronic structure of the sample surface. Note that the LDOS is evaluated for the bare surface, i. e. in the absence of the tip.

For a more comprehensive analysis, with the weak coupling between the tip and the sample, first-order perturbation theory gives current:

$$I = -\frac{4\pi e}{\hbar}\int_{-\epsilon}^{\infty}\{|M_{st}|^2\rho_s(\epsilon)\rho_t(\epsilon+eV)f(\epsilon)[1-f(\epsilon+eV)]-f(\epsilon+eV)[1-f(\epsilon)]\}d\epsilon \tag{2.7}$$

Where *f(E)* is the Fermi Function, M_{st} is the tunneling matrix element between wave function of the tip and the sample, and E is the energy. To simplify this, the Fermi function is replaced by their zero-temperature values, i. e. the perfect cutoff Fermi surface. with a small bias, Eq. 2.7 becomes:

$$I \approx -\frac{4\pi e}{\hbar}\int_{-eV}^{0}\{|M_{st}|^2\rho_s(\epsilon)\rho_t(\epsilon+eV)\}d\epsilon \tag{2.8}$$

In reality, thermal smearing modifies this relationship. The tip density of states can be constant if we use a clean tungsten tip which has a flat density of states near Fermi surface.Thus, Eq. 2.8 becomes:

$$I \approx -\frac{4\pi e}{\hbar}\rho_t(0)\int_{-eV}^{0}\{|M_{st}|^2\rho_s(\epsilon)\}d\epsilon \tag{2.9}$$

Now it is easy to see that

$$\frac{dI}{dV} \approx -\frac{4\pi e}{\hbar}\rho_t(0)|M_{st}|^2\rho_s(\epsilon) \tag{2.10}$$

In Fig. 2.4, WKB (Wentzel, Kramers, Brillouin) approximation considers a square shape of tunneling thus:

$$|M_{st}|^2 = e^{-\frac{\sqrt{8m\varphi}}{\hbar}z} \tag{2.11}$$

which again provides the negative exponential relationship for the atomic resolution.

In summary,

$$I \approx -\frac{4\pi e}{\hbar}\rho_t(0)e^{-\frac{\sqrt{8m\varphi}}{\hbar}z}\int_{-eV}^{0}\{\rho_s(\epsilon)\}d\epsilon \tag{2.12}$$

$$\frac{dI}{dV} \approx -\frac{4\pi e}{\hbar}\rho_t(0)e^{-\frac{\sqrt{8m\varphi}}{\hbar}z}\rho_s(V) \approx \rho_s(V) or LDOS(V) \tag{2.13}$$

2.1.2 Types of measurement

Topography

The most common STM measurement is surface topography, i.e. the topographic height mapping of a surface. The principle is rooted in the current's negative exponential dependence of the distance between tip and sample surface from Eq. 2.12. There are two modes of imaging: one is constant-current mode by definition recording the tip-sample distance z as a function of location (x, y) while keeping the current as a constant; the other one is constant-height mode by with height fixed recording the current response then mathematically converting to corresponding height. Constant-current mode is much more common used in the scientific community.

The understanding of STM topography is a little tricky, because the current not only depends on z but also always involves the integration of LDOS at an energy window near Fermi surface. Further, there is no strict definition of distance between the tip and the sample and the cutoff diameter for an atom at the end of the tip. In reality, the end of the tip has a finite size (could be more than one end atom) and the proximity effect will smear out the real height contrast. Let's assume a scanning is in constant current I_0 mode with distance at z_0 and bias V_0. The STM scanner moving in-plane will response $\Delta z^{'}$ in z direction rather than the real topographic height Δz from the following equation:

$$\frac{dI(V)}{d(x,y)} = \frac{I_0}{e^{-\frac{\sqrt{8m\varphi}}{\hbar}z}0}\frac{d(e^{-\frac{\sqrt{8m\varphi}}{\hbar}\triangle z)}}{d(x,y)} + \frac{I_0}{\int_{-eV}^{0}\{\rho_s(\epsilon)\}d\epsilon}\frac{d(\int_{-eV}^{0}\{\rho_s(\epsilon)\}d\epsilon)}{d(x,y)} = \frac{I_0}{e^{-\frac{\sqrt{8m\varphi}}{\hbar}z}0}\frac{d(e^{-\frac{\sqrt{8m\varphi}}{\hbar}\triangle z')}}{d(x,y)} \tag{2.14}$$

Only when the first term dominates, then $\Delta z^{'} = \Delta z$. Thus, the assumption of interpreting the image as topography is that the LDOS at the surface is a constant at any bias at everywhere. i. e.

$$\rho_s(\epsilon, x, y) = constant \tag{2.15}$$

Then we will have $\Delta z^{'} = \Delta z$. In reality, the requirement is rarely meet except for simple metals which have a flat band structure. However, the problem with imaging the metal surface is that the second term can be huge with the itinerant electrons smoothing out the topographic height contrast because of either the finite size or finite tunneling channel. Further, the assumption can easily break down when there are defects and confinement induced electron density waves in space. A more realistic assumption is that:

$$\int_{-eV}^{\infty}\{\rho_s(\epsilon, x, y)\}d\epsilon = constant\ only\ depends\ on\ Bias \tag{2.16}$$

and with requirement that the second term is not a dominated contribution to the current. If the second term becomes larger, we can interpret the corresponding STM topography as the mapping to relative topographic height. This is a "relative" rather than "real" topographic height, because this constant still depends on the applied bias. Thus, by changing the bias, we will have different topography, but strictly speaking only the contrast is meaningful. In many cases, if the dominated current signal is from difference of z rather than the variation of the LDOS, the assumption of Eq. 2.16 is true.

Bias-dependent topography

As we discussed previously, the topography depends on the choice of voltage. Only at flat LDOS, the choice of voltage becomes less important, but again that is really rare except on metal surface (Still, the bias cannot be too high because the assumption of quantum tunneling may be broken down thus invalid Eq. 2.12.). There may be situation that the first term dominates, so the second term can be ignored, then the bias-dependence can be ignored.

The situation is very different when the change of current is dominated by the change of electronic structure. Then $\Delta z^{'}$ is very different from a real topographic Δz. In contrast, the topography is the map of the charge density integral of the energy window from eV below or above to Ferme surface. It is then determined by the band crossing Fermi surface, thus these mappings show strong dependence of bias. Sometimes, by changing the bias, the image contrast may even reverse.

The surface of lead coated Ge(111) is a good example to show the geometric and electronic contribution on the image at temperatures below and above a charge density wave order transition temperature. Figure 2.5 shows a 1/3 monolayer of equivalent adatoms with spaced $\sim 7\mathring{A}$ apart in a hexagonal array of T4 sites atop the bulk-truncated germanium lattice, forming the $(\sqrt{3}\times\sqrt{3})$R30° arrangement. This is a metallic surface at room temperature. Figure 2.6a shows room temperature STM topography at two different biases, the positive bias probing the filled states and the negative bias probing the empty states [20]. A hexagonal array of identical protrusions can be seen. These lattice bright protrusions are corresponding to Pb adatoms by theory [55], thus the topography is more geometric dominated with no bias-dependence, i. e. the first term in Eq. 2.15.

As the temperature drops below 250 K, the property of the surface dramatically changes to semiconductor and the geometric structure changed to new (3×3) sym-

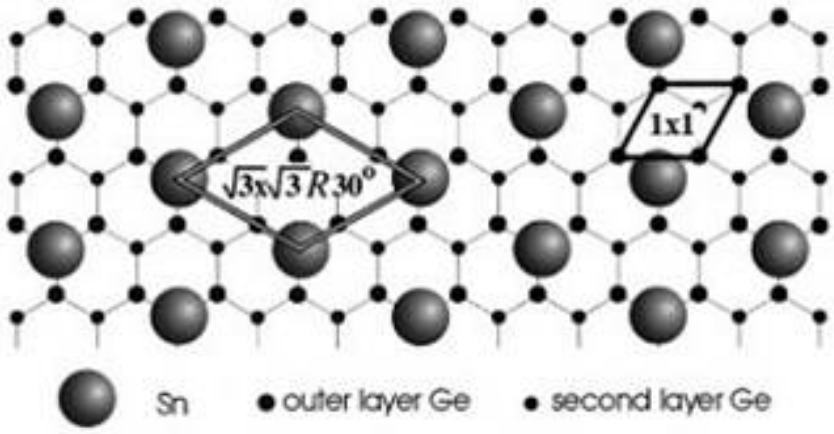

FIGURE 2.5. Top view of ball models of Pb or Sn coated Ge(111) surface

metry in LEED pattern. Low temperature STM topographies in Figure 2.6b show that the Pb adatoms are no longer equivalent. One out of three Pb atoms now poses an enhanced relative concentration of the filled states (bright protrusion at the center in right image of Fig. 2.6b) and diminished relative concentration of the empty states (dark protrusion at the center of the left image of Fig. 2.6b). Note that this is not a rippled topography but rather an electronic dominated surface because of the strong bias dependence of the STM topography - the filled states image reverse the contrast compared to the empty states image.

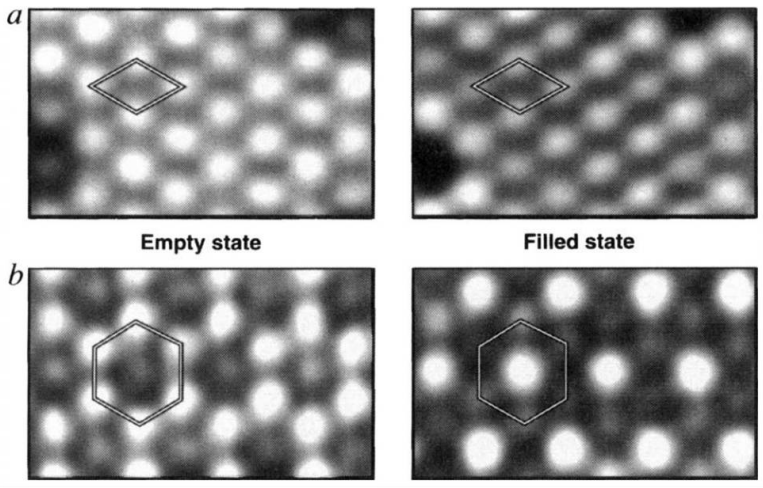

FIGURE 2.6. Bias dependent STM topography of Pb coated Ge(111) Surface

Such bias-dependence indicates that this new (3×3) order is a commensurate surface charge density waves (CDW) occuring at low temperature, which is not a bulk phenomenon. A CDW is a periodic symmetry lowering redistribution of charge within a material, accompanied by a rearrangement of electronic bands and usually a small periodic lattice distortion. Compared with examples of bulk CDW, this surface incorporates a structural distortion seen by LEED pattern. This is a direct observation of the surface CDW which is temperature-induced and reversible.

$\frac{dI}{dV}$ curve measurement

We typically refer dI/dV curve as scanning tunneling spectroscopy (STS), where recording the dI/dV signal as changing the bias. Since dI/dV or differential conductance is proportional to LDOS, the STS will be the $LDOS(eV)$ curve, the band crossing the Fermi surface. Technically, dI/dV as a function of applied voltage can be obtained by the first derivative of I/V curve. The direct and more precise way is to use a look-in technique. A small *sine* voltage modulation is added to the bias, and then the responses on the current are recorded and analyzed in a look-in amplifier. The output will be the dI/dV signal without the phase shift of the current response and modulation voltage.

Eq. 2.13 is valid under WKB approximation of Eq. 2.10. However, it is possible that the applied bias voltage will affect the surface wave functions through the tunneling matrix M_{st} which leads to complication of the tunneling spectrum dI/dV. The M_{st} is strongly bias V dependent when the voltage becomes an appreciable fraction of the work function. Thus, the V-dependence of dI/dV may distort the features in the STS.

Stroscio et al proposed a simple but effective solution to this problem [56]. They normalized dI/dV by dividing it by I/V, which yielded $d(lnI)/d(lnV)$, effectively

cancelling out the exponential dependence of M_{st} on V. However, this normalization is both unnecessary and undesirable at small bias in which case, I/V is well behaved and *(dI/dV)/(I/V)* is identically equal to unity for ohmic systems and carriers no information.

In the study of HTSC cuprates [57], a common way is to use dI/dV below Tc dividing by dI/dV normal state at above T_c, i. e. $(dI/dV)_{SC}/(dI/dV)_N$ when the tunneling conductance at high temperatures is weakly dependent on temperature and energy. This ratio, which is independent of the tunneling matrix element, can be used to extract the temperature dependence of the energy gap and features associated with strong coupling of electrons to bosonic modes in cuprates.

$\frac{dI}{dz}$ curve measurement

From the negative exponential relationship of the current and tip-sample distance in Eq. 2.3, we can have apparent barrier height (ABH):

$$\varphi \approx \frac{\hbar^2}{8m}(\frac{d\ln I}{dz})^2 \approx 0.95(\frac{d\ln I}{dz})^2 = -3.8k^2 \tag{2.17}$$

Experimentally, this ABH can be measured by changing the tip-sample distance. Again, the ABH is approximately equal to the average work function of the tip and the sample, as well as affected by the applied bias and also geometric configuration of the tunneling junction.

$$\varphi = \frac{(\varphi_s + \varphi_t - e|V|)}{2} \tag{2.18}$$

With the known work function of the tip, we can get the work function of the sample surface.

Topo-mapping

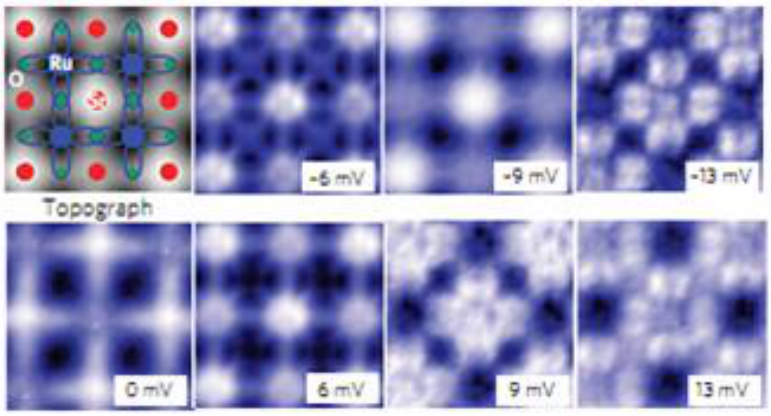

FIGURE 2.7. STM topo-mapping of dI/dV at the surface of $Sr_3Ru_2O_7$. The top left-hand panel shows the locations of Ru atoms and their d_{xz} and d_{yz} orbitals in blue. Red and green circles mark the positions of Sr, and O atoms, respectively. Each subsequent panel shows topo-maps of dI/dV resolving sub-unit-cell spatial features in the same field of view. Whereas some mappings show high intensity mainly at the positions of the Sr atoms (-9, 0 meV), others clearly resolve sub-unit-cell features with the symmetry and location of the d_{xz}, d_{yz} orbitals (-13, +9, +13meV). Figure is adapted from reference [59].

Even though topography can show electronic information as in the CDW in Figure 2.6, there is a more directly way by mapping the LDOS rather than the topographic height z. In principle, any parameters can be measured at each point as a function of location (x, y) thus creating a 2D mapping of this parameter. This is called topo-mapping and besides height z the most frequent measured parameter is LDOS at given bias V. From Eq. 2.13, this is to measured dI/dV at given bias crossing all over the surface location. dI/dV is proportional to density of states but it call also been called differential conductance. The map of local density of states at certain energy is purely electronic information.

Figure 2.7 shows sub-unit cell orbital structure in $Sr_3Ru_2O_7$ from several differential conductance mapping at very low energy of several meV and low temperature of 3.8 K. The top left topography shows the locations of Ru, O and Sr sites, and no clear features is inside the unit cell. The rest LDOS mappings reveal pattern

related to d_{yz} and d_{xz} orbitals. It is argued that there images are actually mapping the energy evolution of strongly renormalized Wannier states [59].

STS-mapping

There is another type of mapping. Recording STS curve at every pixel of the surface, then the data is a three dimension *LDOS(x,y,V)*. A plane cut parallel to *x-y* plane will generate a series of differential conductance mapping. The *LDOS(x,y,V)* data is used to detect the energy evolution of the interference wave vectors (momentum), thus providing a band dispersion for the surface. This method has been used quite often and successfully in cuprate studies. Similar types of mapping include Gap mapping where each pixel will have a value of gap size, ratio of conductance mapping and each pixel will have a valve of the ratio of *dI/dV(+V)* divide by *dI/dV(-V)*, etc [58, 29].

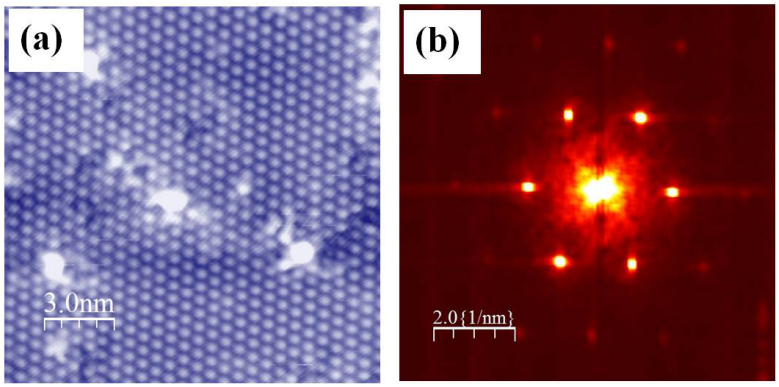

FIGURE 2.8. (a) STM topography of surface of Ag($\sqrt{3}\times\sqrt{3}$)-Si(111) with its FT-image in (b).

Fourier-Transform (FT) STM images

A useful technique to analyze the STM images from several types measurements above is to study the Fourier-Transform (FT) STM images. FT-method will transfer the periodicity of the lattice in real space STM images to a spots pattern in momentum space. For instance, Fig. 2.8a shows a real-space STM topography on Ag($\sqrt{3}\times\sqrt{3}$)-Si(111) surface with hexagonal arrangement of Ag atoms. The FT-

image reproduces the periodicity in momentum space and the spots pattern is similar to a LEED pattern. For a topography with poor resolution in real space, sometimes it is easier to use FT-image to identify the periodicity from the momentum space. Further, FFT-image can be especially useful, if there is a long-range wave-like modulation on the STM images. The topography on Be(0001) in Fig. 2.9a is dominated by enhanced surface Friedel oscillation, and its FT-image shows that, besides the spots associated to Be reciprocal lattice, there is a ring with twice the radius of the surface state of the 2D Fermi surface ($2k_F$ *vs.* k_F). Note that even though the Be lattice cannot be "seen" in the STM image, it is nonetheless identified in the FT-STM image. Thus, the FT-STM image represents a combined structural and electronic measurement, containing the information obtained from both LEED and angle-resolved photoemission spectroscopy (ARPES). A FT-STM image directly produces a "picture" of the 2D Fermi surface. In more complex system where Fermi surface is anisotropic, the FT procedure is typically done on a topo-mapping whose FT image can directly show wave-vectors for the quasi-particle interference or Fermi surface nesting, which have been demonstrated in high Tc cuprates [60], heavy Fermions [61], topological insulator [62], ruthenates [59], and Fe-based superconductors [63, 64].

2.1.3 STM instrument and experimental procedures

Instrument

The instrument at LSU is a home-built variable and low temperature STM. It was built at University of Tennessee at Knoxville by M. H. Pan. There are two special designs of this STM worthy to mention. One would be the design of the coarse approach - Pan (S. H. Pan) type design [66], the other would be the cryogenics mechanical design by W. Ho [67]. Figure 2.10a shows the Pan-type head and the Fig. 2.10b shows the thermal cooling design. References [66] and

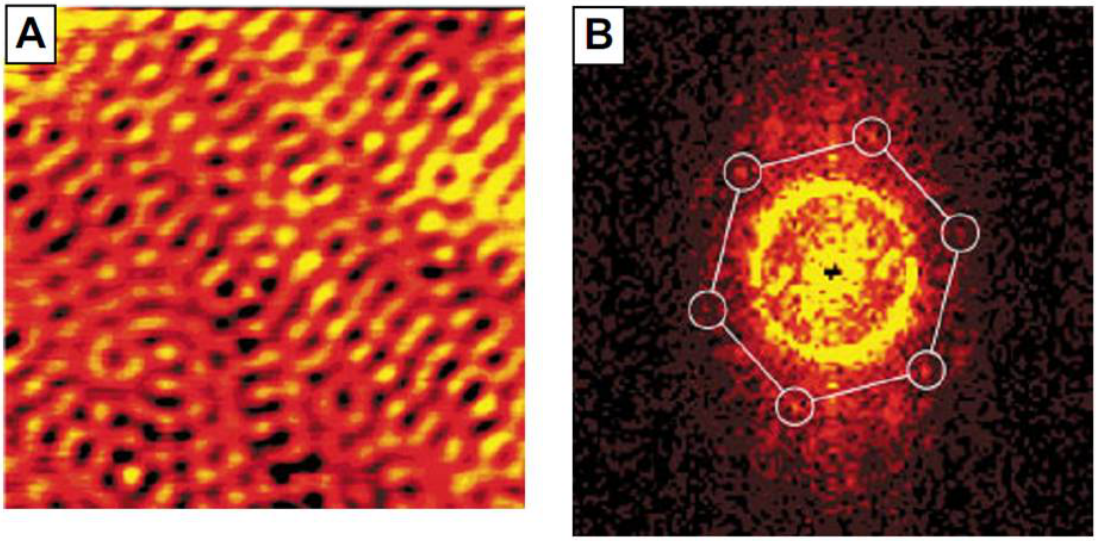

FIGURE 2.9. (a) Constant-current STM image (40 $\AA$ by 40 $\AA$, I=1.5 nA, V=4 mV) of Be(0001) at 150 K. (B) The 2D FT of the image in (b). Figures are adapted from reference [65].

[67] provide the technical details. In short, the Pan-type has a favored mechanic stability for atomic imaging and spectroscopy and the Ho's design of the cooling not only allow temperature to vary from lowest 10 K using liquid helium to room temperature with a heater inside but also keeps the system mechanically stable.

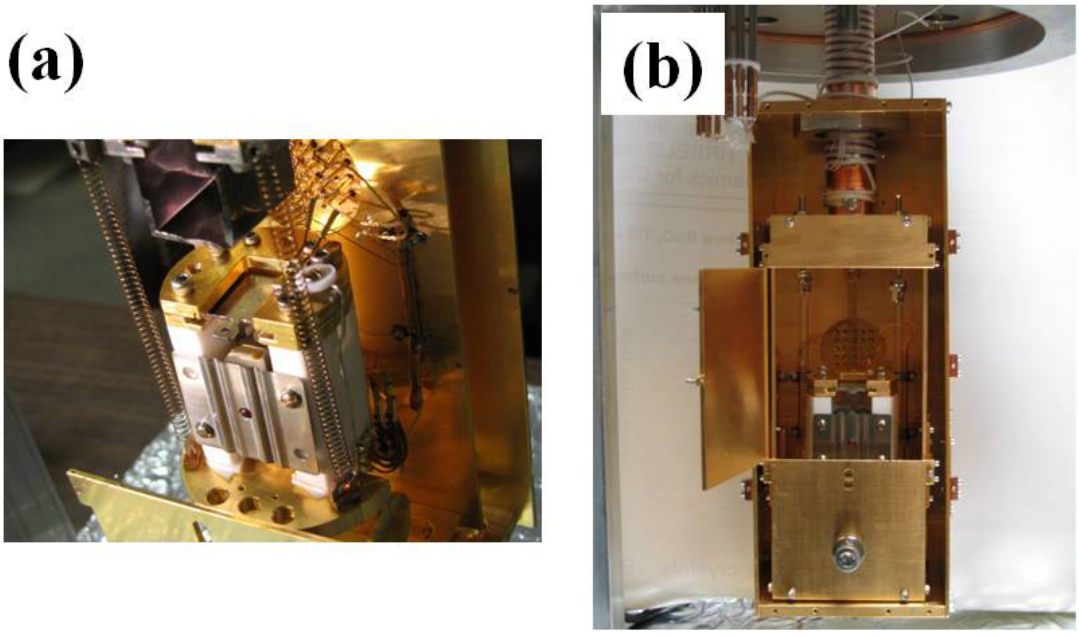

FIGURE 2.10. Instrument: (a) STM Head (b) Variable temperature design.

Experiments procedures

Liquid nitrogen and liquid helium are to cool the system. For this study, the lowest instrument temperature has been tested to reach to 15 K using liquid helium and 80 K using liquid nitrogen. The temperature fluctuation can be reduced to *0.05K/hour*. Samples are cooled down with the thermal shielding box, and typically cleaved at the low temperature at the cleave-box shown in Fig. 2.10a. Then they are transferred to sample stage with a wobble stick. The locked STM head will be released, and coarse approach can start after the temperature becomes stable.

Typical parameters used for topographic imaging depend on the samples studied. The typical absolute value of bias range is from 20 mV to 1.5 V at liquid nitrogen temperature, and can be lower as 5meV at liquid helium temperature. The current ranges from 30 pA to 2 nA. The $r.m.s$ of voltage modulation should be no less than $k_B T$ (where room temperature $k_B T$=25.6 meV). The frequency should be tested and optimized to show the most clear (low noise) output dI/dV signals. The Rule of Thumb is never use the frequency which is the integer or half-integer number times of the electrical base frequency 60 Hz, or the base mechanical noise frequency of the STM head or the summary of both.

To achieve the atomic resolution, the critical and complex variables are the noise level and the condition of tip. Atomic corrugation can be as small as several picometers thus easily burred in the noise. Common practice to reduce the noise level are using airlegs, tuning the head positions, aligning the cables, etc.

The ideal tip end should have one or two atoms, but it is never a guarantee with traditional tip treatments. Pt/Ir tips and tungsten tips are both used in this study. Pt/Ir tips are either handed cut or etched. Tungsten tips are etched. After that, tips are clean by alcohol and deionized water. All of the tips are tested in an air STM to achieve atomic resolution on HOPG and the best one will be installed

to STM head. The air STM is an commercial EasyNano STM. When tip is in vacuum, a field-emission may be conducted to clean the tip further and it will be tested with scanning on clean Au or Cu surface until a reasonable resolution and STS curve got with a stable junction.

A special note on STM.

STM is such powerful tool that is widely used in scientific studies. Reference [68] reviewed a 10 mK STM with a magnetic field as high as 14 T. However, it is important to point out that a normal STM is sensitive to charge but not spin, or chemical signals. The tunneling current does not know the spin information until the tip is magnetic, i. e. spin-polarized STM can detect spin information. Here, the spin degree of freedom is detected indirectly either by comparing theory to experiments, or either by its coupling to the charge and lattice. This thesis provides two examples of how we could indirectly probe the spin information with a combination of non-spin sensitive surface techniques and theory.

The tunneling current is never sensitive to chemical identity. It cannot tell whether the protrusion or depression corresponds to what atomic site. Because STM is also only sensitive to the charge, STM is not a structural tool to determine the structure. To under the detail surface structure, low energy electron diffraction has been proven to be the most reliable tool.

2.2 Low Energy Electron Diffraction

As discussed previously, STM is not a structural tool and it sees only the charge density. In contrast, LEED serves as an important complementary tool to STM because it produces diffraction pattern reflecting reciprocal lattice information and when properly used it determines the surface structure.

2.2.1 Principles

Two-dimensional Periodicity and the LEED pattern

Electrons can be either waves or particles. When they are elastically scattered from a periodic lattice they have a de Broglie wavelength of

$$\lambda = \frac{\hbar}{\sqrt{2mE}} \tag{2.19}$$

where m is the mass of the electron and E is its energy. For an electron beam with energy 100 eV, the wavelength is about 1.2 $\mathring{A}$ which is in the order of atomic scale. When this electron beam interacts with a periodic lattice, the diffraction/interference becomes significant and observable in the length scale of experimental apparatus LEED.

Fig. 2.11 shows the schematic view of LEED apparatus. An electron beam of known energy E incidents in normal direction at a surface of a single face crystal. The incident electrons are scattered strongly by the crystal lattice at the surface layers and only a small portion of the incident electron flux is back scattered elastically in discrete directions (see Fig. 2.11) , forming a LEED pattern.

From the momentum and energy conservation of the elastic scattering, for every diffraction spots, we have following relations between incident electrons (o) and diffracted electrons (out):

$$E_{out} = E_o \tag{2.20}$$

$$Q = k_{out}^{\parallel} - k_o^{\parallel} = G_{l_1 l_2} = l_1 b_1 + l_2 b_2 \tag{2.21}$$

where G is a reciprocal lattice vector labelled by Miller indices l_1 & l_2 with b_1 & b_2 as the respective axis vectors of the reciprocal lattice. The back-scattered electrons

are accelerated to form discrete bright spots on a fluorescent screen, forming a map of the two-dimensional reciprocal lattice of the crystal layers, i. e. LEED pattern. The spot pattern so obtained gives the sizes, shapes, and orientations of the two-dimensional reciprocal lattice. The ideas are familiar to materials scientists and X-ray crystallographers concerning that three-dimensional symmetry operation can be easily adapted to the two-dimensional cases of an ordered surface by using electrons scattering process rather than X-ray. The LEED pattern gives no direct information, however, of the crystal structure in the direction normal to the surface plane.

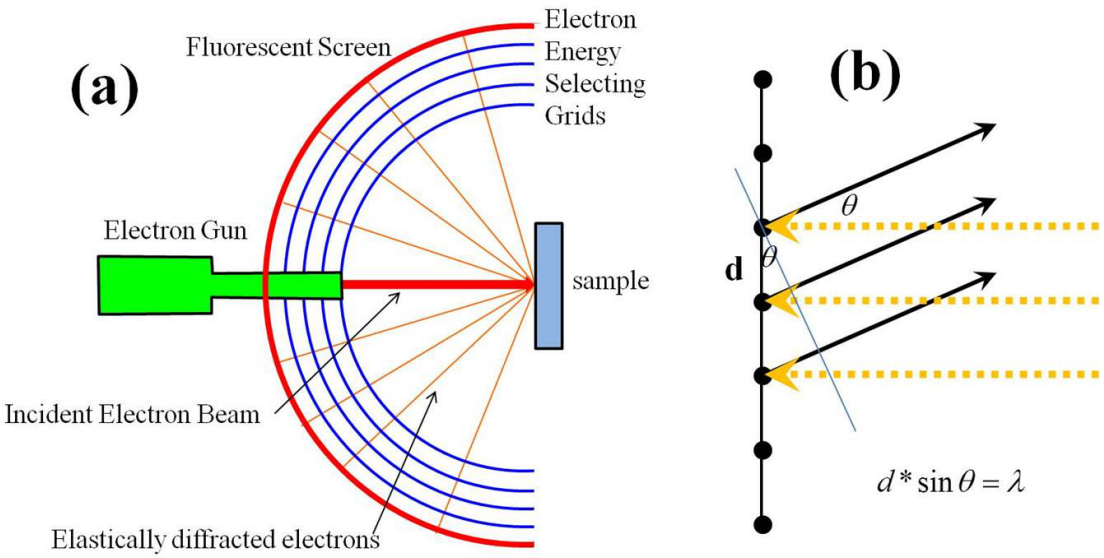

FIGURE 2.11. (a) The schematic view of LEED apparatus. (b) The Bragg condition for diffraction.

Surface Sensitivity

In LEED experiments, only those electrons that are back-scattered elastically are measured by filtering out the inelastic electrons which have lost appreciable energy ($>1\ eV$) using multiple retarding grids. Figure 2.12 shows the energy distribution of scattered electrons in a solid. Most of the electrons are inelastic and only 1 or 2% of the incident electrons are elastically back scattered in Fig. 2.12 where the sharp

peak at the right contains the elastically back-scattered electrons. The consequence of strong inelastic excitations in the target materials is that the mean free path of the incident electrons is only a few atomic layers. Thus, the elastic component of the back-scattered electrons only probe information about the surface region, leading to the surface sensitivity of the LEED intensity (I) versus voltage (V) curves thus is making LEED one of the most powerful tools for the study of surface structure.

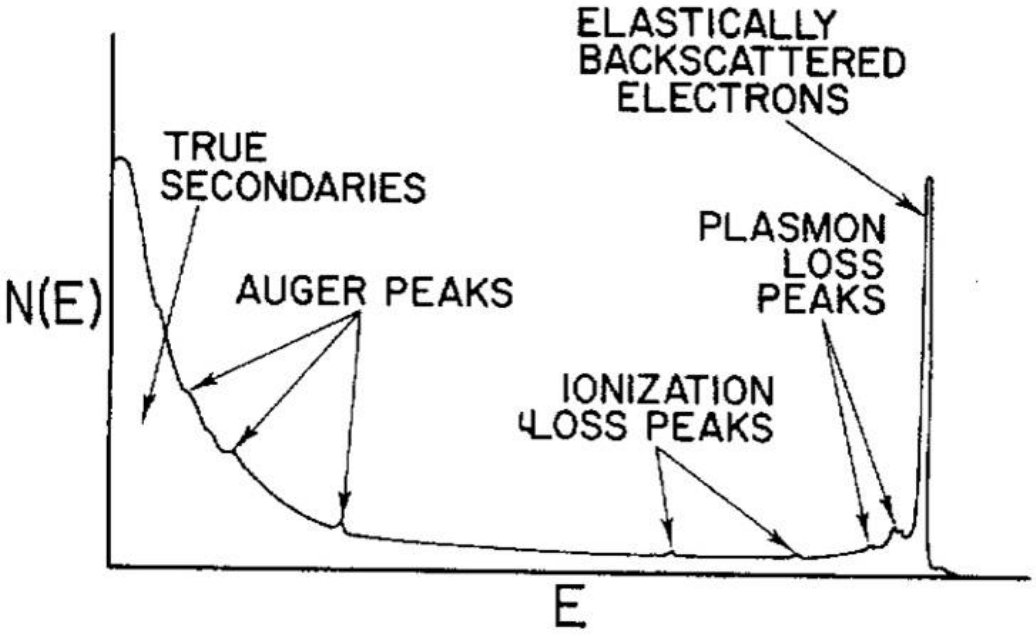

FIGURE 2.12. Schematic diagram of energy distribution of scattered electrons in a solid. The sharp peak at the right contains the elastically back-scattered electrons. (Figure adapted from reference [69].

2.2.2 Pattern analysis

This section and next section will introduce the application of LEED including LEED pattern analysis and I-V analysis. Two examples related to this thesis are given below.

Coexistence of multiple surface phases of 1×1, 1×2 and ($\sqrt{2}\times\sqrt{2}$)R45°.

(1×1) is defined as the unit cell from the top view of bulk truncated surface. For example, Fig. 2.13a is the top view of the bulk truncated surface with the short & thick lines representing the axis vectors for a (1×1) unit cell. With the known real space 2-D lattice with its superlattice, LEED pattern can be simulated. Here used is the software LEEDpat32. The reciprocal lattice for Fig. 2.13 would be like a square (1×1) lattice. The simulated LEED pattern in 2.13b is actually identical to the reciprocal lattice with the middle spot always have the biggest shape and highest intensity. The unit cell vectors were shown in both figures. The spots with circles on LEED pattern thus all correspond to (1×1) lattice. .

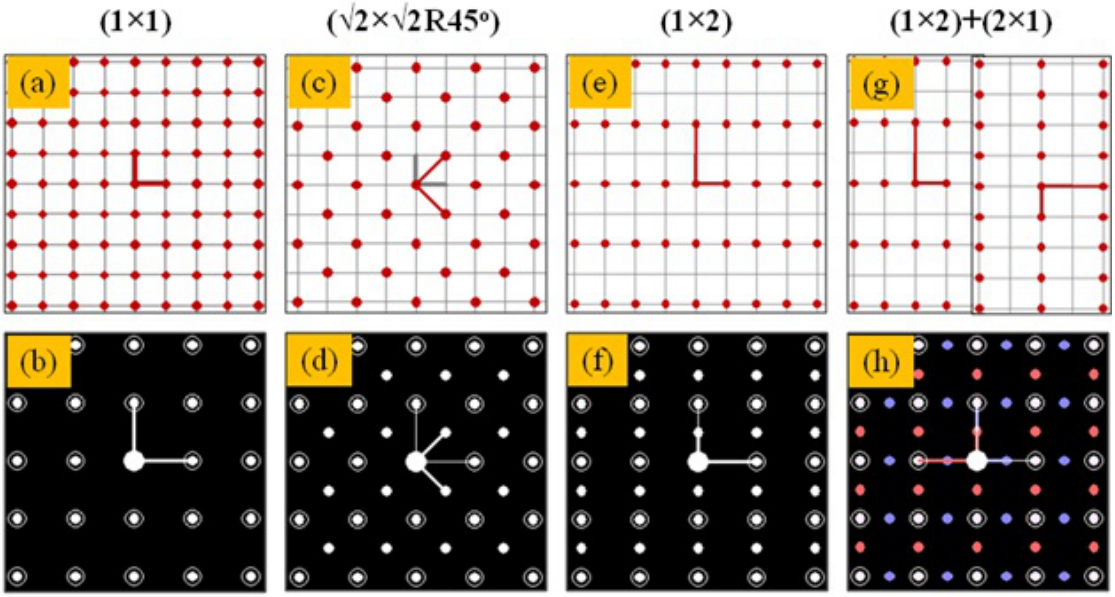

FIGURE 2.13. The corresponding LEED pattern of bulk truncated (1×1) square lattice phase and several surface reconstruction phases including $(\sqrt{2}\times\sqrt{2})$R45°, 1×2, and its twin domains.

When there is a surface reconstruction or super-lattice, for example in Fig. 2.13c, every alternative atom is the same along both directions and nearest identical atom is now *sqrt*2 times lattice constant distance away. It can be seen as two sub-lattice overlap (one is at buckling-up position and the other is at buckling-down position) with a one square unit vector shift in plane. Either sub-lattice has $(\sqrt{2}\times\sqrt{2})$R45°

super unit cell with one atom in the super unit cell but the overlapped lattice has also an $(\sqrt{2}\times\sqrt{2})$R45° super unit cell with one atom up and one atom down. Thus, the superlattice is a $(\sqrt{2}\times\sqrt{2})$R45° order or so the called c(2×2) phase. The simulate LEED pattern (Fig. 2.13d) shows that besides the circled (1×1) spots, there are additional fractional spots (not circled) in the center of the circled (1×1) spots reciprocal unit cell (thin white lines). In other ways, there is a small unit cell vector (thick white lines) about $1/sqrt2$ of the (1×1) spots unit cell vector.

Figure 2.13e shows a (1×2) superlattice where lines of atoms are alternative missing. The 4-fold symmetry is now 2-fold. Its simulated LEED pattern in Figure 2.13f shows this symmetry. Additional fractional spots (no circles) appear in this LEED pattern. If surface has twin (perpendicular) domains in Figure 2.13g, the LEED pattern shows additional fractional spots with red color at from (1×2) domain and blue color from (2×1) domain. The integer (1×1) spots, however, now are mix signals from both domains.

While in LEED experiments, we observe a LEED pattern then propose a possible structure model. If there are additional fractional spots, the surface is reconstructed and the superlattice unit cell can be constructed by analyzing the fractional spots positions. This problem becomes difficult when there are multi-domains on the surface. For example, if Figure 2.13b is the LEED pattern observed in experiments, without knowing the distances between fractional spots, the LEED pattern is the same with a (1×1) phase. The position of the spots will be used to determine, for example, whether the spots with different color all correspond to (1×1) spots or just the circled ones. Back to Fig. 2.11b with the Bragg's law of diffraction, along θ direction, we can have integer spots where

$$d \cdot \sin\theta = n\lambda \tag{2.22}$$

Where d is the lattice constant, and n is the integer spots index. From the geometric configuration of LEED apparatus, we have

$$\sin\theta = \frac{d(integer\ spot)}{d(LEED\ screen\ to\ sample)} \tag{2.23}$$

then the lattice constant is

$$d = \frac{d(LEED\ screen\ to\ sample)}{d(integer\ spot)} \cdot n\lambda \tag{2.24}$$

From the lattice constant we know the real index for the spots on LEED pattern, thus obtaining the surface unit cell.

If the LEED pattern comes from the multiple phases, the LEED pattern alone we cannot distinguish whether the phase has (1×1) phase and the intensity of integer spots are mixed signals. In this thesis, we have seen such phase coexisting at the surface of Ba122, which will be explained in chapter 5.

Glide plane symmetry in Ruthernate surface.

It is worthwhile to show an example of LEED pattern on ruthenates whose key structure is the RuO_6 octahedra which can have structural distortion of rotation and tilt. The bulk structure of Sr_2RuO_4 has no tilt and no rotation. Figure 2.14a shows the bulk-truncated structure of Sr_2RuO_4 with no rotation and tilt structural distortion. Thus, the expected LEED pattern in Fig. 2.14b shows no additional fractional spots. However, the actually surface of Sr_2RuO_4 shows reconstruction with 9° of rotation at low temperature and 6° at high temperature, shown in Fig. 2.14c. It creates a surface unit cell which is $(\sqrt{2}\times\sqrt{2})$R45°. Fractional spots will appear at the center of each 4 nearest integer spots in Fig. 2.14d but there are fractional spots missing at all energies along the perpendicular dashed white lines, i. e. glide lines.

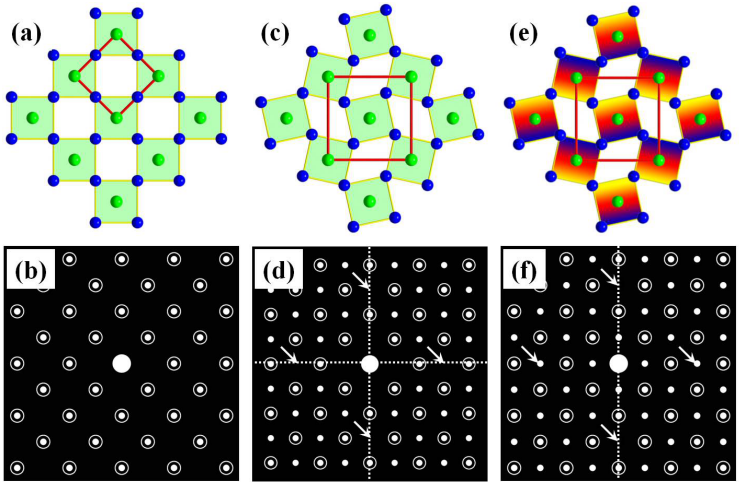

FIGURE 2.14. Top view of ruthenate compounds with (a) no rotation and no tilt (c) with only rotation (e) with both rotation and tilt structural distortion. Below (b), (d), (f) are corresponding simulated LEED pattern. Comparing to (b), rotation induced fractional spots with two glide lines in (d). Comparing to (d), tilt makes one glide line disappear, i. e. re-appearance of the fractional spots.

Glide reflection is a result by reflecting a figure about a line and translating it in a direction parallel to the line. The fractional spots will be extinct along glide lines because of the π-phase mismatch in the structure factor (explained later). Rotation in Figure 2.14c has glide reflection symmetry along orthorhombic orthogonal direction. Thus the fractional spots are extinct along dash white lines in Fig. 2.14d. The additional tilt distortion in Fig. 2.14e breaks the glide symmetry along the horizontal line thus the missing fractional spots appear in Fig. 2.14f. More detail analysis on similar LEED pattern will be in Chapter 6.

LEED spot profile analysis.

The diffraction spots would be infinitely sharp if the experiments were performed on a perfect, rigid, and infinite crystal with a perfect instrument. In practice, the diffraction spots are finite size due to the instrumental distortion and surface imperfections. Figure 2.15b shows a line profile crossing a spot shown in LEED pattern of $Sr_3(Ru_{0.84}Mn_{0.16})_2O_7$ in Fig. 2.15a. The full width at half maximum (FWHM) of the peak, due to the instrumental distortion, consists of several major

contributions: the coherence of the incident beam (i.e. the energy spread plus the beam divergence), the electron beam diameter, the focus on the diffracted beam, the normal incidence and some others. To achieve the best LEED pattern quality, besides preparing the best quality sample surface, extra care needs to be taken on the focus of the beam and the normal incidence. The coherence of the incident beam and beam diameter is determined by the electron gun thus not tunable. The coherence length, the diameter of coherently scattered area, is only 10 to 20 nanometer for a standard LEED optics.

The line profile of the spot also reflects the surface imperfection, thus in principle it can be used to analyze the crystalline structure. Standard LEED optics lacks sufficient resolution due to the instrumental distortion. Spot-profile-analysis (SPA) LEED can provide a precise quantitative analysis of lateral and vertical lattice constants, terrace/islands size and height distribution, ordering parameters in phase transitions and much more. In this thesis, however, we mainly focus on the standard LEED pattern and I-V analysis.

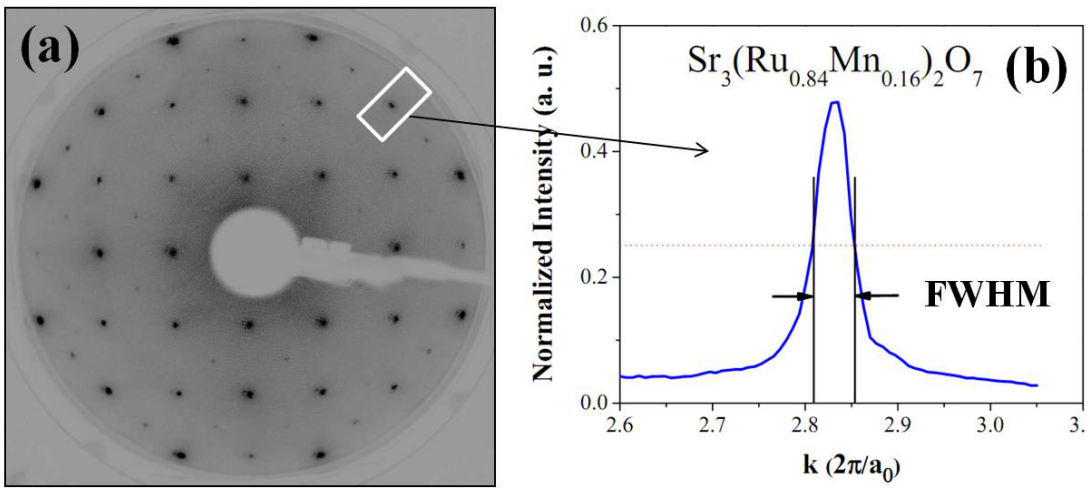

FIGURE 2.15. LEED pattern of $Sr_3(Ru_{0.84}Mn_{0.16})_2O_7$ at 87 K with 225 eV. (b) Line profile crossing the spot shown in white rectangular in (a)

2.2.3 Intensity versus Voltage analysis

The LEED pattern contains information about the two dimensional reciprocal lattice but no information about the positions of the atoms in the unit cell relative to the bulk. In order to gain information about the surface structure, it is necessary to measure the intensities of spots as the function of beam energy. A curve so obtained is called intensity (I) -voltage (V) curve and the interpretation of intensity data requires an understanding of LEED theory and I-V analysis methods.

This section will describe the specific methods developed for the determination of the surface structure through the interpretation of intensity data. The kinematic methods are relatively simple and therefore provide a computationally efficient approach. However, surfaces do not diffract low-energy electrons kinematically and the approximations involved lead to a loss of accuracy and reliability. Thus, dynamical-scattering formalism and attempt to reproduce the experimental data theoretically by a trial-and-error search for the correct structure is needed for a detailed and reliable structural determination.

Kinematic Theory: single scattering

In cases when an electron has been only scattered once by a surface atom, a simple kinematic theory can applied to interpret the diffraction intensity. A alternative definition is the situation in which each wave packet representing one electron incident on a surface is diffracted elastically only once by the surface [70]. This is demonstrated in Fig. 2.16a. The kinematic method has been quite successful in the interpretation of the diffraction in X-rays and neutron scattering and in a few systems by LEED.

In LEED experiments, the incident monoenergetic electron beam can be represented by a plane wave which is described by:

$$A_i = A_0 e^{-i\vec{k_o}\vec{r}} \tag{2.25}$$

Where A_i is the amplitude of the incident wave, A_0 is a constant, k_0 is the incident wave vector and r is a space vector. In single scattering approximation, the amplitude of a diffracted beam is represented by:

$$A_s = A_0[\sum_n \alpha f_n(\vec{s}) e^{-i\vec{s}\vec{r_n}}] e^{-i\vec{k_{out}}\vec{r}} = e^{-i\vec{k_{out}}\vec{r}} \tag{2.26}$$

where $f_n(\vec{s})$ is the atomic scattering factor for the nth atom located at position $\vec{r}_n$. $\vec{s}$ = $\vec{k}_{out}$ - $\vec{k}_o$ is the momentum transfer, and $\vec{k}_{out}$ is the wave vector of the scattered wave. $\alpha$is a constant to be determined later. For elastic scattering, we have:

$$E = \frac{\hbar^2}{2m}|\vec{k_o}|^2 = \frac{\hbar^2}{2m}|\vec{k_{out}}|^2 \tag{2.27}$$

Electrons projecting from vacuum into a surface are actually accelerated to a higher kinetic energy by surface dipole layers. Thus the kinetic energy inside the surface is E + V_o where V_o (> 0) is the so called "inner potential" which will be discussed in multiple scattering later.

The intensity of the diffraction spots would be proportional to the plane wave area density times the area. That gives incident beam intensity as $Ck_o\|A_o\|_2$ and diffracted beam intensity:

$$C(\cos\theta_{out}/\cos\theta_o)k_o|B|^2 \tag{2.28}$$

C is the cross section area of incident beam and incident angle θ_o in the normal incident case and θ_{out} is the angle of diffracted beam in Eq. 2.22.

Now let's focus on the structural factor S in the kinematic theory.

$$S = \sum_n f_n(\vec{s}) e^{-i\vec{s}\vec{r}_n} \tag{2.29}$$

In a two dimensional case for a surface with ordered lattice, with

$$\vec{r}_n = \vec{R}_p + m_1\vec{a}_1 + m_2\vec{a}_2 \tag{2.30}$$

Thus, the structure factor is given by

$$S^{2D} = [\sum_p f_p(\vec{R}_p) e^{-i\vec{s}\vec{R}_p}]\{e^i\vec{s}(m_1\vec{a}_1 + m_2\vec{a}_2)\} \tag{2.31}$$

The sum over lattice vector is proportional to the Dirac delta function, thus Eq. 2.21 is the solution to Eq. 2.31 for any integer of l_1 and l_2.

When consider a 2-dimension Bravais lattices of atoms, the Bragg energies E^B follows: (The kinematic energies with maximum intensity for any given diffraction beam satisfy Eq. 2.21.)

$$2(E^B + V_o)\cos^2\theta = n^2\frac{\pi^2}{d^2} \tag{2.32}$$

Where d is the interlayer spacing. If taking to normal incidence with a rectangular lattice, it can be written as

$$2(E^B + V_o) = \{\frac{\pi}{d}(n - l_1b_1 + l_2b_2) + \frac{\pi}{n - l_1b_1 + l_2b_2}[(\frac{b_1}{a_1})^2 + (\frac{b_2}{a_2})^2]\} \tag{2.33}$$

Thus in kinematic limit, it can be used to identify the intensity peaks at I-V curves. Figure 2.17a give a demonstration of I-V curves determined by Eq. 2.33. In Xenon and aluminum surfaces, one finds strong peaks close to the Bragg energies. However, in many cases, there is no obvious connection exist between Bragg energies and strong peaks, which is due to the multiple scattering.

Dynamical LEED theory: Multiple Scattering

The kinematic limit in weak-scattering is characterized by a total transmission 1 while an improved physical description should have less than 1. Electron diffraction is actually termed a dynamical process because it is a multiple scattering process in most of the cases. Two main features are commonly implied in dynamic process. First, multiple scattering of the diffracted electron occurs within the individual atom and the scattering is described by several parameters such as phase shifts, which are strongly energy dependent. Figure 2.16a should be interpreted as a multiple scattering within one atom. Second, a substantial amount of multiple scattering of the diffracted electrons occurs between the atoms of the crystal surface. Figure 2.16b shows multiple scattering between atoms within one plane while Fig. 2.16c& d shows the multiple scattering within planes.

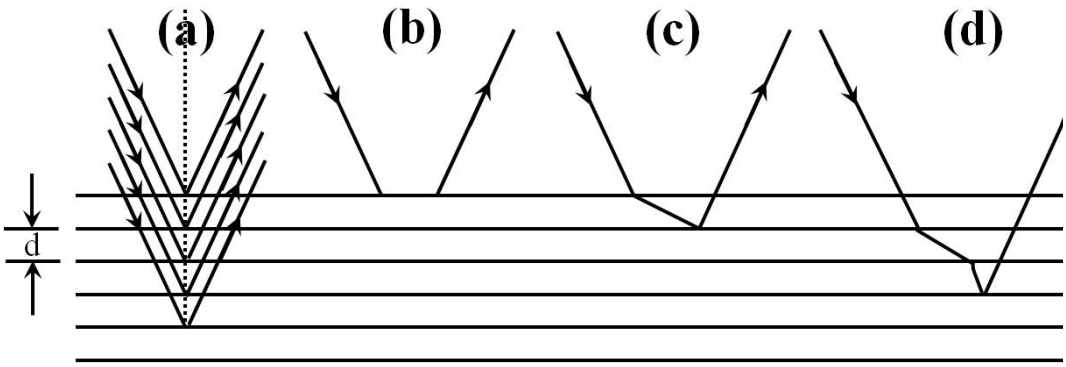

FIGURE 2.16. single scattering process (b-d): Multiple scattering process

The orders of multiple scattering perturbation may create new peaks at new energies comparing to kinematic theory. For example, an I-V curve for the surface structure of bulk truncated face-centered cubic lattice should in the kinematic limit produce a well-ordered sequence of Bragg peaks at predicable energy intervals, see Fig. 2.17a. However, experiments show additional peaks. Thus, multiple scattering process have to be considered in order to correct identify the surface structure.

Figure 2.17d shows a complete multiple scattering can reproduce more peaks rather at Bragg energies than kinematic model.

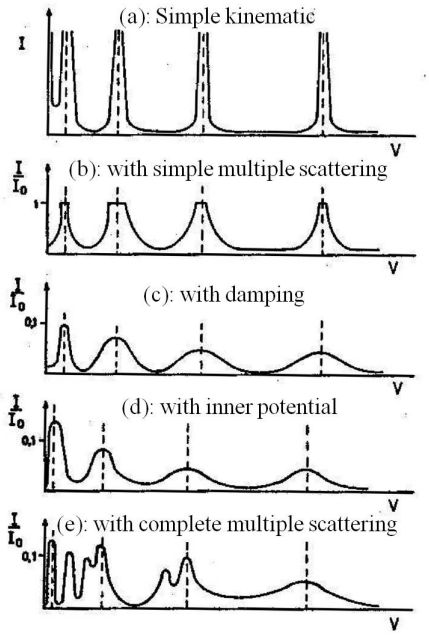

FIGURE 2.17. Demonstration of theoretical calculated I-V curves for model with different approximation. (a) The major peaks can be identified by simple kinematic theory The next three are modified I-V curves by considering with (b) simple multiple scattering, (c) damping, and (d) inner potential. A fully dynamical multiple scattering theory could produce all of the minimum and maximum features in I-V curves in (e). (Figure adapted from reference [71].)

For more details of the multiple scattering process, please refer to reference2 and 1. As a result of these dynamical effects, typically we can not "invert" experimental data directly in order to obtain the surface structure. Rather, a trial-and-error process is implied in LEED calculation.

Tensor LEED calculation.

A perturbation tensor LEED (TLEED) approximation has been developed and implemented by Rouse and Pendry [72] in 1980s. The idea is to make one full dynamical calculation for a reference structure then express the diffraction from modification of this structure in first order perturbation theory. If we move the atoms only by a small amount from reference structure, the perturbation will be

weak and can be calculated by first-order perturbation theory as for the X-ray case. The tensor LEED approximation holds, as long as the atomic displacements from the reference structure are less than 0.2 $\mathring{A}$. Thus, once one reference structure is evaluated, thousands of trial structures within the approximation limit can be calculated in a very efficient manner.

Rp-factor:

During the trial-and-error process, a reliability factor (R-factor) is used to quantitatively measure the agreement between theoretical I-V curves and experimental curves. A variety of different R-factors are defined with different focus on the complex peak structures. Today, the mostly commonly used one is the Pendry R-factor which focuses on the maxima and minima features in the I-V curves rather than the amplitude [73]. The way is to use logarithmic derivative

$$L(E) = \frac{I'}{I} = \frac{1}{I} \times \frac{dI}{dE} \tag{2.34}$$

To avoid the infinite which may give too much emphasis on zeros when intensity equals to 0, a different function *Y(E)* can offer similar emphasis on zeros and peaks as follows:

$$Y(E) = \frac{L^{-1}}{L^2 + V_{oi}^2} \tag{2.35}$$

Where

$$Y_{max} = \pm\frac{1}{2}|V_{oi}| \tag{2.36}$$

when $L = \pm\frac{1}{|V_{oi}|}$.

then for one specific I-V curve, the Pendry R_p-factor is defined in terms of Y functions.

$$R_p = \frac{\int (Y_{gth} - Y_{gexp})^2 dE}{\int (Y_{gth}^2 - Y_{gexp}^2) dE} \tag{2.37}$$

The total R_p-factor for N sets of beams can be calculated by

$$R_p^{all} = \frac{\sum_{i=1}^{N} (R_p)_i \times (\triangle E)_i}{\sum_{i=1}^{N} (\triangle E)_i} \tag{2.38}$$

where ΔE is the energy range of specific beam i. The overall R_p is the average of individual R_p with weight of its energy range. $R_p = 0$ shows perfect correlation and $R_p = 1$ shows no any correlation between theory and experiment. In general, R_p below 0.3 is acceptable and reliable solution for system involving a few atoms in one unit cell. As systems get more complex, the acceptable value may be raised due to the complexity of the system inducing more technical and theoretical inaccuracies.

Once a global minimum R_p has been reached, the trial structure for the global minimum is taken as the actual surface structure. Technically, another round of trial-and-error may need to be taken with this trial structure as the new reference structure. The variance of the top R_p is calculated by:

$$\triangle(R_p^{all}) = (R_p^{all})_{min} \sqrt[2]{\frac{8|V_{oi}|}{\triangle E}} \tag{2.39}$$

where ΔE is the total energy range. The structural parameter t in optimization is in the range of (t-$\Delta t'$,t+$\Delta t'$) where at its minimum or maximum of t:

$$R_p^{all} = (R_p^{all})_{min} + \triangle(R_p^{all}) \tag{2.40}$$

Thus, the error of t can be determined.

Tensor LEED calculation package:

Our LEED calculations were performed using programs derived from the Barbieri/Van Hove Symmetrized Automated LEED (or SATLEED) package [74] with

atomic phase shifts calculated with the optimized muffin-tin (MT) potential approximation [75]. The detail of SATLEED can be found in reference [74]. Let's focus on the modification to the original SATLEED, which is

Optimized muffin-tin potential approximation:

To start the LEED calculation, one has to consider the addition of multiple atomic species and several atoms per unit cell in complex materials complicating the shape of the crystal environment in which the electrons scatter. A common practice is using MT potential approximation. Rundgren introduced an optimized MT potential method [75] which is implied in our modified SATLEED codes. Below is the general introduction of the modification.

In LEED, the optical potential is typically modeled as a constant with a real and imaginary component

$$V_o = V_{or} + iV_{oi} \tag{2.41}$$

The introduction of an imaginary component to the optical potential establishes the life time of an electron

$$\tau = -\frac{1}{2V_{oi}} \tag{2.42}$$

The uncertainty principle, implying the minimum width a feature, can be observed in the diffraction intensity, thus

$$\triangle E \geqslant 2|V_{oi}| \tag{2.43}$$

Hence the peak observed in I-V spectra is directly related to V_{oi}. To model V_{oi}, we consider the "Universal Curve" of electron mean free path in various metals as shown in Fig. 2.18 and establish a phenomenological form for V_{oi} that reproduces

the curve. For the energy ranges in LEED experiments, a simple form for V_{oi}, that reproduces the "Universal Curve" is:

$$V_{oi}(E) = C(\frac{E}{\frac{200}{27.21} + V_{or}})^{\frac{1}{3}} \tag{2.44}$$

The SATLEED code is modified to incorporate this form for V_{oi}, where C typically takes -4 to -5 eV. It is also found that $V_{or}(E)$ has a form of:

$$V_{or}(E) = A_1 + \frac{A_2}{\sqrt{E + A_3}} \tag{2.45}$$

where A_1, A_2, and A_3 need to determined through the fitting of V_0 vs. E curve. The SATLEED code is modified to incorporate the energy dependence of $V_{or}(E)$. Their modification is closed related to the optimized surface-slab-excited-state muffin-tin potential from which phase shifts can be calculated [75].

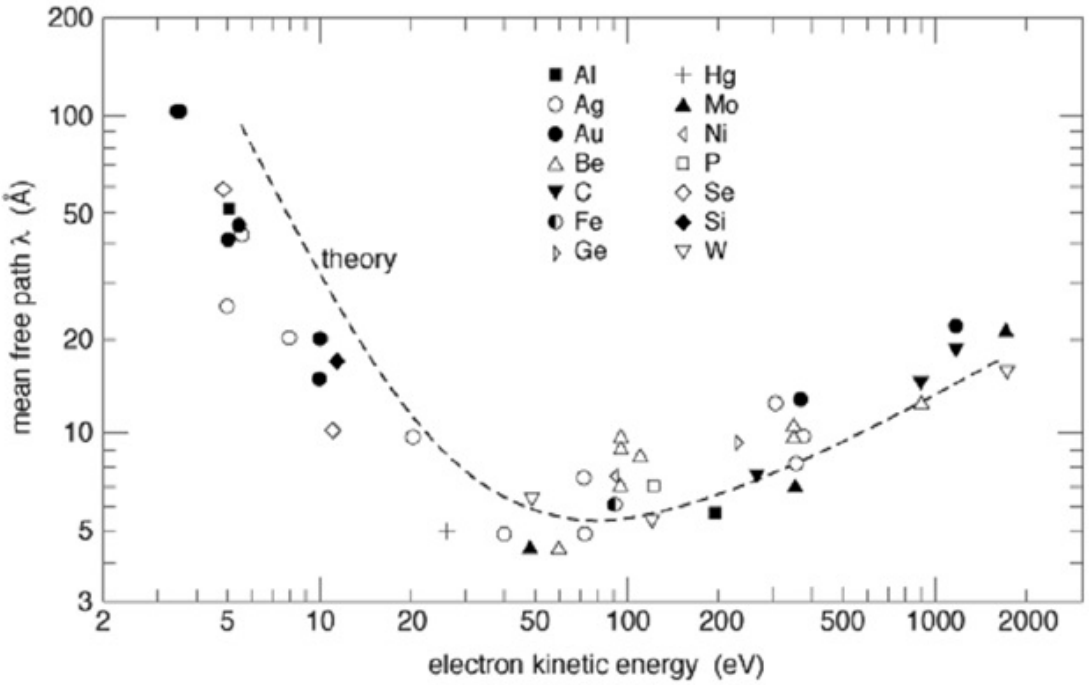

FIGURE 2.18. "Universal curve" of electron mean free path in various metals. Figure adapted from Reference [76]

General procedure of LEED calculation:

The general flow chart for the calculation is in Fig. 2.19. The step 1 is to propose the structure model based on the symmetry from LEED pattern and STM real-space observation. It also involves the consideration from the bulk crystal structure. There are several possible structure model candidates and in principle they all need to be tested to find the minimum of R_p. Step 2 is to define a reference structure with certain structure model (in file *tleed5.i*). The tensor LEED approximation is limited within 0.2 $\AA$ displacement for a valid perturbation theory. Thus, the next reference structure typically moves 0.2 $\AA$ on one particular structure parameter comparing to previous reference structure. Step 3 is to calculate the tensor for the reference structure defined in *tleed5.i*. This is done by *tleed1*. Then step 4 is to calculate the R_p for the reference structure or the structure within tensor LEED approximation limit. At step 5, the R_p is evaluated whether it is a minimum. If it is not, then move one step from the previous structure, and back to step 4 again for R_p evaluation. Until the R_p reaches a minimum then it outputs the structure and all necessary files. Figure 2.20 shows the input and output files and the process of this R_p evaluation. Then we judge the R_p whether it is a local or global minimum. We might need to try several reference structures. Until we have a clear conclusion for the global minimum R_p for this structure model, then we can see whether it is less than 0.3. If not, we need to propose a different new structure model and go through all the process again. If it is less than 0.3, the structure is very likely the correct surface structure but we need to output the structure for further optimization.

The further optimization includes: (1) Optimization of the reference structure to achieve lowest Rp without any further atomic movements (step 6); (2) surface Debye temperature optimization; (3) Error bar analysis. In principle, (1) and (2)

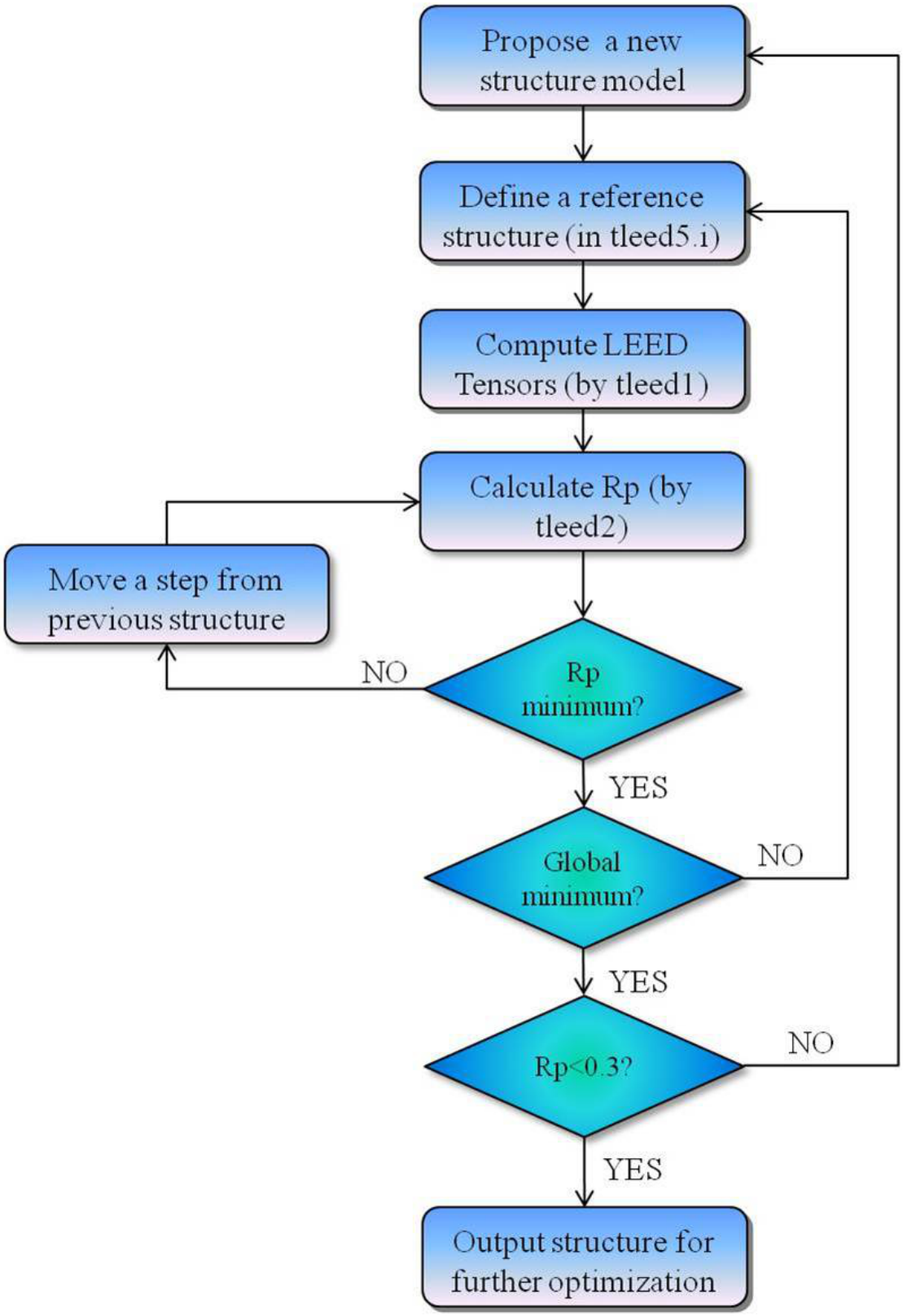

FIGURE 2.19. Flowchart for LEED I-V analysis

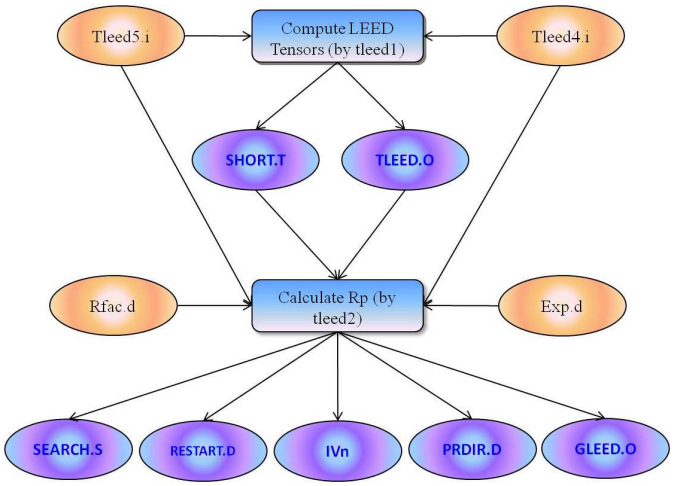

FIGURE 2.20. Diagram of inputs and outputs of TLEED program

need to be done back and force because the surface Debye temperature optimization may change the previous optimized structure or the other way around.

Last we need to consider Debye temperatures. Surface Debye temperature is different than bulk, which is the consequence of creation of a free surface. Typically, the reduction of the top forces is greater at the perpendicular motion than the parallel motion which leads to concept of Debye temperature normal to the crystal surface and parallel to the crystal surface. In kinematic approximation, the intensity of diffracted beams would decrease exponentially with an increase in the temperature of the crystal surface, offering a way to investigate the Debye temperature. The measured "effective" Debye temperature depends on the beam energy and with smaller beam energy ($\sim 50\ eV$) it is more close to surface Debye temperature which is lower than the one in the bulk. In multiple scattering, the Debye temperature is severely distorted and it is not a well-defined measurable quantity because the Debye model is a simplified picture of lattice vibration. In tensor LEED calculation, the surface Debye temperature is obtained by the surface Debye temperature optimization of the trial-and-error full LEED calculation. In later chapters we will show this optimization.

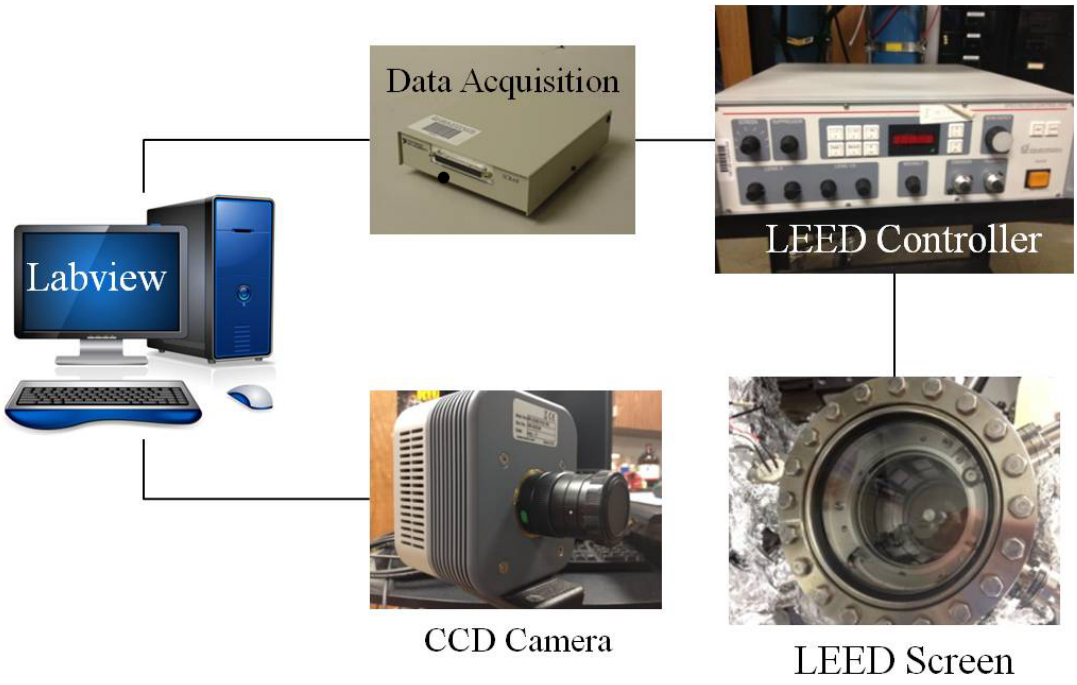

FIGURE 2.21. The diagram of LEED photos acquisition.

Instrument and detail experiments

LEED optics (Omicron) is mounted in a UHV chamber ($<1\times10^{-10}$ Torr) and the sample was on a vertical manipulator with adjustable rotation and tilt. The sample position was adjusted to achieve normal incidence for the primary electron beam. The sample can be cleaved or prepared at various temperatures from room temperature to lowest temperature 20K if using liquid helium. The lowest temperature if using liquid nitrogen is calibrated to 87 K. The diagram for data acquisition setups is in Fig. 2.21. A CCD camera (Andor Technology Mod No. DR-328G-C02-SIL) is controlled by the LabView software to record the LEED photos. A designed data acquisition Equipment (SCB-68) is communicating between the LabView software and LEED controller. LEED controller is carefully tuned to achieve the best LEED pattern with enough contrast of the intensity and good focus. Sample position is carefully tuned to achieve ideal normal incidence. By changing the beam energy, a series of photos is taken on the LEED pattern.

Each photo is a LEED pattern at certain beam energy. I-V curves were carefully extracted by tracking the spots. Each spot will have one I-V curve but the equivalent spots should have the same I-V curves. The sameness could be used to test the validity of the data. The background of the raw I-V curves should be subtracted and smooth is necessary to avoid artificial small peaks. A good reproducible experimental data taken in a wide energy range on a clean surface is critical for determining the structure in LEED I-V analysis.

Chapter 3

Nanoscale Chemical Phase Separation in $FeTe_{0.55}Se_{0.45}$

3.1 Introduction

[77, 78] Among all known Fe-based superconductors, the Fe-chalcogenide $FeTe_{1-x}Se_x$ is structurally and chemically the simplest [79]. Figure 3.1 shows the phase diagram for $FeTe_{1-x}Se_x$, one for the as-grown samples in Fig. 3.1a and one for the annealed samples in Fig. 3.1b. The phase diagram for the annealed samples is similar with iron pnictides. $Fe_{1+y}Te$ is an antiferromagnetic metal with a monoclinic structure below 65 K [81], while $FeSe_{1-\delta}$ is a superconductor with an orthorhombic structure in the ground state [79]. The AFM order in parent FeTe is bicollinear, characterized by an in-plane propagation wave vector $Q_m = (\pi,0)$[81, 82] rather than collier AFM order in iron pnictides. What makes $FeTe_{1-x}Se_x$ particularly interesting and unique is that superconductivity results from isovalent doping of Se for Te which presists over a wide doping range (x) [83, 84].Optimal superconducting transition occurs close to 50% mixture of Se and Te, while other compounds require only a small amount of doping for reaching the highest T_c [85]. AFM seems overlap with superconductivity. The superconductivity is characterized as weak superconductivity because of the small superconducting volume. Because as-grown samples have unavoidable excess Fe atoms thus make the region of weak SC controversial [84, 86, 102]. It is believed that annealing reduces the amount of excess Fe atoms [86] but oxygen may play a role in the bulk superconductivity [102].

As shown in Fig. 3.2a, the material is composed of Fe-chalcogenide slabs stacked together without any spacing layer. In many ways, the isovalent substitution can be viewed as a chemical pressure. In many families of transition-metal compounds,

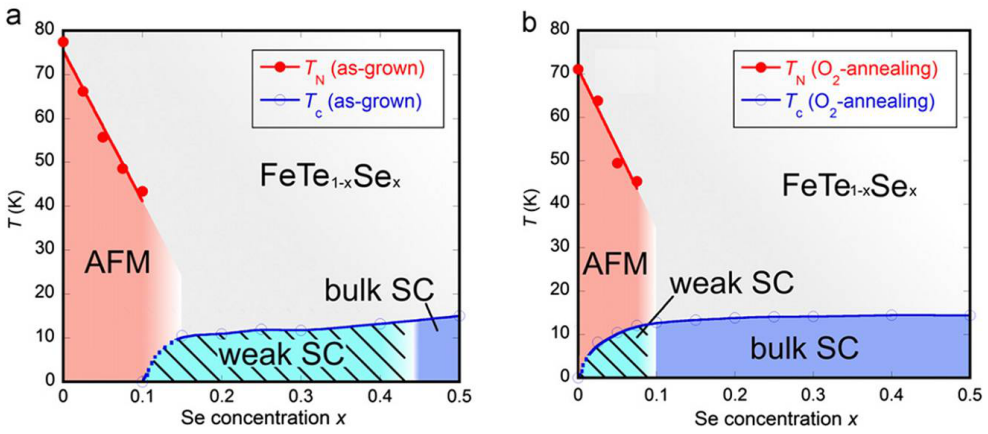

FIGURE 3.1. Phase diagram of the $FeTe_{1-x}Se_x$ for as-grown samples in (a) and plus O_2 annealing in (b). Note that the weak superconducting region is significantly reduced after O_2 annealing.Figure adapted from reference [102]

it is believed that the chemical substitution is completely random, which is refereed as homogeneous doping. However, the electronic structure appears inhomogeneous with doping thus generating many interesting phenomena, due to strong electron correlation in these materials [9]. At present, there is very little information about the distribution of Te and Se in $FeTe_{1-x}Se_x$. To address this issue, we have used scanning tunneling microscope/spectroscopy (STM/STS) to investigate the spatial dependence of the structural and electronic properties for $FeTe_{1-x}Se_x$ with $x = 0$ and 0.45. For $x = 0.45$, Te and Se atoms can unambiguously be distinguished. Statistical analysis allows us to identify the two sites, and to conclude that the distribution is not random. Interestingly, the STS measurements show that the local electronic density of states is the same everywhere in the normal state on the ordered surface (away from defects). After presenting the data we will present a model for the origin of this behavior and discuss the relationship between the size of the phase separation and the coherence length in the superconducting phase.

Single crystal samples of $FeTe_{1-x}Se_x$ were grown by the self-flux method as described previously [87]. The sample compositions were determined using the energy dispersive X-ray spectroscopy. The measured superconducting transition

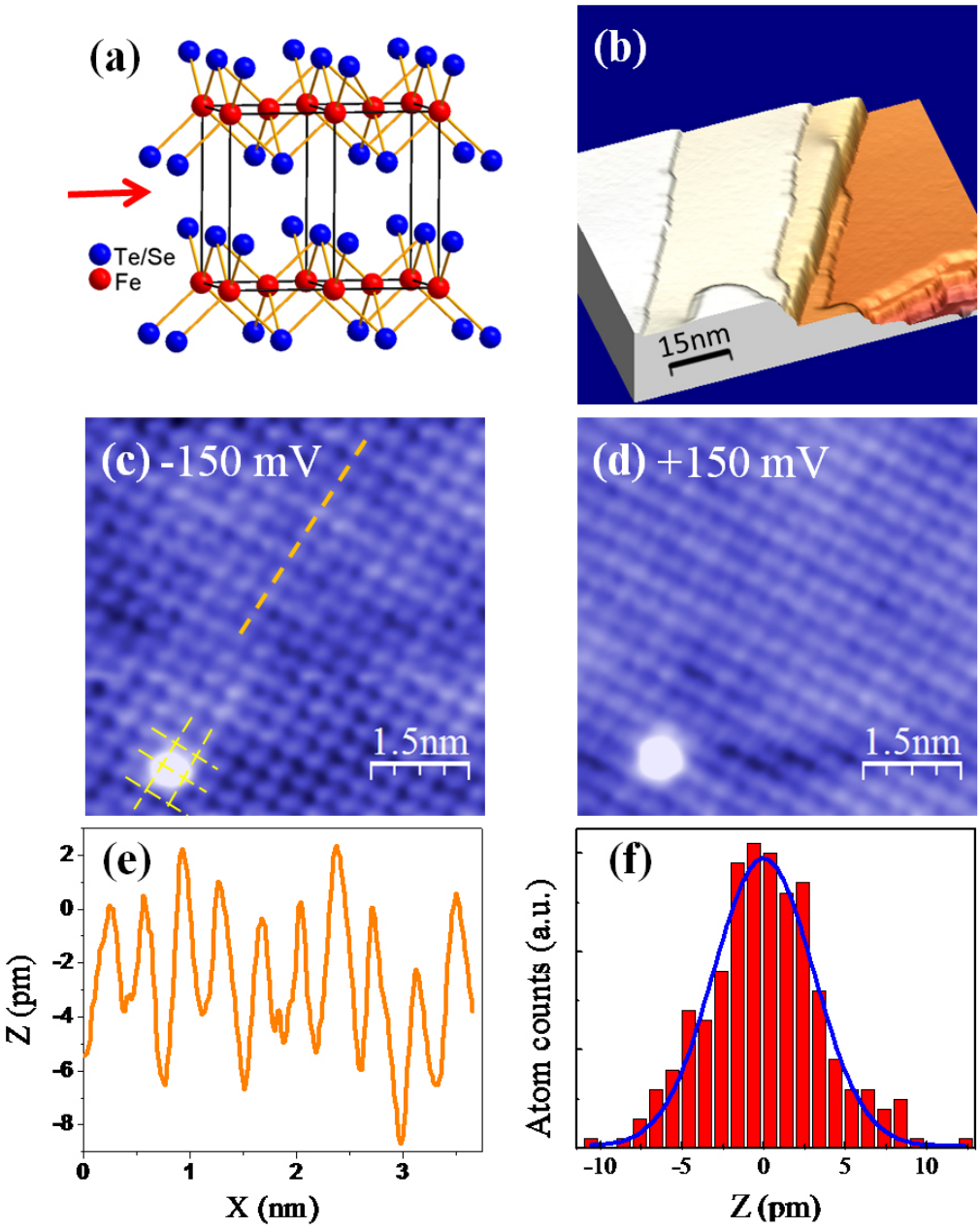

FIGURE 3.2. (a) Bulk crystal structure of $FeTe_{1-x}Se_x$ and the cleavage position marked by arrow; (b) 3D view of a constant-current STM topographic image of the cleaved FeTe surface showing large atomically flat terraces and steps by using a sample bias $V = 800$ mV and tunneling current $I = 200$ pA; Zoom-in (c) filled-state and (d) empty-state STM topographic images on the same location of cleaved FeTe surface (59Å×59Å) with the tunneling current $I = 500$ pA; (e) Line profile for the dashed line marked and (f) Histogram of imaged atom heights in (c). The solid curve is the fitting result to a Gaussian distribution.

temperature in the optimally doped compound $FeTe_{0.55}Se_{0.45}$ is 14 K with a specific heat jump [88], indicating bulk superconductivity. The samples were cooled to 80 K with liquid nitrogen in a homemade low-temperature STM, and then cleaved *in situ* to acquire a fresh *ab*-plane surface. Figure 3.2b shows the cleaved FeTe surface with large atomically flat terraces terminated by a step of either single or multiple layer step height of bulk lattice constant $c = 6.3$ Å. This assures that the crystals cleave between Fe-chalcogenide layer so that the surface is Te layer for FeTe or mixed Te/Se layer for doped compound. The surface crystallographic properties are measured using low energy electron diffraction (LEED), which reveled a highly ordered surface, the same symmetry as the bulk, and a 0.07 Å compression of the Te-Fe-Te surface tri-layer. The vacuum during cleavage and STM/STS experiment was better than 5×10^{-11} Torr. All data presented were obtained at 80 K. The STM tip was tungsten and checked on a clean single crystal gold *in situ* before acquiring STM/STS data on Fe-chalcogenides. The tunneling conductance spectra dI/dV was obtained with a lock-in amplifier. The d^2I/dV^2 was acquired by numerical differentiation of the measured dI/dV characteristics.

3.2 Surface Geometric Structure of FeTe and $FeTe_{1-x}Se_x$

3.2.1 Parent FeTe

Figure 3.2c and 3.2d show the atomically-resolved STM images with opposite-polarity bias on the same location of a cleaved FeTe surface. They are similar to previous STM studies of Fe-chalcogenides [89, 90, 91], where no reconstruction is observed. The lattice constant estimated from Fourier transform of the image is $\sim$ 3.8 Å, in good agreement with that obtained from the bulk [87]. The protrusions observed in the STM images correspond to the apical chalcogen atoms (Te) above the Fe plane in the tetrahedral building blocks. There are almost no vacancies

observed on the surface. We note few "big bright spots" that are randomly distributed on the surface. These are assumed to be excess Fe atoms [89, 90]. These "big bright spots" are located at the bridge site of the surface lattice, which is consistent the results of X-ray diffraction refinement [87] and density functional investigation [92].

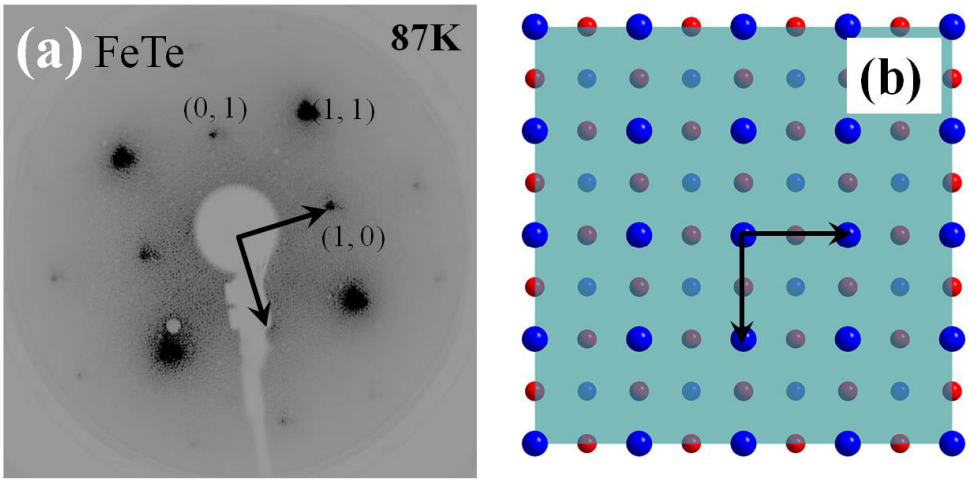

FIGURE 3.3. (a) LEED pattern for parent compound FeTe. (b) Top view of bulk-truncated Te-terminated surface without any reconstruction.

A conspicuous feature of the cleaved FeTe surface is its extreme flatness. Fig. 3.2e presents the line profile marked in Fig. 3.2c, which allows us to estimate that the surface corrugation is less than 8 pm. Different bias STM images show similar small corrugation. Though with smaller atom density (larger lattice constant), the surface corrugation of FeTe is 4-5 times smaller than the noble metal surface like Cu(100) [93], indicating the itinerant characteristic of the electrons on the surface. We have carried out the statistical analysis in order to more quantitatively characterize the surface corrugation [94]. By using the mean vertical position of imaged Te atoms as the reference, a histogram of atom height (z) extracted from Fig. 3.2c is presented in Fig. 3.2f. The appearance of single peak in the histogram confirms a single kind of atoms (Te) on the ordered FeTe surface.

LEED experiments generate a (1×1) pattern in Fig. 3.3a. The indices of integer spots are marked and there are no fractional spots, indicating no surface reconstruction. It is consistent with STM images in Fig. 3.2. The crystal is unlikely to be cleaved at Fe layer which has a smaller periodicity than Te layer. Thus, the symmetry from LEED patterns and real-space STM images lead to a Te-terminated surface model without surface reconstruction in Fig. 3.3b.

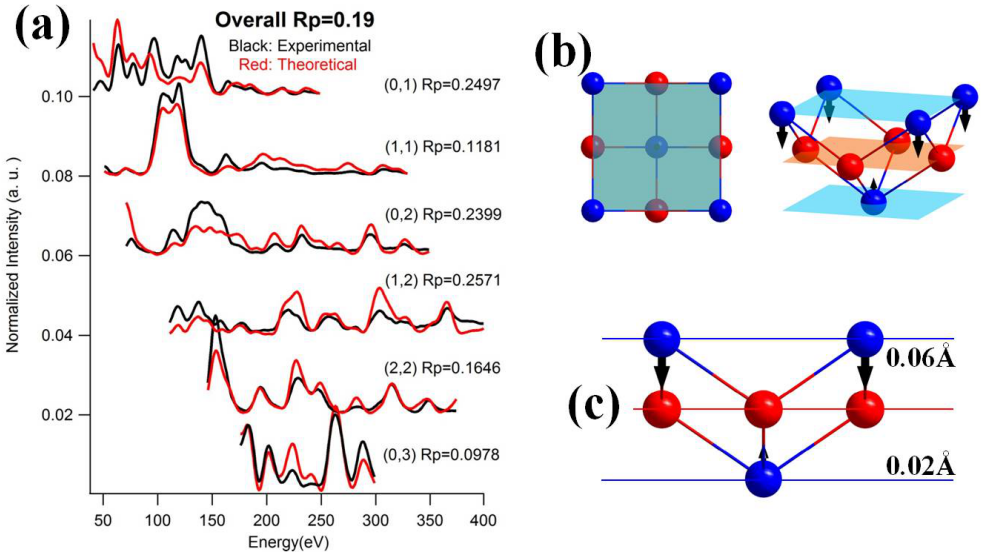

FIGURE 3.4. (a) Comparison of experimental LEED I-V curves to theoretical I-V curves. (b): Top view (left) and 3-D view (right) of one tetragonal-(1×1) unit cell demonstrating the surface relaxation. (c) Side view of the surface relaxation.

Total six LEED I-V curves are collected with total energy range 1421eV. The result of I-V analysis is shown in Fig. 3.4a. With Te-terminated structure model, the theoretical I-V curves can fit experimental I-V very well, i. e. R_p is better than 0.19. The resultant structure is shown in Fig. 3.4b for the top and 3-D view and Fig. 3.4c for the side view. It shows that the top Te layer has 0.06 Å inward motion to the bulk and the bottom Te layer has 0.02 Å outward motion. Fe layer keeps the same position as the bulk.

Figure 3.5 shows the error bar analysis. Using Eq. 2.36 with V_{oi} is 5.0 V, and ΔR_p is estimated to 0.03. Then we fix the lattice in the optimized structure, gradually change one structure parameter in the step of 0.01Å, and calculate out the corresponding R_p for each position. The R_p vs. displacement was plotted out in Figure 3.5. We cut off at R_p equals to 0.23 then we got the error on each structural parameter. The error bars estimated from Fig. 3.5 shows that the top Te layer for sure has relaxation. The bottom Fe plane and Te plane may not have any relaxation. This is under our expectation since the outmost layer always has a larger relaxation.

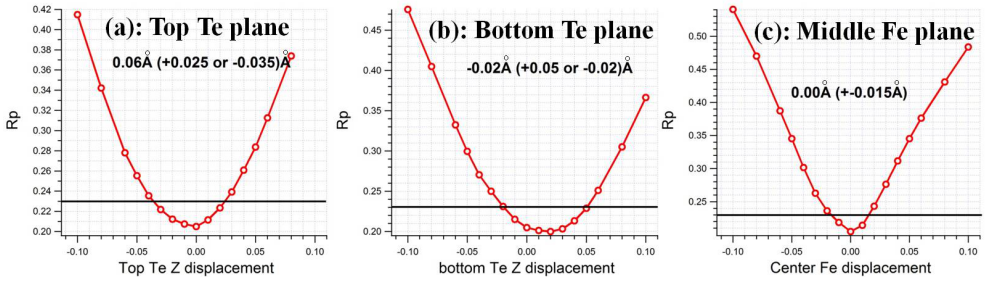

FIGURE 3.5. Error bar analysis on the top Te plane, middle Fe plane and bottom Te plane.

3.2.2 $FeTe_{0.55}Se_{0.45}$

We now turn to the optimally doped $FeTe_{0.55}Se_{0.45}$. The STM images with different bias-voltages are shown in Fig. 3.6a& 3.6b. Similar to FeTe, there are few vacancies on the surface presumably indicating the high crystal quality. However it is clear that there are two types of atoms, "bright" and "dark", forming irregular small "patches/domains". As displayed in Fig. 3.6c, there is a considerable height difference of $\sim$ 47 pm between these two kinds of patches. On the other hand, the atomic corrugation within a single patch of either "bright" or "dark" atoms (see the line profiles in Fig. 3.6d) is comparable to that of FeTe surface. Since the adjacent atom layers (i.e., between Fe and Te/Se) are 1.48 - 1.72 Å apart in $FeTe_{0.55}Se_{0.45}$

[87, 95, 96], these "dark" patches of atoms should not be the beneath Fe atoms but be within the same Te/Se layer. Note that similar images were obtained in previous STM studies on the doped compounds [90, 91]. Both filled-state or empty-state images show very similar contrast of two groups of atoms. This indicates that the height difference in the STM images of $FeTe_{0.55}Se_{0.45}$ mainly comes from chemical (or crystallographic) contribution rather than an electronic effect.

TABLE 3.1. The two Gaussian peak fitting results of the histograms in Fig. 3.7a- 3.7d, including the height difference (Δz), percentage of normalized area of each peak, as well as their average values

Fig.	Bias(mV)	Δz (pm)	Peak I(%)	Peak II(%)
3(a)	-150	-40.9	54.6	45.4
3(b)	+150	-51.8	53.2	46.8
3(c)	-200	-36.9	54.4	45.6
3(d)	+200	-49.1	52.8	47.2
Ave.		-44.7±12.0	53.8±1.5	46.2±1.5

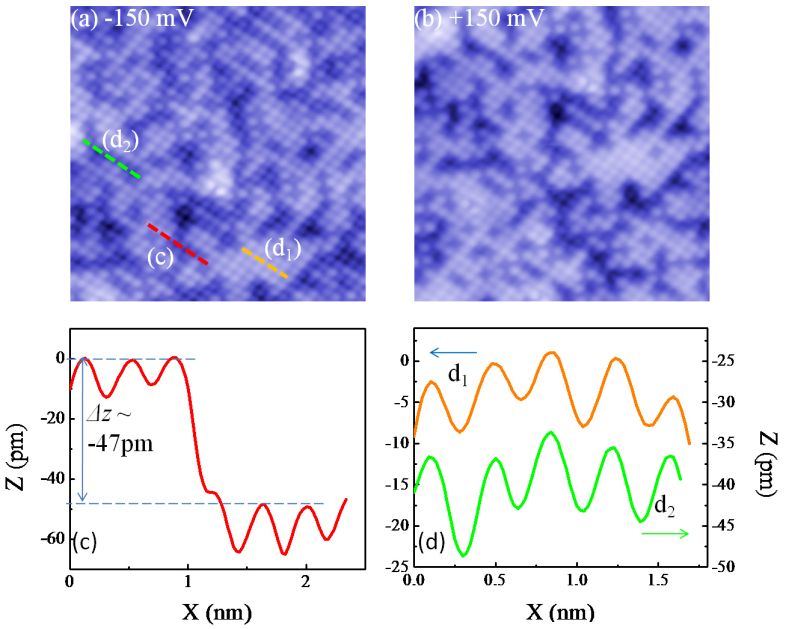

FIGURE 3.6. (a-b) Constant current STM topographic images (111Å×111Å) of $FeTe_{0.55}Se_{0.45}$ surface with different bias voltages but identical tunneling current I of 1.3 nA. (c) Line profile across different patches of atoms and (d) Line profiles on both a "bright" and "dark" atom patches marked in panel (a)

3.3 Nanoscale Chemical Phase Seperation of Te and Se Atoms

To gain more insight into the nature of these two types of imaged domains, we extract the relative height of every atom in STM topographic images of cleaved $FeTe_{0.55}Se_{0.45}$. The histograms are shown in Fig. 3.7. Similar to the analysis for FeTe surface, we use the mean position of "bright" atoms as the reference. There exists a double-peak distribution associated with the distinct two types of surface atoms, in contrast to the single peak appearance in the histogram for FeTe surface (see Fig. 3.2f). The solid curves in Fig. 3.7 are the fittings using Gaussian distributions. As listed in the Table 3.1 for the fitting results, the area ratio of higher to lower peak, i.e., the ratio of "bright" to "dark" atoms, is (53.8%:46.2%). This is very close to the ratio of Te to Se in the bulk (55%:45%). We thus identify the "bright" atoms as Te, and the "dark" ones as Se, respectively. As shown in Fig. 3.7 and Table 3.1, the apparent height difference between Te and Se atoms in the same layer is $44.7 \pm 12.1\ pm$ in the STM images, which is larger than the results from extend X-ray absorption fine structure spectroscopy [95] and X-Ray/neutron diffraction [96, 97]. The larger value obtained from the STM measurements could be simply a consequence of the details of the tunneling experiment or due to a surface relaxation.

Our high resolution STM images clearly reveal a nanophase separation between Te and Se atoms in $FeTe_{0.55}Se_{0.45}$, in sharp contrast with normally expected picture for a random alloy. To test this we counted the number of Te nearest neighbors (NN) for every Se atom in many of our STM images of $FeTe_{0.55}Se_{0.45}$ surface. We found that the NN count gives a value of ~ 1.7, in contrast with the value of 2.2 expected for this concentration of a completely random alloyed $FeTe_{0.55}Se_{0.45}$. Both Te and Se atoms prefer to form small patches, rather than random distribution on

the surface. With the NN count value ($\sim$ 1.7), the estimated average patch size is consistent with the experimental observation of $\sim$ 1 nm^2 which contains 9-10 atoms on surface.

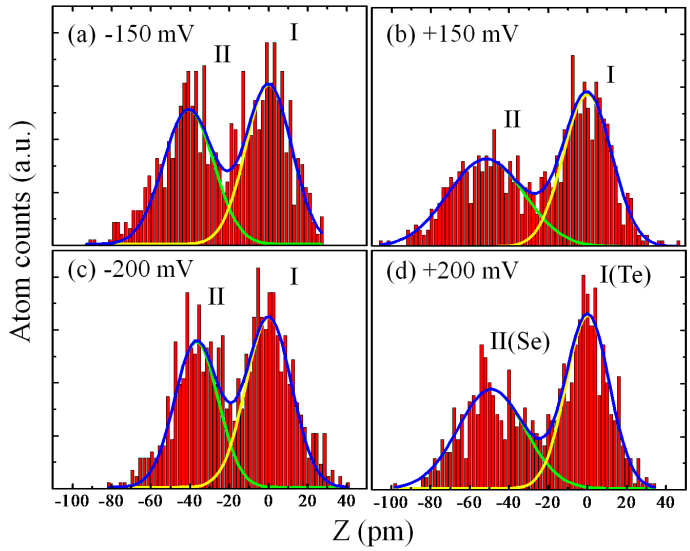

FIGURE 3.7. (a-d) Histograms of atom heights corresponding to the bias-dependent STM topographic images respectively. The solid curves are the results by fitting to two Gaussian distributions. In each panel, the yellow (I)(light gray) and green (II)(dark gray) peaks correspond to "bright" and "dark" atoms in the image, respectively, and the blue (darkest gray) curve is the envelop sum of two peaks.

This configuration would lead to a local inhomogeneity in chemical pressure, which could drive a local structural change. In the ground state, the structure of FeTe is monoclinic while the structure of FeSe is orthorhombic. The central question is, do the electronic properties including superconductivity respond to the local chemical (crystallographic) inhomogeneity? To gain insight into this critical issue, we have measured the dI/dV spectra on individual Te and Se atoms, as well as the average dI/dV spectra on their associated patches. The results are shown in Fig. 3.8 for both $FeTe_{0.55}Se_{0.45}$ and FeTe surfaces. Note that, in the energy window of ± 100 mV around Fermi surface (Fig. 3.8a and 3.8b), all the individual dI/dV taken on Te and Se sites on the $FeTe_{0.55}Se_{0.45}$ surface are indistinguishable.

To further confirm this, we have taken many more spectra at the surface on the same STM image (Fig. 3.8a) and averaged all the spectra taken from Te (Se) atoms/patches, respectively. The two averaged dI/dV spectra, one from Te and other from Se, are identical as shown in Fig. 3.8c, independent of the local chemical environment. The earlier report of spatial variations in the dI/dV spectra at high energy [90] is likely due to the excess Fe. For comparison, the tunneling spectra of FeTe surface is also presented. The pronounced feature in the dI/dV of FeTe is the enhanced local density of states (LDOS) around 20 mV as compared with $FeTe_{0.55}Se_{0.45}$. The difference in the electronic properties between them is best displayed in Fig. 3.8d where the d^2I/dV^2 spectra are presented. The most obvious differences are the position at the zero bias ($V = 0$) and the peak around 20 mV in the parent compound.

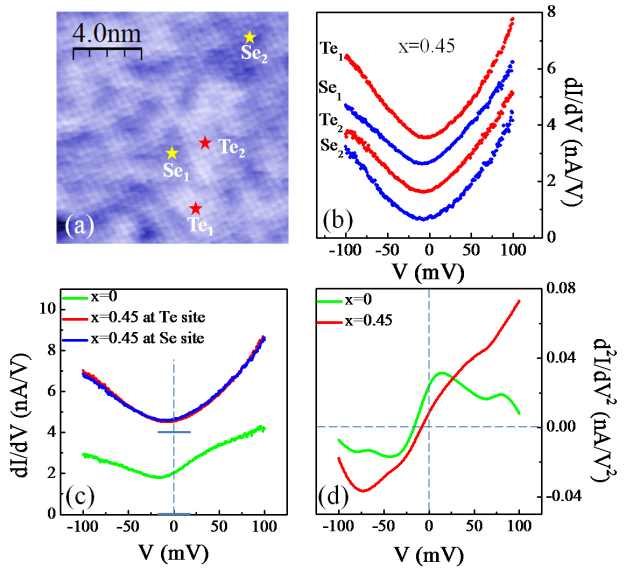

FIGURE 3.8. (a) A 128Å×128Å constant current STM topographic image on $FeTe_{0.55}Se_{0.45}$ surface. I = 1.5 nA, V = -100 mV; (b) Tunneling spectra taken at several Te and Se sites indicated in (a). Curves are vertically shifted for clarity; (c) Averaged dI/dV spectra at Te and Se sites on $FeTe_{0.55}Se_{0.45}$ surface in (a) and on FeTe surface. The spectra are also shifted for clarity, with the zero value of dI/dV marked by solid lines. (d) the corresponding d^2I/dV^2 curves acquired by numerical differentiation of the measured dI/dV spectra in (c). All the data were taken at 80 K.

The data presented here reveals a unique feature: inhomogeneous chemical distribution giving rise to homogeneous electronic behavior. What has been expected for many doped correlated electron materials is just the opposite: chemical homogeneity but electronic and magnetic phase separation [9]. Electronic homogeneity and very small corrugation in the STM topograph coupled with the nearly homogeneous superconducting gap [90, 91] indicate that this compound is closer to an itinerant metal than to a highly correlated material. Superconductivity in this compound with nanscale chemical phase separation must be a consequence of the fact that the sizes of chemical patches are smaller than the superconducting coherence length resulting in a homogenous superconducting gap.

What may have occurred for $x \sim 0.5$ is that Te and Se nanscale phases compensate each other in the tri-layered structure (see Fig. 3.2a). This is that, everywhere we see a Te patch on the surface, there could be a Se patch underneath the Fe in the third layer. Thus, the Se/Te concentration in the triplet layer system is nearly homogeneous. If this is the case, the follow-up question is what is the chemical and electronic behavior in doped $FeTe_{1-x}Se_x$ when x is away from $\sim 50\%$? For example, electrical resistivity shows both weakly localized electronic behavior and filamentary superconductivity for $0.1 < x < 0.3$ [84]. Is this caused by large-scale chemical inhomogeneity which leads to electronic inhomogeneity or by random chemical distribution generating strong scattering which leads to weak localization? This can only be answered by further STM/STS investigation.

In summary, scanning tunneling microscopy and spectroscopy have been performed with Fe-chalcogenides FeTe and $FeTe_{0.55}Se_{0.45}$, respectively. In both cases, the cleaved surfaces are chalcogen terminations without reconstruction. A very small corrugation is measured for cleaved FeTe surface. Mixed Te and Se atoms in $FeTe_{0.55}Se_{0.45}$ can be identified in STM topography by statistical analysis, con-

sistent with that found in bulk. Furthermore, direct evidence of local chemical inhomogeneity in Fe-Te/Se layer of $FeTe_{0.55}Se_{0.45}$ is found with significant height difference between Te and Se atoms, leading to larger surface corrugation. In contrast to the nanoscale chemical phase separation, the local electronic properties revealed by tunneling spectroscopy show no sign of inhomogeneity.

Chapter 4
(1×2) stripe surface of (Ba,Ca)($Fe_{1-x}Co_x$)$_2As_2$

4.1 Introduction

Compared to $FeTe_{1-x}Se_x$ system, structurally there is an intermediate layer of A atoms separating Fe_2As_2 planes in $A122$ compounds where A=Ba, Sr, Ca [98]. Electronically, there are two electrons transfering from A layer to Fe_2As_2 layer in one tetragonal unit cell. Their phase diagram is similar to $FeTe_{1-x}Se_x$ but what is more interesting is that there is a concurrent structural and magnetic transition in the parent compound of $A122$ system [22, 99] (see phase diagram of Ca122 in Fig. 4.1 as an example): from tetragonal-paramagnetic (Tet-PM) to orthorhombic-antiferromagnetic (Ort-AFM). This is a sign of a strong coupling between spin and lattice in $A122$ compounds. Besides chemical doping, the application of hydrostatic pressure lowers both the structural and magnetic transition temperature. For example, it was shown in $BaFe_2As_2$ that the application of a critical uniaxial pressure of 0.7 *MPa*, beyond the pressure needed to detwin the sample, dramatically increases the coupled transition temperature [100]. A modest hydrostatic pressure of 0.35 *GPa* suppresses the first order transition in $CaFe_2As_2$ from Tet-PM to Ort-AFM. It is replaced by a first order transition to a low temperature-collapsed tetragonal nonmagnetic phase [7]. Surface lattice dynamics measurements in Ba122 clearly indicate that the presence of a surface raises the transition temperature [28], suggesting that the properties at the Ba122 surface may mirror the bulk under extreme/pressure conditions.

The relationship between AFM and SC is also intriguing in $A122$ compounds, especially in Co-doped (Ba,Ca)122. In other systems, a superconducting dome exists

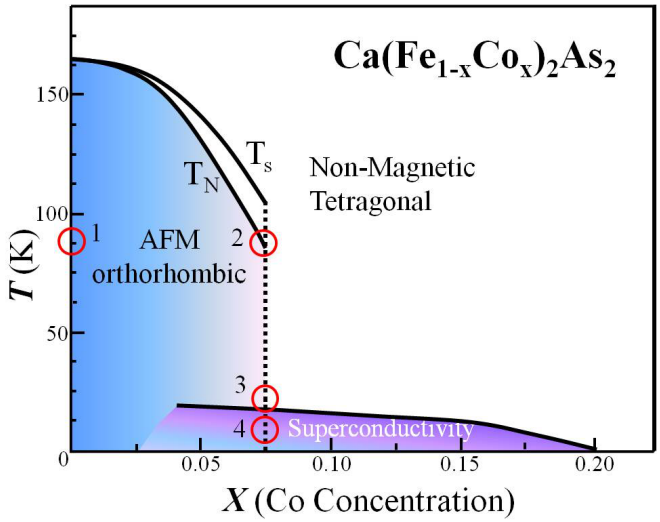

FIGURE 4.1. Phase diagram of $Ca(Fe_{1-x}Co_x)_2As_2$. Black lines are boundaries separate each phase. T_s and T_N represent structural and magnetic transitions, respectively. Circle 1 & 2 are where LEED experiments are taken and circle 3 & 4 are where STM experiments are taken.

after the AFM is completely suppressed ($SmFeAsO_{1-x}F_x$ [2] and $CaFeAsO_{1-x}F_x$ [101]) or there seems to be an overlap ($FeTe_{1-x}Se_x$ [102], $Ba_{1-x}K_xFe_2As_2$ [103], $Ba(Fe_{1-x}Co_x)_2As_2$ [22]). $Ca(Fe_{1-x}Co_x)_2As_2$ [99] is an example of an apparent overlap of superconducting and antiferromagnetic (AFM) phases without a clear superconducting dome in the underdoped region (Fig. 4.1). X-ray and neutron scattering studies argue that AFM and SC coexist and compete with each other in $Ba(Fe_{0.953}Co_{0.047})_2As_2$ evidenced by the suppression of the low energy spin excitations together with the reduction of the static moment [104]. Recent studies on both underdoped powder and single-crystal samples reported the microscopic coexistence of the two forms of orders in $Ba_{1-x}K_xFe_2As_2$ [105, 106]. All of these measurements are averages over the bulk, which could be phase separated. Thus, measurements of the local geometric and electronic structure using, for example, scanning tunneling microscopy/spectroscopy (STM/S) to probe the local behavior [29], are needed.

STM/STS is a surface tool, and it is essential to understand what role the surface plays [107]. Topographies of $BaFe_2As_2$ show that the surface is stabilized by an enhanced orthorhombicity (discussed in Chapter 5 [108]). The $(\sqrt{2}\times\sqrt{2})$R45° domain structure at $BaFe_2As_2$ surface is further locked to AFM ordering, indicated by broken mirror symmetry at the domain boundaries, which stabilizes the bulk spin fluctuation [109]. This leads to a higher surface phase transition temperature [28]. Interestingly, a superconductivity gap is observed from this surface [110]. Recently, STM studies on $K_{0.73}Fe_{1.67}Se_2$ have speculated that the superconductivity is observed on the surface with a charge order resulting from the block-AFM ordering of the Fe layer [111]. Another STM study on $NdFe_{1-x}Co_x$ speculated that the spin density wave gap coexists with SC gap at the surface [112]. However, to figure out whether these phenomena are associated with the bulk or surface properties, it is important to start with a detailed understanding of the surface structure and then its interplay with its properties.

Cleaving *A*122 layered compound typically produces two competing reconstructed phases: $(\sqrt{2}\times\sqrt{2})$R45° and (1×2) stripe phase [109, 113, 64, 115, 89, 116, 117, 118, 119]. The symmetry notation is with respect to the high temperature tetragonal phase. These two competing surface phases complicate the determination of the surface structure. For instance, STM and LEED studies of Ba122 compounds have led to conflicting conclusions [89, 116, 117, 118, 119, 110]. Fortunately, for Ca122, the (1×2) stripe phase dominates. The first step is to determine the structure using LEED I-V analysis, and then compare the experiment to first-principles calculation.

In this chapter, we present a spatially-resolved coexistence of superconductivity and AFM order on the (1×2) stripe phase at the surface of Co-doped Ca122 by combing STM/S with low energy electron diffraction (LEED), and density func-

tional theory (DFT) calculation. This combination allows us to address the coupling between spin, charge and lattice at the stripe surface of Ca122 compounds. The (1×2) reconstructed surface is a half monolayer Ca with a surprisingly large inward relaxation (~ 0.5 $\mathring{A}$), and the As-Fe_2-As layer displays a significant buckling. Spin dependent first-principles DFT calculations reproduce the experimental findings if and only if the surface possesses bulk AFM ordering. Furthermore, the charge distribution is shown to be very sensitive to the configuration of the lattice and spin. Superconductivity is found at this surface by STS, thus coexisting with AFM ordering. Last, similar conclusion has been found on the stripe phase of Ba122 compounds.

4.2 Spin-lattice-charge coupling at the stripe surface

4.2.1 Experiments: STM and LEED

Single crystals of $Ca(Fe_{1-x}Co_x)_2As_2$ ($x = 0$ and 0.075) were grown out of Sn flux, as described previously [120]. Magnetic susceptibility and electrical resistivity measurements show the bulk magnetic/structural transition temperature is $T_{N/S} \sim 170$ K for the parent $CaFe_2As_2$. For the 7.5% Co doped compound, the bulk magnetic transition is $\sim$ 90K while structural transition is $\sim$ 100 K. Superconductivity occurs at a transition temperature Tc ~ 19 K. Fig. 4.2a is the Ca122 bulk low temperature orthorhombic crystal structure with AFM ordering (Ort-AFM) showing that Ca planes separate the As-Fe_2-As layers. There are two atoms in each Ca and As plane and four in Fe plane in one unit cell. The spins are coupled antiferromagnetically along the long in-plane axis a and axis c but coupled ferromagnetically along b axis, which is the so-called collinear AFM ordering. Fig. 4.2b is the top view of bulk-truncated Ca layer, where the orthorhombic lattice is shown by black lines and the axis vectors are indicated by the black arrows. The bulk orthorhom-

bicity of *(a-b)/(a+b)* is very small for Ca122, $\sim$ 0.5% [24]. Figure 4.2c shows a superlattice which is the major topic of this chapter but it is inconvenient to use orthorhombic notation. If using tetragonal notation, it can be defined as (1×2) supercell. From a practical point of view, since the orthorhombicity is so small, using a tetragonal notation or lattice parameter in STM and LEED analysis does not make a difference.

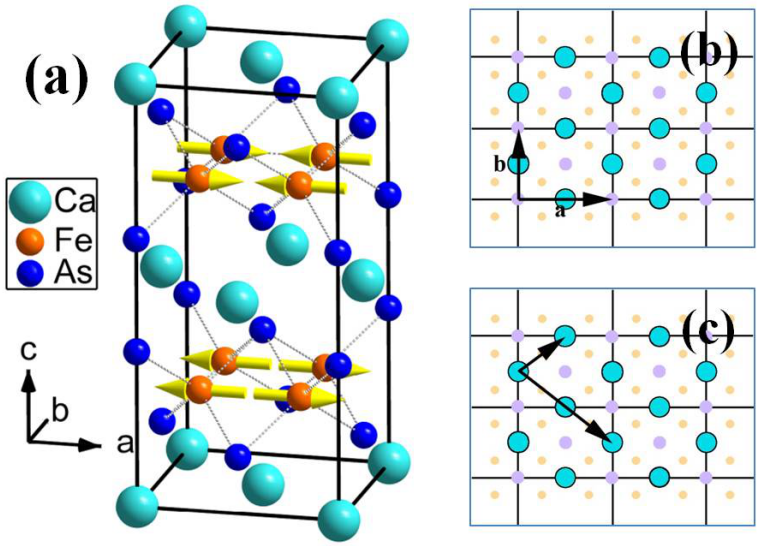

FIGURE 4.2. Schematic View of the structure for Ca122 (a) Bulk low temperature orthorhombic crystal structure and spin structure. The yellow arrows represent the magnetic moment directions. (b-c) Top views of Bulk-truncated at Ca layer for orthorhombic structure. Note that the black arrows in (b) are the orthorhombic unit cell axis vectors while in (c) they illustrate a (1×2) unit cell (in tetragonal notation).

STM image taken at 80 K in Fig. 4.3a shows a stripe-like surface. The rows of atoms (stripes) have a spacing of $\sim$ 8 $\mathring{A}$, which is $\sim$ 2 times the tetragonal lattice constant a $\approx$ 4 $\mathring{A}$. It is hard to resolve the atomic corrugation along stripes. Thus, it is not clear from this image what the spacing along stripes is. The Fourier transform of this STM images shows weak peaks along stripes associated with a lattice spacing of one tetragonal lattice constant. A lower temperature STM at 4.3 K on Co-doped Ca122 shows a 4 $\mathring{A}$ periodicity along stripes [64]. The same periodicity is also seen in Sr122 [114] and Ba122 [110]. Thus, the stripe phase is

a (1×2) reconstructed surface, with the unit cell indicated by the white rectangle in the inset of Fig. 4.3a. Note that STM cannot resolve the small distortion ($a \neq b$) induced by the bulk orthorhombicity. Other STM images show that the typical topographic features include the dark missing lines, bright surface additional lines, anti-phase domains, twin domains, some of which will be demonstrated later.

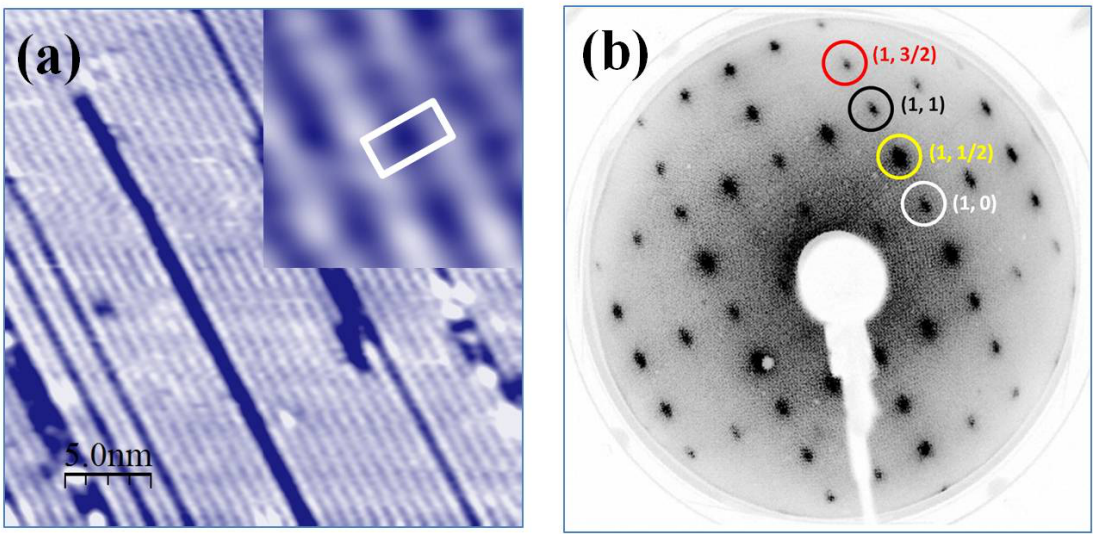

FIGURE 4.3. (a)STM topography of stripe-ordered surface on $CaFe_2As_2$ at (1V, 200pA). Inset is the zoom-in image with red rectangle showing a (1×2) unit cell.(b) LEED pattern on surface of $CaFe_2As_2$.

A LEED pattern obtained with electron beam energy of 120 eV at 87 K in Fig. 4.3b shows fractional spots that appear only in the middle of two nearest integer spots in axis direction, in additional to a tetragonal LEED pattern. They are identical to LEED pattern (Fig.2.13h in Chapter 2) simulated from a (1×1) lattice with (1×2) twin domains. The indices of some of the spots are marked with circles. The integer spots (1, 0) and (1, 1) are marked by white and black circles, respectively. The fractional spots (1, 1/2) and (1, 3/2) are marked by yellow and red circles, respectively. Thus, there is a (1×2) superlattice in real-space. Because the fractional spots are seen at both directions, the surface should

have two perpendicular domains, just as demonstrated in Fig. 2.11d in Chapter 2. The LEED pattern is consistent with STM images.

The fractional spots are extremely sensitive to experimental conditions. They are fragile and their existence and sharpness are sensitive to temperature, vacuum, thermal processing, and LEED electron beam energy. Room temperature cleaved samples only shows (1×1) tetragonal LEED pattern without any sign of fractional spots, see Fig. 4.4a. The sample measured at lower temperature shows a better LEED pattern with clearer fractional spots (see Fig. 4.4b & 4.4c). This is expected from a surface with low Debye temperature. The lower background in Fig. 4.4c indicates a better ordering of the surface.

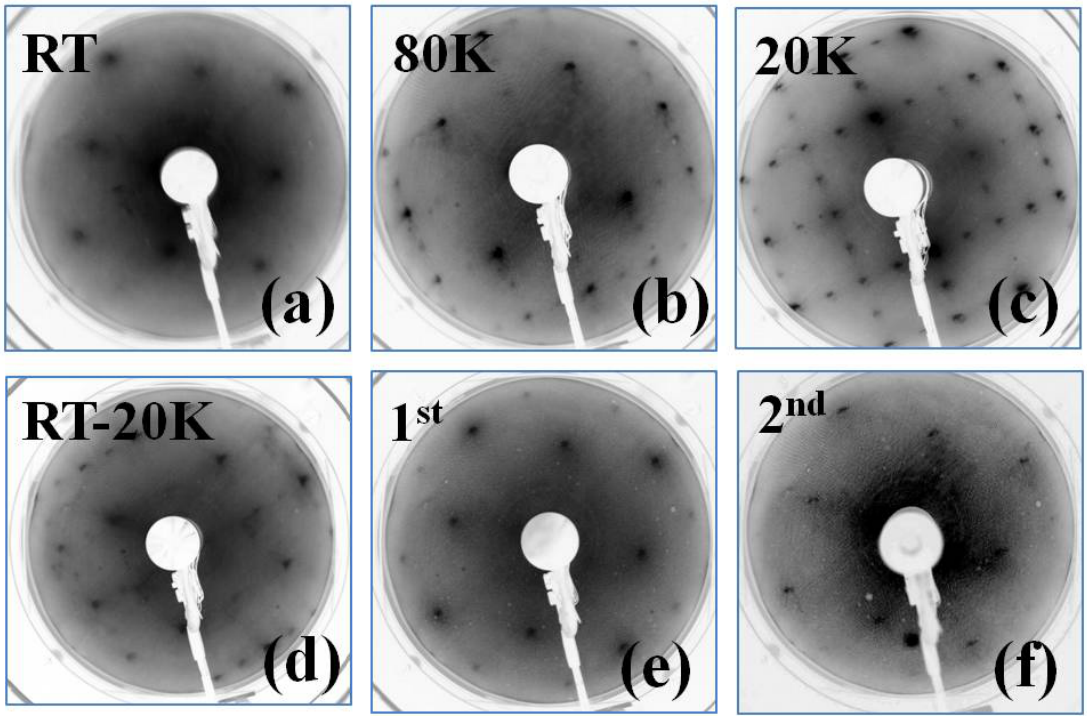

FIGURE 4.4. LEED pattern of parent Ca122 sample cleaved and measured under different conditions at: (a) room temperature (RT); (b) liquid nitrogen temperature 80 K; (c) liquid helium temperature 10 K; LEED pattern of sample cleaved at RT, measured at liquid helium temperature 10K after: (d) cooled down to 10K from RT (RT-LHe); (e) 1st thermal cycle (RT-LHe-RT-LHe); (f) 2nd thermal cycle (RT-LHe-RT-LHe-RT-LHe).

Thermal cycling can also destroy the (1×2) phase. There are still weak fractional spots at 20 K after the cleavage at room temperature and cooling down (Fig. 4.4d). However, LEED patterns after one and two thermal cycles show no fractional spots (Fig. 4.4e & 4.4f, respectively). Thermal cycling kills fractional spots and increases the background. We infer that the (1×2) order phase becomes disordered or destroyed and only the integer tetragonal spots from the underneath bulk lattice remain similar.

The (1×2) phase is sensitive to the electron beam energy. The fractional spots gradually fade away (within 60 minitues), and disappear when the sample exposed to electron beam with energy from 40 eV to 400 eV. Sample contamination may be one of the reasons that the spots disappear because the vacuum pressure went up to 3×10^{-9} *Torr* when the LEED filament and beam voltage was on. However, after the fractional spots disappeared on the first sample, we observed that the second sample on the same plate cleaved simultaneously with the first sample still showed fractional spots when we moved the LEED beam from first sample to the second sample. If contamination was the main reason, the fractional spots would have disappeared at the same time in both samples. Thus, it is likely that the electron beam can disturb the (1×2) phase.

Our observation is similar to what was observed in Co-doped Ba122 compounds [89]. Extra care has been given to record the best LEED I-V data in a time period as short as possible. We used only the best LEED pattern recorded within an hour after the cleavage for LEED I-V structural refinement.

In the analysis of surface structure, we assume that the termination layer cannot be Fe, because of strong bonding between As and Fe. Figure 4.5 shows six structural models of Ca/As-termination, a dimerized full monolayer of Ca/As at the first column, a buckled full monolayer of Ca/As at the middle column (filled and empty

circles) and, a half-monolayer of missing Ca/As at the third column. All of these six models have the same (1×2) unit cell, as shown by LEED and STM.

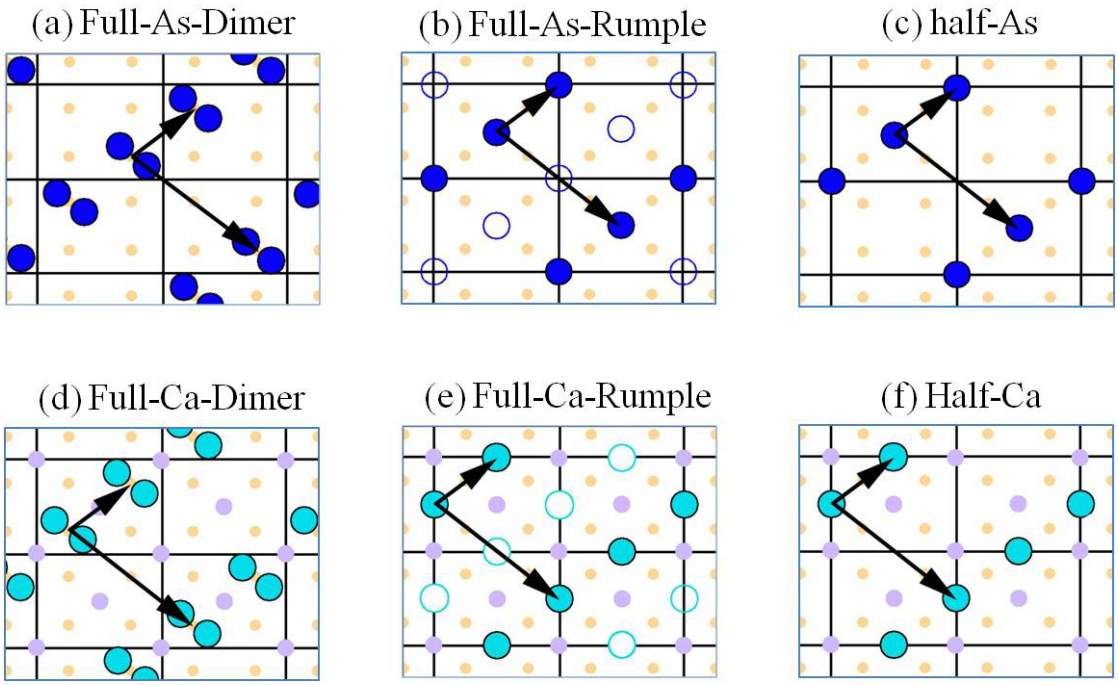

FIGURE 4.5. Six possible structural models for stripe (1×2) phase for (1 strow a, b, c)Ca- and (2^{nd} row d, e, f)As- termination. The first column (a, d) is the dimer model; the second column (b, e) is the buckling model; and the third column (c, f) is the half atoms missing model.

The intensity of fractional spots in LEED patterns (see Fig. 4.3b) is solely contributed by the (1×2) superlattice but the integer spots contain mixed intensity from (1×2) stripe phase and other phases (for example, a non-reconstructed As-planes with randomly distributed Ca atoms, see Appendix C.) Therefore, only the fractional spots are used in the LEED I-V structural refinement. Equivalent beams are averaged, smoothed, and then normalized to the electron gun current. For Ca122, 9 fractional beams (0.5, 0), (0.5, 1), (1.5, 0), (1.5, 1), (0.5, 2), (1.5, 2), (2.5, 0), (2.5, 1), (0.5, 3) were collected with total energy range 1224 eV.

For LEED structural input files for Ca122, we used (1×2) tetragonal cell with $a = b = 5.506$ $\mathring{A}$ and $c = 11.664$ $\mathring{A}$ from crystallographic data at 20 K from

reference [99]. In-plane atom displacements were searched in typical step size 0.02 $\mathring{A}$ while out-of-plane 0.01 $\mathring{A}$. In these six models in Fig. 4.5, the estimated maximum in-plane error $\pm$ 0.02 $\mathring{A}$ is very small thus makes no difference for LEED I-V calculation for using a tetragonal lattice instead of orthorhombic lattice. We optimized the R_p factor with a grid of surface Debye temperature of As/Fe layer and Ca/As layer in these two termination respectively. Then we finalize our structure by optimizing two Debye temperatures.

The R_p values achieved with optimized structure and Debye temperature for the six different models of the surface of $CaFe_2As_2$ are: 0.80 for a Full-As-dimer, 0.67 for a full-As-rumple, 0.8 for a half-As, 0.8 for full-Ca-dimer, 0.6 for full-Ca-Rumple, and 0.23 for half-Ca model. The half-monolayer-Ca model with Rp of 0.23 is the only acceptable answer. Figure 4.6 shows the fitting of theoretical I-V curves to experimental I-V curves for the best structure. The experimentally determined displacements are in Table 4.1. The corresponding bond length and intra-layer spacing are shown in Table 4.4. The resulting structure is drawn in top view in Fig. 4.7a and 3D view in Fig. 4.7b. For comparison, Table 4.1 also include our LEED I-V structure results on 7.5%-Co-doped Ca122 and Table 4.2 shows the structure details of stripe phase in Ba122. They all display the similar behavior.

The termination with half-monolayer Ca is not surprising, because it is the most intuitive model and has the lowest energy according to DFT calculations [121]. However, the details of the surface reconstruction of Ca122 are surprising and not anticipated. In Fig. 4.7b, we show three vertical planes labelled with *a*, *b*, and *c*. The Fe and As atoms are labelled according to their respective plane, Fe3 and As3 in plane *a*, Fe2 and As2 in plane *b*, and Fe1 and As1 in plane *c*. Our structural refinement indicates that Ca atoms at the surface are pulled down by as much as 0.5 $\mathring{A}$, as shown in Fig. 4.7b. What is even more startling is the distortion in the

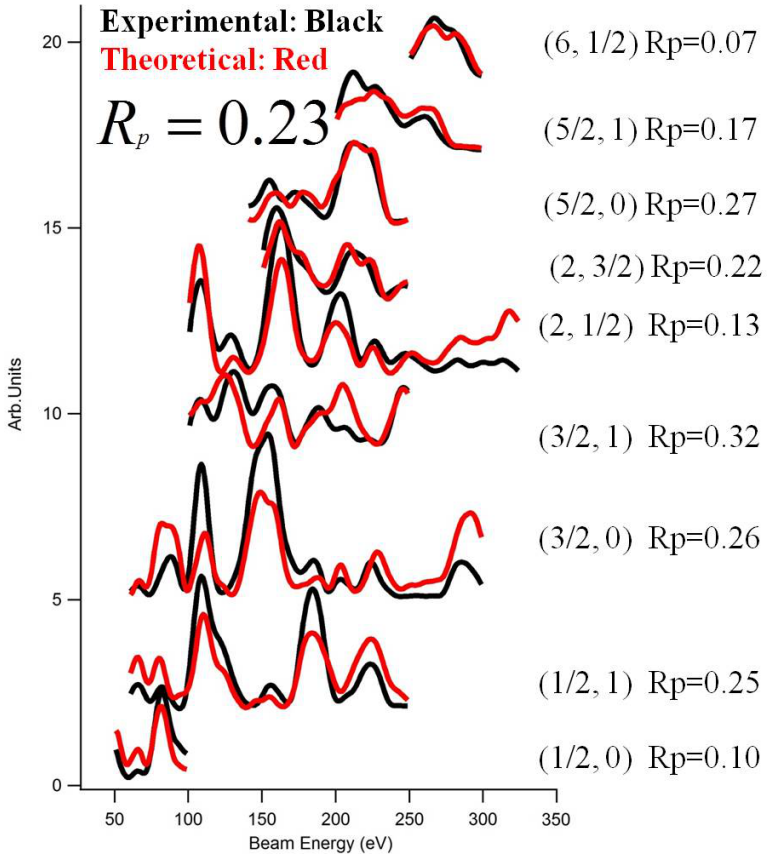

FIGURE 4.6. LEED I-V analysis on (1×2) fractional spots at the surface of $CaFe_2As_2$.

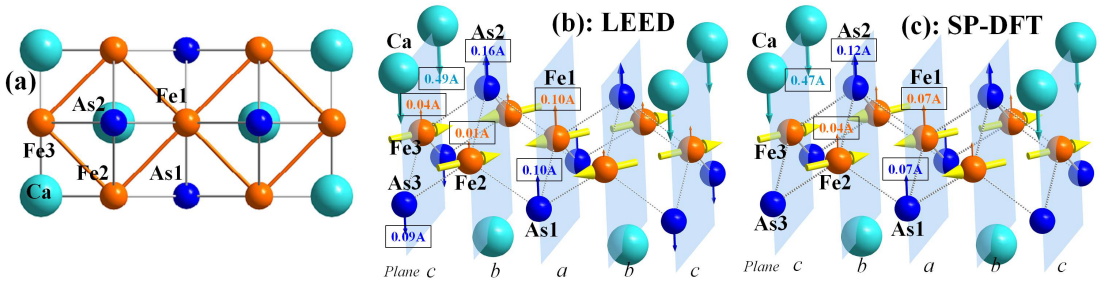

FIGURE 4.7. (a) Top view of (1×2) unit cell and surface structure for (1×2) stripe phase in $CaFe_2As_2$ determined by LEED I-V analysis (b) and DFT calcuation (c).

As-Fe_2-As triple layer just below the surface Ca plane: the Fe atoms (Fe1) between the Ca rows move up by 0.1 $\mathring{A}$, compared to the position of this plane for a bulk structure or the position of the Fe3 atoms. The displacements of other surface Fe atoms (Fe2 & Fe3) are less than 0.05 $\mathring{A}$ which is comparable to error bar (see Table 4.1). The R_p is very sensitive to the vertical motion of Ca and Fe1 atoms so their error bars are small. The rippling in the Fe plane seems to be accompanied by similar distortion in the As planes, but the error bars are too large to justify this conclusion (see Table 4.1).

TABLE 4.1. Stripe (1×2) Surface Structure for $CaFe_2As_2$ and $Ca(Fe_{0.925}Co_{0.075})_2As_2$

Labels	Bulk[109]	Bulk(the.)	Ca122-Surf.(exp.)	Co-Ca122-Surf.(exp.)	Surf.(the.)
Ca	0.0000	0.000	+0.49(±0.04)	+0.54(±0.03)	+0.474
As2	1.5583	1.538	-0.16(±0.26)	-0.04(±0.23)	-0.118
Fe1	2.9160	2.851	-0.10(±0.05)	-0.07(±0.04)	-0.073
Fe2	2.9160	2.851	-0.01(±0.10)	+0.08(±0.13)	-0.043
Fe3	2.9160	2.851	+0.04(±0.06)	+0.11(±0.05)	+0.004
As1	4.2737	4.160	-0.11(±0.10)	-0.04(±0.06)	-0.072
As3	4.2737	4.160	+0.10(±0.10)	+0.11(±0.05)	-0.008
Ca	5.8320	5.698	0.000	0.000	0.000

Figure 4.8 shows the error bar analysis on the optimized structure parameters. Using Eq. 2.39 with $V_{oi} = 5.0\ V$, we have $\Delta R = 0.04$. Thus the cutoff maximum R_p is 0.27 (= 0.23 + 0.04). From Fig. 4.8a, the error bar on the top Ca layer is 0.035 $\mathring{A}$ which is very small, indicating that the large relaxation is indeed accurate. The error bar on the center Fe1 atom is also less than 0.045 $\mathring{A}$. What is interesting is the error bar on the As2 atoms is as huge as 0.26 $\mathring{A}$. The main reason is that the As2 atoms forms a sub-lattice which is a tetragonal lattice, thus they only contribute to spots with at least one integer index. To reduce the error bar on As2 atoms, one need to include integer spots for LEED I-V analysis. However, in Ca122 case, as demonstrated in LEED images in Fig. 4.4, the integer spots not only have signals from the underneath As-tetragonal lattice but also (1×2) stripe phase.

When (1×2) phase is destroyed or disordered, the LEED I-V analysis on integer spots shows a bulk-truncated As surface without any measurable relaxation. This will be explained in Appendix C for the surface structure from tetragonal integer spots. Nevertheless, we believe that the 0.16 $\mathring{A}$ upward motion of As2 atoms needs to be carefully treated because of the large error bar.

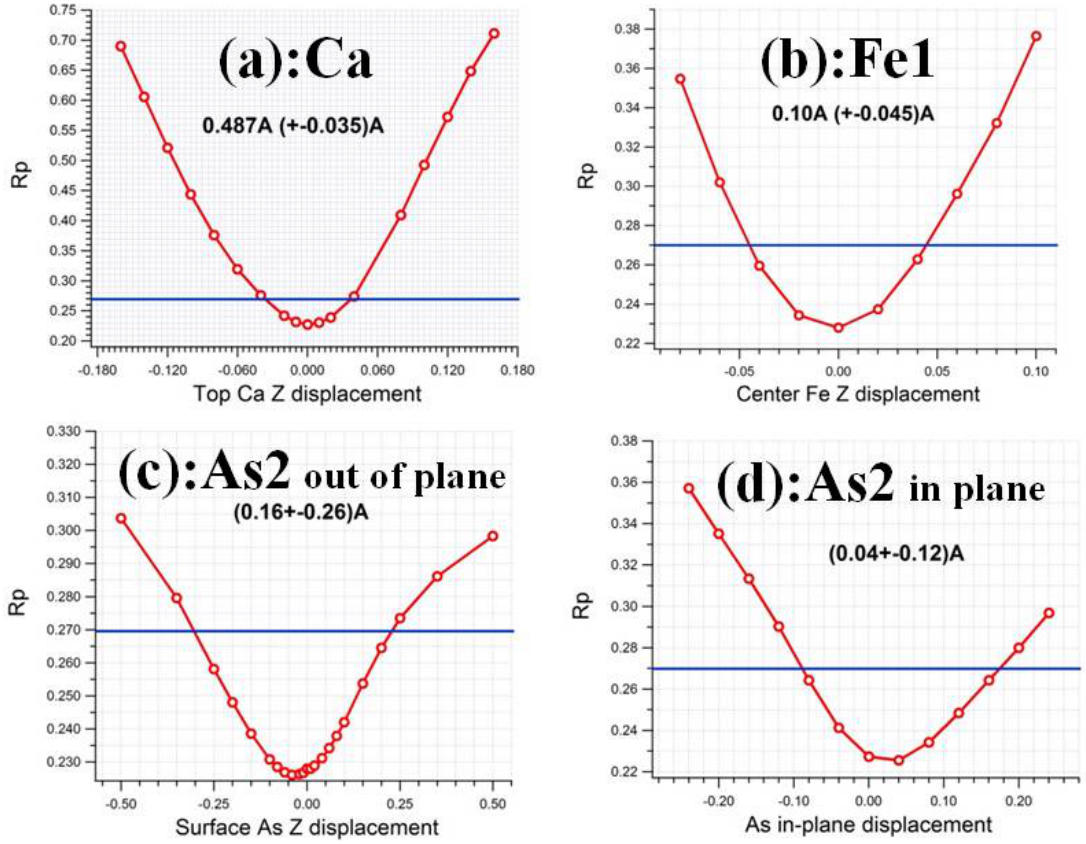

FIGURE 4.8. Structural error bar analysis on the optimized structure parameters on (1×2) stripe surface. R_p vs. displacement curve for (a) for top Ca layer out-of-plane (b) for the center Fe1 out-of-plane (c) for As2 atoms out-of-plane and (d) for As2 in plane.

The error bar for in-plane displacements of As2 atoms is also analyzed. The motivation is from the observation of a dimerization in some STM images on the stripe phase in Fig. 4.9a & 4.9b. Stripe phases in Sr122 [114] and Ba122 [108] were resolved to be dimmer-like. It is argued that they are due to the As-dimerization thus the termination layer is a full monolayer of As surface instead of half Ba/Sr/Ca

surface [108]. Our structural analysis gives 0.04 $\mathring{A}$ in-plane movements of As2 dimerization, however, there is a 0.12 $\mathring{A}$ error bar. Thus, LEED I-V analysis only indicates a possibility of dimerization on the As2 atoms but can not serve as a direct proof. The consistency of STM images of Fig. 4.9a & 4.9b with half-Ba/Sr/Ca termination model is explained by theoretical simulated STM images in Fig. 4.9c & 4.9d. Note that the bright spots do not directly correspond to the positions of surface atoms. Similar STM images are obtained for the (1×2) (Ba,Sr)-terminated (Ba, Sr)Fe_2As_2 surface. We believed that this is the reason for a dimerized topography occasionally seen by STM.

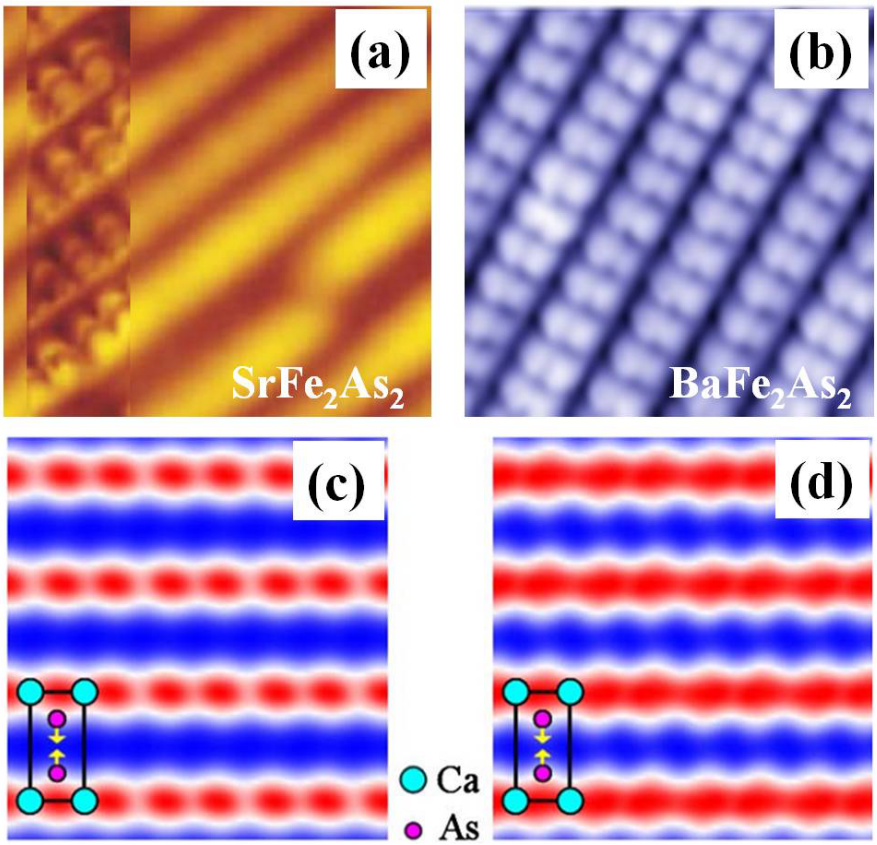

FIGURE 4.9. Possible dimerziation at the As layer. (a) STM images for the stripe (1×2) surface of $SrFe_2As_2$, figure adapted from reference [114]. (b) STM images for the stripe (1x2) surface of $BaFe_2As_2$, figure is adapted from reference [108]. (c-d) Simulated STM images of the (1×2) Ca-terminated $CaFe_2As_2$ surface in the Ort-AFM with bias voltages of (c) 100 and (d) - 100 meV. The rectangles indicate (1×2) surface unit cells, figures are adapted from reference [121].

Last we discuss some of our results on the stripe phase in Ba122. Fig.4.10 is the similar surface studies of the stripe phase in Ba122. Figure 4.10a & 4.10b show two types of stripe domains-twin domains and anti-phase domains. Figure 4.10c is the fitting of theoretical I-V curve to experimental I-V curve. With a reasonable good $R_p \sim 0.24$, we identify the surface as half-Ba terminated surface with 0.45 $\AA$ inward motion. The surface structure is very similar to Ca122 case and details can be found in Table 4.2 and4.4.

TABLE 4.2. Stripe (1×2) Surface Structure for $BaFe_2As_2$.

Labels	Bulk[109]	Bulk(the.)	Ba122-Surf.(exp.)	Surf.(the.)
Ba	0.0000	0.000	+0.45(±0.03)	+0.410
As2	1.8926	1.929	-0.10(±0.10)	-0.070
Fe1	3.2363	3.222	-0.04(±0.02)	-0.037
Fe2	3.2363	3.222	-0.03(±0.03)	-0.038
Fe3	3.2363	3.222	-0.01 (±0.03)	-0.033
As1	4.5800	4.512	-0.06(±0.04)	-0.050
As3	4.5800	4.512	+0.02(±0.03)	-0.028
Ba	6.4727	6.438	+0.000	+0.000

Figure 4.11 shows a defect line and also an anti-phase domain wall parallel to the stripes, in contrast to the anti-pahse domain wall perpendicular to stripes in Fig. 4.10b. We took STS along the wall and perpendicular to the wall. The STS on the defect line or domain wall (curve 1) has lower local density of states at filled states. However, close examination in the inset of Fig. 4.11b shows that near the Fermi surface, the defect line or anti-phase domain wall actually has a higher local density of states. The wall affects the local density of states by at least two nearby stripes (curve 2 & 3) but the STS resumes back to the one at clean stripe surface starting from location 4 see Fig. 4.11b. Further analysis is needed to understand how the domain walls at stripe surface change the local electronic properties, thus offering insights on the general electronic properties of stripe surface.

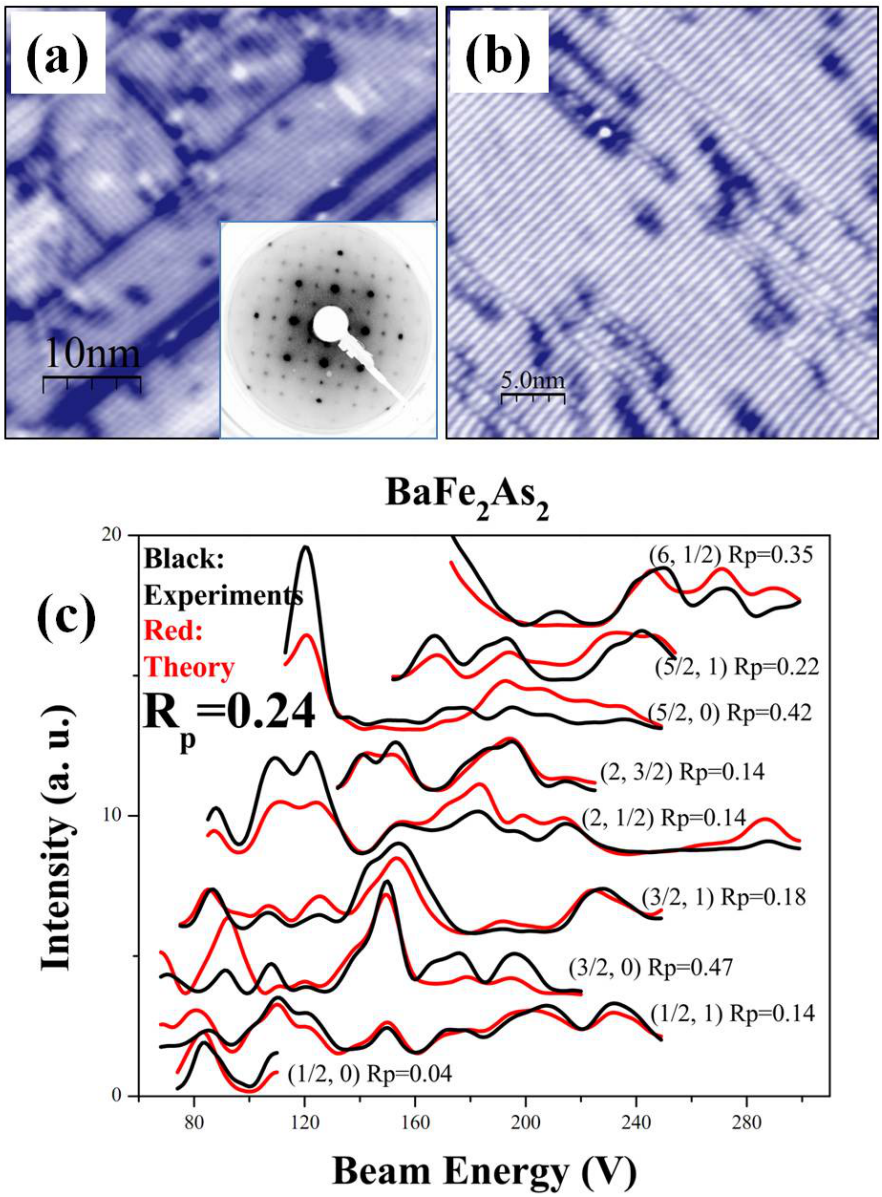

FIGURE 4.10. Surface structure studies on $BaFe_2As_2$ stripe phase. (a) STM topography (1V, 0.2nA) with perpendicular twin domains. Inset is the LEED pattern. Note that compared to Ca122, there are additional fractional spots which correspond to $(\sqrt{2}\times\sqrt{2})$R45° order and will be explained in the next chapter. (b) STM topography (1V, 0.2nA) with anti-phase domains. (c) Fitting theoretical I-V curves to experimental I-V curves in LEED I-V analysis. The overall R_p is 0.24.

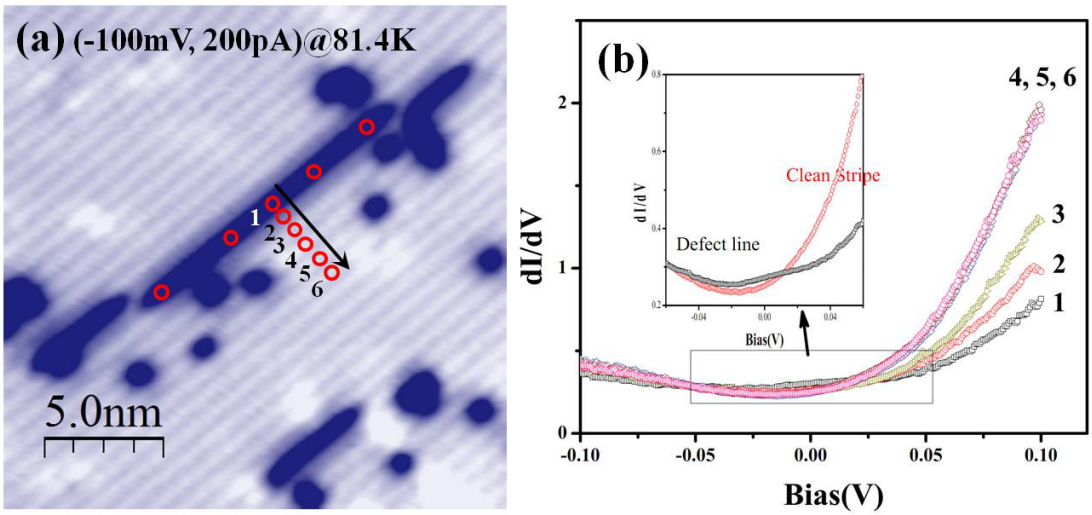

FIGURE 4.11. STS from stripe surface of $BaFe_2As_2$. (a) STM topography of an anti-phase domain wall parallel to stripes. (b) Comparison of STS taken along the anti-phase domain wall and perpendicular to the wall.

4.2.2 Theory: First-principles calculation

We proved that the (1×2) stripe surface in Ca122 is a half-Ca terminated surface with structure details shown in Fig. 4.7b and Table 4.1. To examine the origin of this reconstruction, we performed spin-dependent DFT calculations. Plane-wave DFT calculations were performed using the VASP package [122, 123], within the generalized gradient approximation (GGA) using the Perdew-Burke-Enzerhof (PBE) exchange-correlation function [124]. Projector augmented wave (PAW) pseudopotentials [125] were used with energy cutoff of 400 eV. The Brillion zone was sampled in the k space within Monkhorst-Pack scheme [126] with the number of these k points being (16 × 16 × 8) for bulk compounds and (8 × 8 × 1) for the (1×2) surface structures. For bulk structures, both atom positions and cell dimensions were allowed to relax until the residual forces are below 0.02 $eV/\mathring{A}$. Then two optimized bulk unit cells (see Fig. 4.2a) were taken along the z-axis direction to model the surface in the repeated slab model with a vacuum space of 14 $\mathring{A}$. The surface was relaxed with in-plane lattice parameters fixed as the bulk ones

until the residual forces go below 0.04 $eV/\mathring{A}$. For spin-polarized calculations, a certain spin ordering was imposed on a given bulk structure and then the lattice and magnetic moments were optimized.

We first considered a non-magnetic tetragonal model. DFT calculations give the so-called collapsed tetragonal phase with c axis about 1 $\mathring{A}$ shorter than the one in orthorhombic phase. Since DFT is calculating the ground state phase, it fails to reproduce the high temperature tetragonal phase. This is the same situation with the published DFT calculation [128] where theory cannot produce a high temperature tetragonal phase. The surface structure from DFT calculation without any spin ordering has only 0.38 $\mathring{A}$ relaxation at the top Ca layer at the surface, which is almost 0.1 $\mathring{A}$ less than experimental determined value. If we simply scaled the c axis (10.4 $\mathring{A}$) to the one (11.4 $\mathring{A}$) in high temperature tetragonal phase, the relaxation is 0.42 $\mathring{A}$ which is still less than experimental value of 0.49 $\pm$ 0.04 $\mathring{A}$.

We then consider different models for AFM ordering. Six AFM configurations for Ca122, are shown in Fig. 4.12, where AFM1 is actually the bulk AFM ordering. Careful examination shows that AFM1 and AFM3 are equivalent to each other. For AFM1 or bulk AFM ordering, the FM ordering is along b direction and AFM ordering is along a direction. For AFM3, the FM ordering is along a direction and AFM is along b direction. The structural optimization shows that a in AFM1 has the value of b in AFM3 and b in AFM1 is equal to a in AFM3. Similarly, AFM4 is equivalent to AFM6. Hence, AFM3 and AFM6 will not be discussed anymore. The simulation results for spin orderings are summarized in Table 4.3.

For the Ca122 bulk, calculations show that AFM2 and AFM5 are not stable. The structural relaxations with initial AFM2 or AFM5 configuration reach equilibrium with final magnetic moments of Fe atoms of zero. This is true for FM ordering. Only AFM1 and AFM4 orderings are seen by theoretical calculations

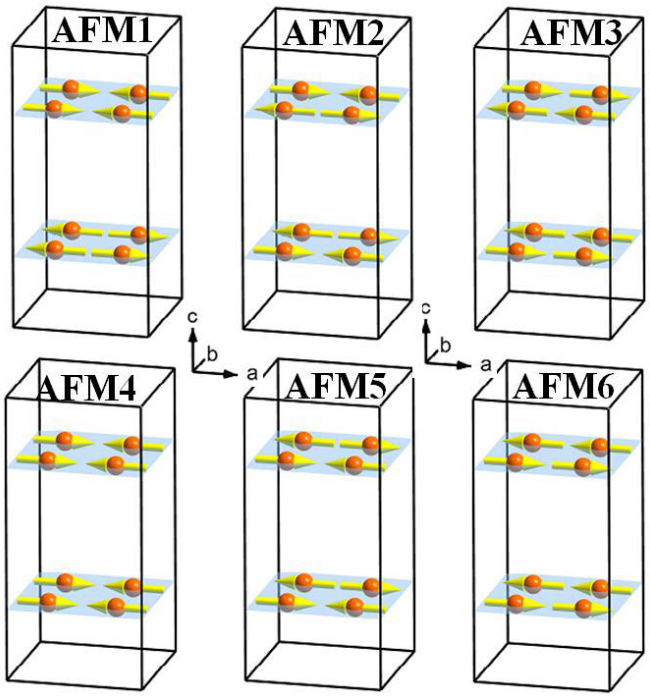

FIGURE 4.12. Six AFM configurations. AFM1: magnetic moments on Fe atoms are AFM coupled along a and c axis, but FM coupled in b axis; AFM2: magnetic moments are AFM coupled along all three axis; AFM3: magnetic moments are AFM coupled in b and c axis but FM coupled in a axis; AFM4: magnetic moments are only AFM coupled in a axis but FM coupled in both b and c axis; AFM5: magnetic moments are AFM coupled in both a and b axis but FM coupled along c axis; AFM6: magnetic moments are only AFM coupled in b axis but FM coupled in both a and c axis.

TABLE 4.3. Surface energies of different AFM ordering by DFT calculation.

AFM structure	a Å	b Å	c Å	Energy meV/unit	magnetic moment(μ_B)
$CaFe_2As_2$					
AFM1	5.60	5.49	11.38	0	1.78
AFM4	5.59	5.51	11.31	162	1.64
NM	5.63	5.63	10.41	3560	0.00
$BaFe_2As_2$					
AFM1	5.71	5.61	12.88	0	1.93
AFM2	5.65	5.65	12.74	390	1.49
AFM4	5.69	5.62	12.89	20	1.89
NM	5.61	5.61	12.65	509	0.00

and AFM1 is the most stable structure (see Table 4.3). For the surface, there is little difference between AFM1 and AFM4 because the difference between AFM1 and AFM4 is the coupling along the c axis (AFM vs. FM), which is not important in our surface relaxation. For the Ba122 bulk, the stable phase with neither FM nor AFM5 ordering can be found. (1×2) stripe surfaces with AFM1 (the most stable phase) or AFM4 ordering both show inward motion of the top Ba layer by 0.41 $\mathring{A}$ (again topmost Fe layers share the same AFM1 ordering), while (1×2) surfaces with AFM2 and NM configurations both exhibit contraction of top layer by 0.35 $\mathring{A}$. Thus, the conclusion is similar with Ca122 where AFM1 or bulk AFM ordering is the stable phase with lowest energy.

For $CaFe_2As_2$, the structural relaxation with bulk AFM configuration (see Fig. 4.2a) yields the orthorhombic bulk with lattice parameters as $a = 5.596$ $\mathring{A}$, $b = 5.489$ $\mathring{A}$ and $c = 11.375$ $\mathring{A}$ (Table 4.4). Optimization without spin ordering gives collapsed-tetragonal bulk phase with lattice parameters as $a = b = 3.982$ $\mathring{A}$ and c =10.414 $\mathring{A}$ (Table 4.4). This is consistent with Yildirim's first-principle calculations where the giant reduction in parameter c depends upon the magnetic configuration [128]. Our spin-dependent DFT calculations for the orthorhombic (1×2) stripe ordered surface structure (Fig. 4.7c) show a large contraction of 0.49 $\mathring{A}$ for the topmost Ca layer. The center Fe1 atoms move outward by 0.07 $\mathring{A}$. These results, within the experimental error are identical to what was obtained from the LEED I-V analysis. The surface with AFM4 ordering has a top layer sunk down by 0.45 $\mathring{A}$, but again its energy is higher than the bulk AFM ordering and its in-plane AFM ordering is the same with AFM1. Thus, these results confirm that the topmost Fe layer in the (1×2) orthorhombic Ca122 surface structure has bulk AFM (AFM1) ordering.

Since the spin-polarized DFT calculations reproduce the observed surface structure, it is appropriate to use the theory to understand the interplay between spin,

charge, and lattice associated with the surface relaxation. We use Bader charge analysis to separate charge density to each atom by using zero-flux surface where charge density is a minimal along the direction perpendicular to the surface. This is an intuitive way where the charge enclosed within Bader volume is a good approximation to the total electronic charge of an atom. Table 4.5 shows Bader charge arrangements for surface and bulk in three different structural configurations. The first one is the ground state configuration with an orthorhombic AFM bulk (Ort-AFM); the second is the same structure but with magnetic moment forced to be zero (Ort-NM), and the final configuration is the collapsed tetragonal configuration with no magnetic order (Tet-NM). DFT results on Ba122 are also included in Table 4.5 for comparison.

TABLE 4.4. Comparison of surface and bulk by DFT calculation (units:$\mathring{A}$).

Phase	c	$Z_{Ca/Ba-As}$	Z_{Fe-As}	d_{Fe-As}	$\alpha_{As-Fe-As}$
$CaFe_2As_2$					
Bulk-Ort	11.396	1.538	1.313	2.360	112.4
Sur-Ort		0.946	1.358	2.385	110.6
Diff. sur-bulk		-0.592	0.045	0.025	-1.8
Bulk-CT	10.424	1.437	1.169	2.310	119.2
Surface-CT		0.936	1.269	2.362	115.0
Diff.sur-bulk		-0.501	0.10	0.052	-4.2
$BaFe_2As_2$					
Bulk-Ort	12.884	1.929	1.292	2.381	114.3
Surface-Ort		1.451	1.328	2.401	112.8
Diff.sur-bulk		-0.48	+0.036	0.02	-1.5
Bulk-Tet	12.624	1.954	1.202	2.321	117.6
Surf-Tet		1.525	1.252	2.348	115.6
Diff. sur-bulk		-0.429	0.05	0.027	-2.0

The formal valences in Ca122 are Ca^{+2}, Fe^{+2}, and As^{-3}. Figure 4.13a shows the calculated change of the Bader charge on the surface atoms compared to the bulk in the Ort-AFM phase. The first observation is that the surface becomes more neutral than the bulk. The surface Ca atoms which are pulled down ~ 0.5 $\mathring{A}$ become 8% less positively charged compared to the bulk (+ 1.43 e bulk to

+ 1.31 e surface). Surprisingly, the Fe atoms also become less positive. There is $\sim$ 58% change in the charge of Fe3 atom (+ 0.31 e bulk to + 0.13 e surface) and 35% change in the charge of Fe2 atom (+ 0.31 e bulk to + 0.20 e surface) compared to the bulk. On average, the charge on the Fe atoms in the third layer is $\sim$ 27% less positive than in the bulk. This charge rearrangement is present even in the second and forth As layers, As2 is $\sim$ 13% less negative, while As1 and As3 also have 13% and 15% change, respectively. In short, charge redistribution at the relaxed surface tends to be more neutral than in the bulk. This reflects the impact of surface lattice reconstruction on the charge.

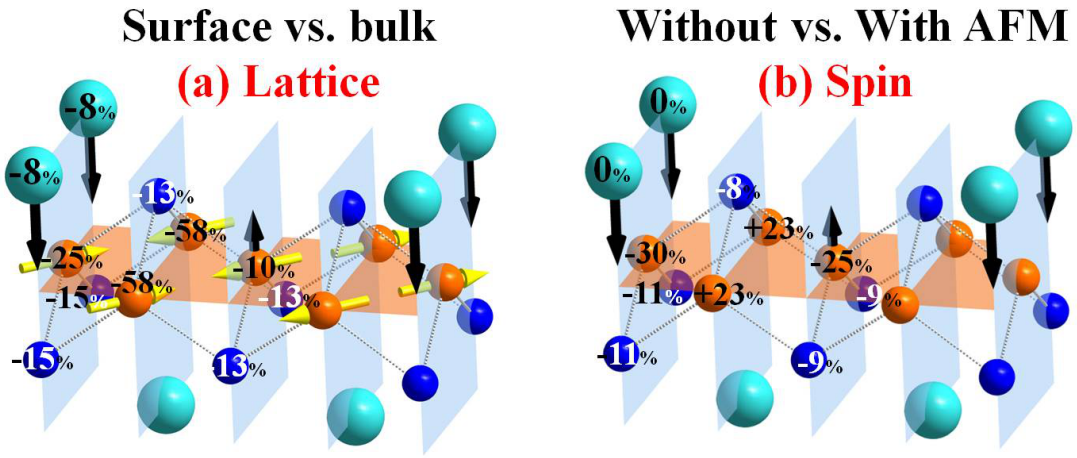

FIGURE 4.13. The impact of (a) lattice reconstruction and (b) AFM ordering on the surface charge. (a): the change on Bader charge by comparing surface to the bulk in ort-AFM phase. (b): the change on Bader charge by removing AFM ordering with ort-AFM lattice fixed. Note that the (a) has the yellow arrows indicating spins and both figures have the same lattice structure with black arrows indicating the surface relaxation on the top Ca-layer and buckling of the center Fe atom.

If the structure (Ort) is fixed and the magnetic moment is set to zero (NM), the impact of spin ordering on the charge can be displayed. Figure 4.13b shows that there is dramatic charge redistribution in the bulk in the Ort-NM phase, comparable with the difference between the surface and bulk in the Ort-AMF phase (Fig. 4.13a). The Fe1, Fe2 and Fe3 atom becomes 25%, 40%, and 30%

less positive, respectively. All the negatively charged As becomes nearly 10% less negative. There is almost no change at the charge on the Ca. This large charge redistribution combined with the loss of spin ordering is what drives the system into the collapsed tetragonal phase.

A 3D view of charge distribution in space is helpful to understand the change on the charge. A charge density map is obtained by subtracting the charge distribution of non-magnetic orthorhombic phase from AFM orthorhombic phase, $\rho(x,y,z)=\rho(x,y,z)_{NM}$-$\rho(x,y,z)_{AFM}$. A plot of isosurface of this charge distribution is shown in Fig. 4.14. It is a surface that represents points of a constant charge density value, here we set the constant as 0.0009 $e/\mathring{A}^3$. The yellow color represents less positive while the green color less negative. By removing AFM ordering, both at the surface and the bulk, the charge on Ca does not change; Fe atoms become less positive thus surrounded by the green color; As atoms become less negative thus surrounded by the yellow color. Further, if we compare the surface to the bulk in this isosurface plot, we realize that surface is slightly different than bulk, evidenced by a larger area of the green and yellow color. It indicates that comparing to the bulk, the surface actually responses stronger to the removal of spin ordering due to the broken surface symmetry.

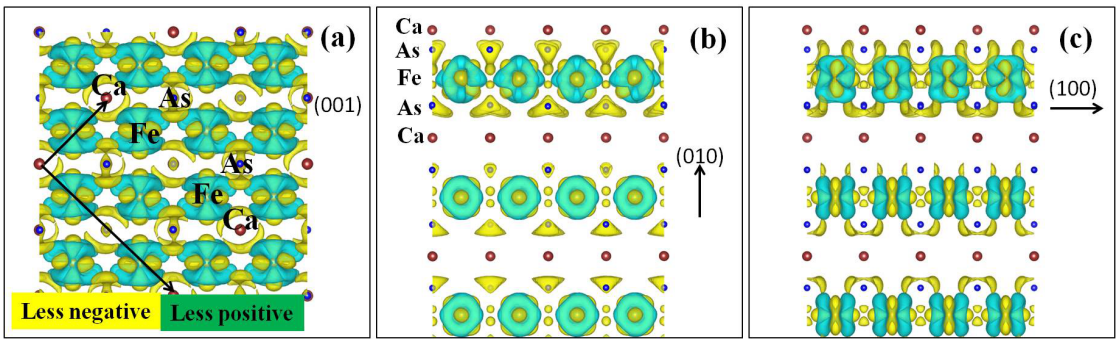

FIGURE 4.14. Isosurface plots of the difference of charge distribution by the removal of the spin ordering with its orthorhombic structure fixed. (a) (001) view of the isosurface. The (1×2) unit cell is indicated by the black arrows and the positions of Ca, Fe and As atoms are marked. (b) (010) view of the isosurface. (c) (100) view of the isosurface.

Obviously, the charge mediates the coupling between the spin and lattice. In an attempt to understand the process of the surface reconstruction, it will be interesting that we do a self-consistent structural calculations starting with the Ort-AFM configuration but gradually reducing the magnetic moment. Yildirim [127] has done such spin-fixed calculations and point out that the magnetic moment of Fe is the key parameter controlling the coupling while the spin structure is the secondary effect. We note that our DFT calculations show a slight larger magnetic moment (3%) at the $CaFe_2As_2$ surface indicating a possible enhanced spin-lattice coupling at the surface.

TABLE 4.5. Bader charge distribution by DFT calculation (units:e).

Phase	Ca/Ba	As2	Fe1	Fe2	Fe3	As1	As3
$CaFe_2As_2$							
Bulk-Ort-AFM	+1.43	-0.99	+0.31	+0.31	+0.31	-1.06	-1.05
Sur-Ort-AFM	+1.31	-0.86	+0.28	+0.2	+0.13	-0.92	-0.89
Diff. sur-bulk	-0.12	+0.13	-0.03	-0.11	-0.18	+0.14	+0.16
Bulk-Ort-NM	+1.39	-0.79	+0.14	+0.14	+0.14	-0.88	-0.88
Sur-Ort-NM	+1.31	-0.79	+0.21	+0.12	+0.16	-0.84	-0.79
Diff. sur-bulk	-0.08	0.0	+0.07	-0.02	+0.02	+0.04	+0.09
Bulk-CT	+1.36	-0.78	+0.05	+0.05	+0.05	-0.78	-0.78
Surface-CT	+1.29	-0.76	+0.17	+0.08	0.00	-0.75	-0.78
Diff.sur-bulk	-0.07	0.02	+0.12	+0.03	-0.05	+0.03	+0.02
$BaFe_2As_2$							
Bulk-Ort-AFM	+1.26	-0.88	+0.26	+0.26	+0.26	-0.90	-0.88
Surface-Ort-AFM	+1.12	-0.82	+0.30	+0.26	+0.24	-0.92	-0.89
Diff.sur-bulk	-0.14	+0.06	+0.04	0.00	-0.02	-0.02	-0.01
Bulk-Ort-NM	+1.26	-0.81	+0.19	+0.19	+0.19	-0.84	-0.81
Sur-Ort-NM	+1.12	-0.74	+0.22	+0.18	+0.16	-0.83	-0.82
Diff. sur-bulk	-0.14	+0.07	+0.03	-0.01	-0.03	+0.01	-0.01
Bulk-Tet	+1.24	-0.79	+0.16	+0.16	+0.16	-0.79	-0.79
Surf-Tet	+1.11	-0.72	+0.20	+0.17	+0.12	-0.78	-0.78
Diff. sur-bulk	-0.13	+0.07	+0.04	+0.01	-0.04	0.01	0.01

4.3 Spatial Coexistence of superconductivity and AFM

It might be expected that the large distortion in the As-Fe_2-As plane at the surface would kill superconductivity. The reconstruction on Sr_2RuO_4 did [32, 34]. As the temperature drops, the first issue is whether the AFM ordering is lost as the system goes below Tc $\sim$ 19 K. In an alternative way, the question is what the bulk structure is at superconducting region and whether there is a structural transition associated to superconductivity. Bulk measurements by neutron scattering show no indication of a change in the orthorhombicity and the magnetic moment when crossing T_c [129]. Thus the bulk keeps the same orthorhombic structure in the superconducting dome.

STM topographies with the same tip and same junction show no change of the atomic corrugation and surface adatom (bright protrusion in Fig. 4.15a) height above and below T_c, i. e. no significant change on the charge. The atomic corrugation is about 5 pm and the adatom height is about 2 $\AA$. They don't change when crossing superconducting transition temperature. This strongly suggests that there is no structure change or loss of spin ordering at the stripe surface when crossing superconducting transition temperature.

We measured a clear superconducting gap from such surface. Figure 4.16a shows the STM topography below T_c and the black square region where the scanning tunneling spectroscopy (STS) was taken. The averaged STS at 19 K is featureless but shows a clear double-peak feature at 7.5 K in Fig. 4.16b. The double-peaks are believed to be the coherence peaks since they are at symmetric positions above and below Fermi energy in Fig. 4.16c and they disappear when warm up. Gap Δ estimated from the coherence peaks is $\sim$ 7.5 meV thus $2\Delta/(k_B T_c) = 8.8$, which is in the upper range of reported reduced gap values in Fe-based superconductors

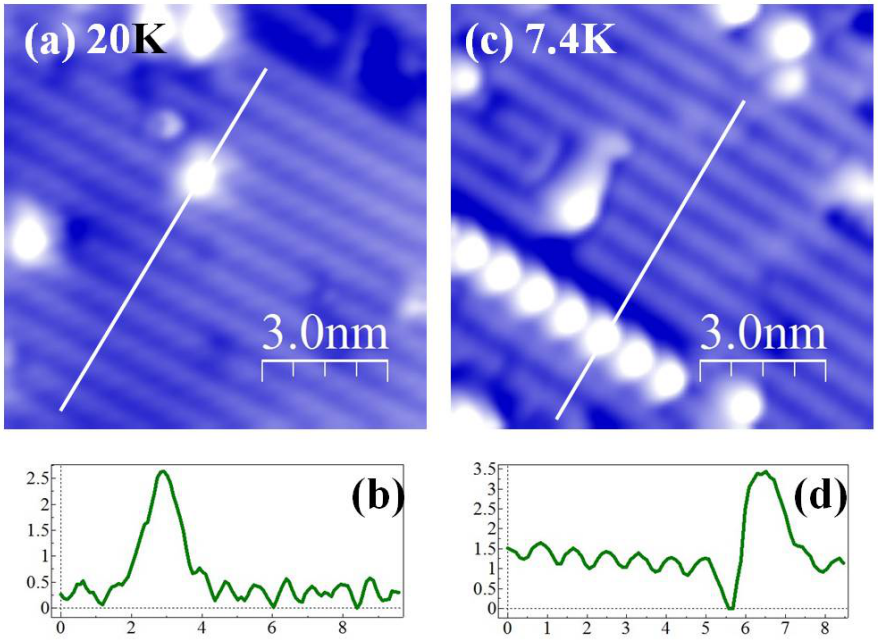

FIGURE 4.15. STM topographies above and below T_c. (a) STM topography (1 V, 0.2 nA) at 20 K and the profile on the white line is shown in (b). (c) STM topography at (1 V, 0.2 nA) at 7.4 K and the profile on the white line is shown in (d).

and comparable to the one in cuprate [118, 29]. This indicates an unconventional superconductivity at the stripe surface, coexisting with the AFM ordering.

The measured gap in Fig. 4.16c has a large zero bias conductance, nearly half of the coherence peak height, indicating another possible phase competing for the density of states. The promising candidate is the spin density wave gap as reported in $NaFe_{1-x}Co_xAs$ [112], except there is no coherence peaks associated to such spin density wave (SDW) gap in our STS. It is not clear whether the SDW gap is fully gapped or partially gapped with finite density of states at zero bias. Doping Ca with Pr or La can also makes the Ca122 compounds superconducting. The bulk of $Ca_{0.83}La_{0.17}Fe_2As_2$ has a T_c of 42 K and a gap-like density of states depression of 7.7 ± 2.9 meV is measured by STM [130]. However, no superconducting gap was observed on another doped compound $Ca_{1-x}Pt_xFe_2As_2$ [118]. All of the reported spectra at the stripe surface of doped Ca122 compounds, either have suppression

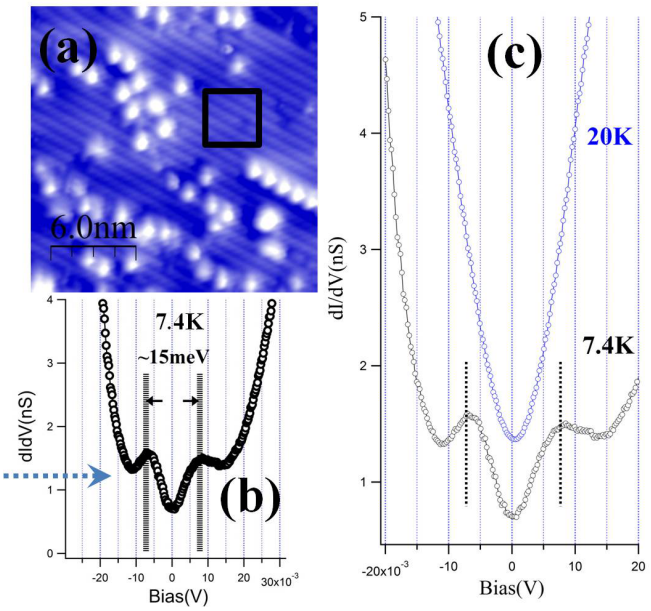

FIGURE 4.16. (a) STM topography on $Ca(Fe_{0.925}Co_{0.075})_2As_2$. (b) Averaged spectroscopy taken from the black square field of view at above and below T_c. (c) Enlarged spectroscopy below T_c taken at 7.4 K with $2\Delta = \sim 15$ meV. The black dash lines lie on the coherence peaks.

of density of states near Fermi surface, or high zero bias conductance, or no clear coherence peaks, leading to a general conclusion that the superconducting in doped Ca122 compounds is modified by other competing phase, which is very likely the AFM phase.

Last, superconducting gap was also found in the Co-doped Ba122 surface [110]. An comparison of superconducting gap at (1×2) stripe phase to $(\sqrt{2}\times\sqrt{2})$R45° phase at Co-doped Ba122 also clearly indicates that the gap feature is more evident in $(\sqrt{2}\times\sqrt{2})$R45° phase, with higher coherence peaks and smaller zero bias conductance [110]. This indicates the coexistence of SC and AFM at (1×2) stripe phase and $(\sqrt{2}\times\sqrt{2})$R45° phase might be different due to the different surface structure. Further STM/S studies in Ba122 are needed in order to clarify their nature of the coexistence.

The microscopically AFM and SC coexistence is consistent with s_{+-} sign changing pairing symmetry [131] and they are competing in underdoped region. A su-

perconducting gap is seen everywhere at the stripe surface indicating that, the co-existence is long-range, in contrast to $BaFe_{2-x}Ni_xAs_2$ where it is short range AFM order coexisting with superconductivity [132]. There is no indication of reduced magnetic moment at the stripe surface suggesting that the large surface relaxation of half-Ca layer may stabilize the surface AFM ordering, thus competing with superconductivity with a possible lower surface superconducting transition temperature. Thus, stripe surface of Co-doped $CaFe_2As_2$ could serves as a playground for the coexistence and competing AFM and SC phases. Further STM studies are needed for a wide range of doping.

In summary, we carried out LEED I-V analysis to identify the stripe-ordered phase seen in the surface of parent and Co-doped $CaFe_2As_2$. The results indicate that the surface consists of half-Ca layer and is reconstructed with (1×2) order. These surface Ca atoms move inward by as large as 0.5 $\mathring{A}$ and the surface As-Fe_2-As layer is buckled. We argue that such motion results from the coupling between spin and lattice through the charge channel. Further, superconductivity is found at the stripe surface indicating a long-range microscopically coexistence of superconductivity and AFM. We have seen the similar results at the stripe surface of Ba122 and thus the coexistence of superconductivity and AFM in Ba122 and Ca122 may have the same origin.

Chapter 5

$(\sqrt{2}\times\sqrt{2})$R45^o domain surface of $BaFe_2As_2$

5.1 Introduction

Co-doped Ba122 system [22] has a qualitatively similar phase diagram with Co-doped Ca122 compounds [99], see Fig. 1.12. Structural and magnetic transitions are coupled and both are suppressed while increasing the doping of Co atoms. However, differences between the two systems are also apparent. Ba has a larger ionic size than Ca. The structural/magnetic transition in Ba122 compound has lower transition temperature and they are gradually suppressed, in contrast to their sharp disappearance in Ca122 compounds. The structural transition in Ba122 is also argued to be second order [26, 167], while it is strongly first order for Ca122 [85]. While the lattice of Ca122 compounds is extremely sensitive to the uniaxial pressure [7], the Ba122 shows a larger in-plane anisotropy which exists at both above and below structural transition temperature [133, 134]. Since structural and magnetic transitions are intimately related to the strong coupling between spin, lattice and charge in the bulk, there is a strong motivation to see how they behave at the surface of Ba122 compare to Ca122. Besides, surfaces are a window to the bulk. Many surface techniques have proven successful in studying complex materials (see Chapter 1) but one needs to understand what the surface does. For example, compared to Ca122, the surface of Ba122 compounds shows a new competing phase to the previous discussed (1×2) stripe phase. That is the $(\sqrt{2}\times\sqrt{2})$R45° phase, which is the focus of this chapter.

Figure 5.1a shows the bulk orthorhombic unit cell representation of layered structure of $BaFe_2As_2$ with the spin ordering. It is exactly the same with the bulk struc-

ture introduced in Ca122 except slightly different lattice parameters and magnetic coupling constants. This orthorhombic (1×1) unit cell at the surface is actually $(\sqrt{2}\times\sqrt{2})$R45° in tetragonal notation. We will use tetragonal terminology except when we explicitly to use orthorhombic. The As-Fe_2-As triple layer structure is sandwiched by Ba layers. The spin structure is so-called collinear structure with AFM coupled in a and c direction but FM coupled in b direction (note that a is the longer axis and b is the short axis). A122 materials with this layered structure are expected to cleave with FeAs layers intact with A ions end on either side of the two cleaved FeAs surface. Cleaving cannot happen at Fe layer because of the strong bonding between As-Fe-As triple layer. Top-views in Fig. 5.1b&c show a full-monolayer of As and Ba layer, respectively. Except the color difference, the two top-views are identical. In one orthorhombic unit cell or $(\sqrt{2}\times\sqrt{2})$R45° unit cell (tetragonal notation), there are two atoms. Later we will show that in $(\sqrt{2}\times\sqrt{2})$R45° phase, we only see one atom in this unit cell.

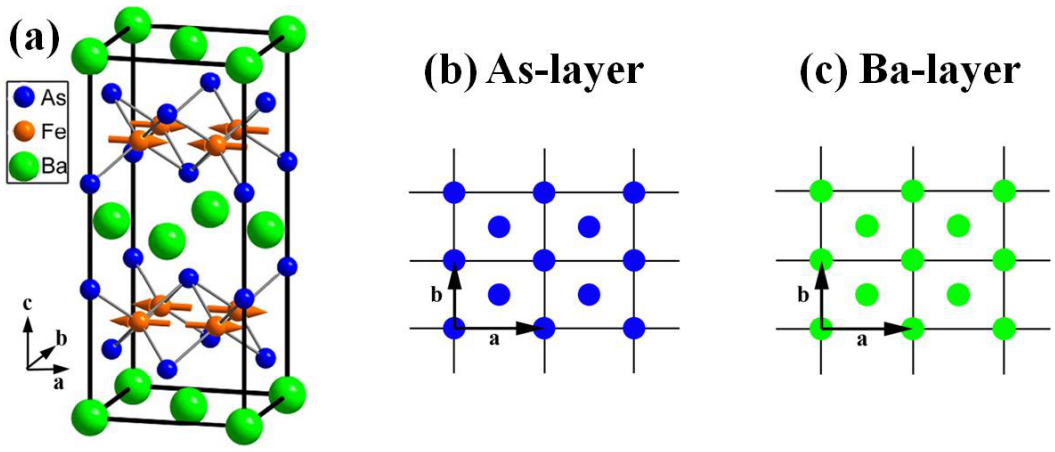

FIGURE 5.1. Bulk geometric and magnetic structure for $BaFe_2As_2$ at low temperature orthorhombic phase (Ort-AFM) in (a) and the top views from As in (b) and Ba layer in (c).

($\sqrt{2}\times\sqrt{2}$)R45° phase is rarely found in Ca122 but it is commonly see in Ba122. The energy of ($\sqrt{2}\times\sqrt{2}$)R45° phase at surface was theoretically found to be close to (1×2) phase in Ba122 compounds [121]. Both phases have the same enhanced surface orthorhombicity which is intimated tied to AFM ordering [108]. Orthorhombicity is defined as $\delta=\frac{a-b}{a+b}$. Figure 5.2 shows that the surface orthorhombicty is larger than 2.4% for both ($\sqrt{2}\times\sqrt{2}$)R45° and (1×2) phase, measured by STM [108]. Note that the bulk orthorhombicity is only 0.7%. As the doping increases, the bulk AFM ordering gets suppressed, accompanied with the decrease of surface orthorhombicity, clearly indicating the strong coupling between spin and lattice especially at the surface. Our recently electron energy loss spectroscopy (EELS) experiments [28] report the temperature dependence of two phonon modes for two compositions of $Ba(Fe_{1-x}Co_x)_2As_2$ with $x = 0$ and $x = 0.05$. The observed surface transition temperature is appreciably higher than in the bulk (see Fig. 1.5 in chapter 1), and the temperature dependence of the vibrational modes in the low temperature phase is dramatically different from in the bulk. An example is in Fig. 5.2b and 5.2c (150 K vs. 136 K). The energy of the A_{1g} mode (out-of-plane As vibration) at the surface of parent $BaFe_2As_2$ is displayed as a function of temperature, and should be compared with the bulk mode. The surface surely has tipped the balance between the competing phases.

(1×2) surface in the previous chapter has been demonstrated to be a half-Ba layer strongly coupled to bulk AFM ordering at the surface Fe-layer. In this chapter, we firstly try to identify the surface termination layer and structure for ($\sqrt{2}\times\sqrt{2}$)R45° phase. Then our STM reveals π-phase shifted domains between ($\sqrt{2}\times\sqrt{2}$)R45° structures. The symmetry of the associated domain walls is lower than the lattice symmetry expected from the bulk or seen by STM within a single domain. We argue that this is a result of the strong coupling between AFM ordered

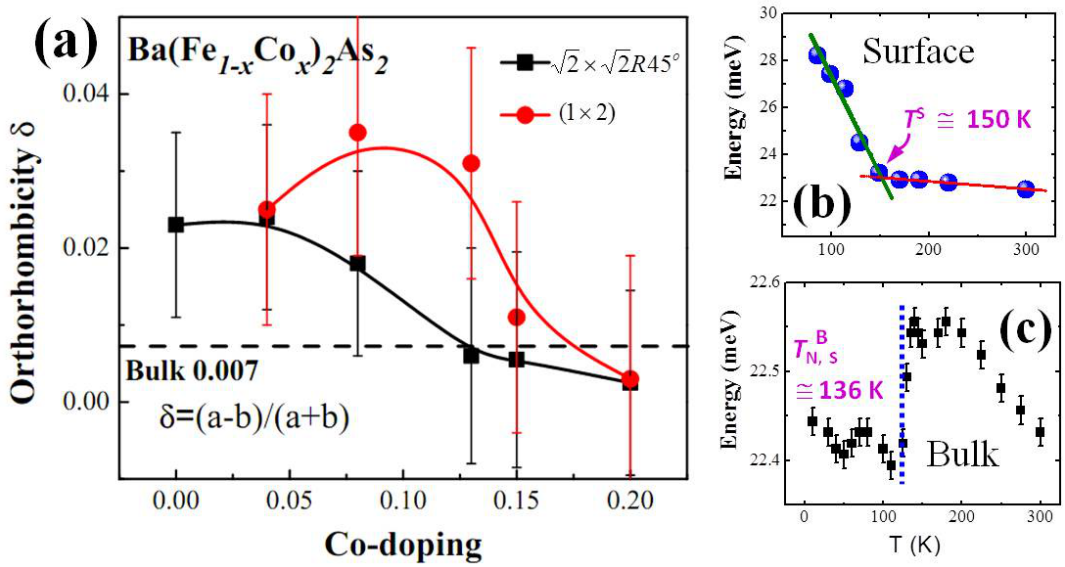

FIGURE 5.2. (a) Surface orthorhombicity vs. doping in $Ba(Fe_{1-x}Co_x)_2As_2$ measured by STM. Figure derived from [108]. (b) Raman measurements of the temperature dependence of the peak position of the A_{1g} mode in bulk $BaFe_2As_2$ [135]. (c) The temperature-dependent phonon shift of A_{1g} surface mode of $BaFe_2As_2$ [28].

spins and electrons at the surface, which causes the coexistence of an antiphase spin domain boundary with the antiphase structural boundary.

5.2 Coexisting Phases at the surface of A122 Compounds (A=Ba, Sr, Ca)

5.2.1 STM topography

STM observed a variety of topographies from the surface of $A122$ parent and doped compounds (A = Ba, Sr, Ca) [113, 114, 64, 136, 137], especially in Ba122 [115, 89, 117, 116, 109]. A review by Hoffman discussed the topographic features observed by different groups [118]. Figure 5.3 shows several typical surface topographies at $BaFe_2As_2$ surface. After cleaving at 80 K, the surface exhibits coexistence of ordered and disordered surface phases (Fig. 5.3). The area of each phase can be as large as 1 square micrometer without a single step. The typical atomic corrugation on ordered surface is as small as several pm thus hard to resolve. with high bias ($1\,V$). There is no atomic step when crossing disorder to order phase in

Fig. 5.3c. Typically, in Fig. 5.3d, the brighter phase is 0.5 $\mathring{A}$ - 1.0 $\mathring{A}$ higher than the lower phase, and the height differences depends on the tunneling junction and temperature.

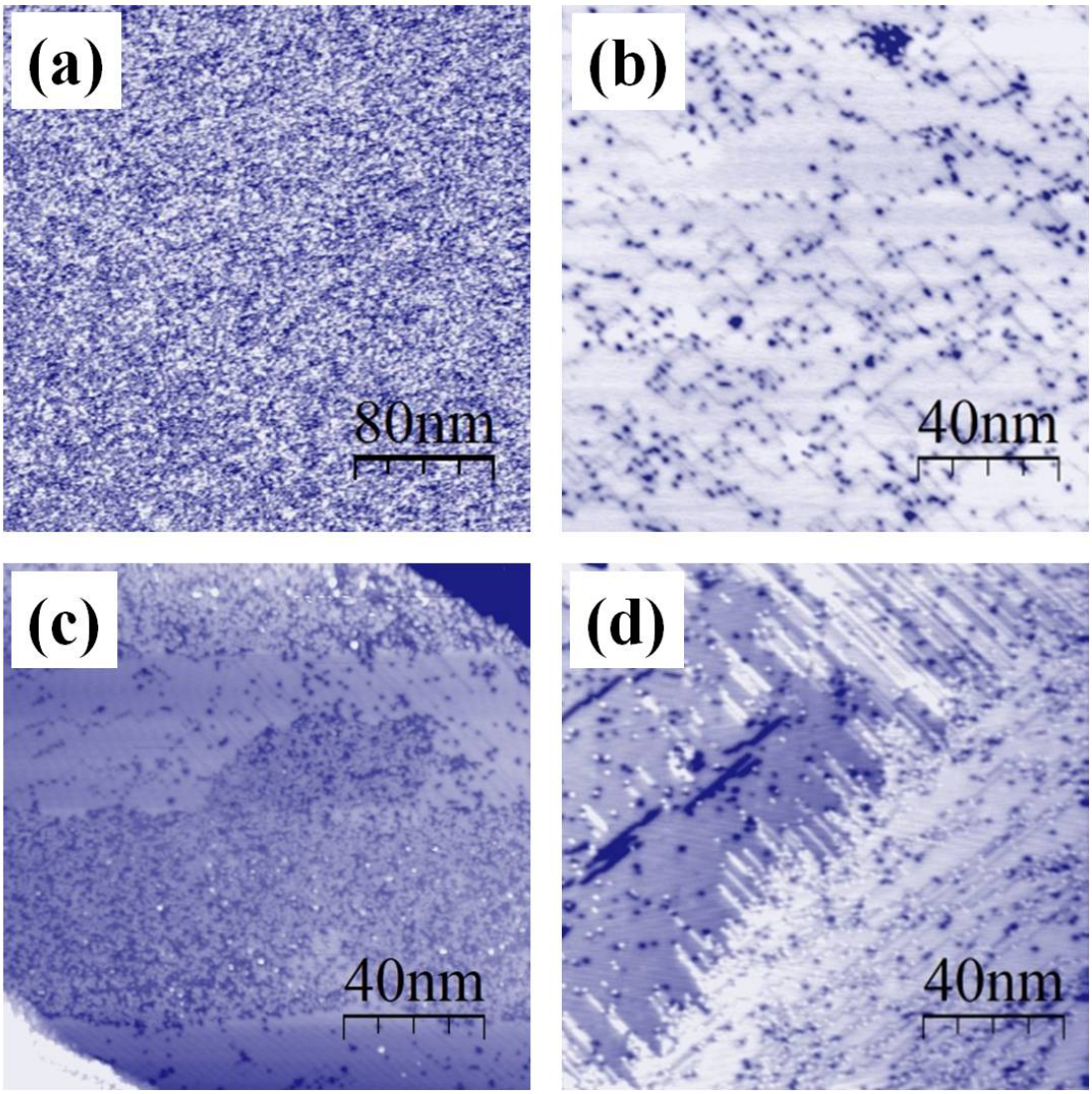

FIGURE 5.3. STM topographies of $BaFe_2As_2$ surface. (a): disorder surface. (b): order surface (c) coexistence of order and disorder phase. (d) coexistence of $(\sqrt{2}\times\sqrt{2})$R45° and 1×2 order phase. All the STM images were taken at 80 K with tunneling junction (1V, 0.2nA)

Figure 5.4 shows atomically resolved images of the ordered phases. The tetragonal unit cell is shown as the white square. In tetragonal notation, the ordered surface in Fig. 5.4a has a (1×2) unit cell, previously identified as (1×2) stripe phase.

Note that such stripe phase is already been determined as half-Ba terminated surface through LEED I-V calculation in Chapter 4. Fig. 5.4b shows a another ordered phase with $(\sqrt{2}\times\sqrt{2})$R45° unit cell which is not present on $CaFe_2As_2$ surface. The peak -to-peak atomic corrugation in Fig. 5.4b is ∼30 *pm*. This phase can be seen in Fig. 5.3b and the brighter phase in Fig. 5.3d. Note that the bias is only tens of mV during imaging the atomic resolution on $(\sqrt{2}\times\sqrt{2})$R45° phase. Only when the tip is close to the sample surface and it is sharp enough, there is a chance for atomic resolution for the $(\sqrt{2}\times\sqrt{2})$R45° phase. Most of the time, the atomic corrugation is too small to be resolved. For example, when the tip is able to resolve the atomic resolution of (1×2) stripe phase, it only produces flat featureless line scans on $(\sqrt{2}\times\sqrt{2})$R45° phase when STM is imaging at the interface. STM studies also reported a rarely seen atomic resolved (1×1) phase in $Pr_xCa_{1-x}Fe_2As_2$ [137] and $BaFe_2As_2$ [138].

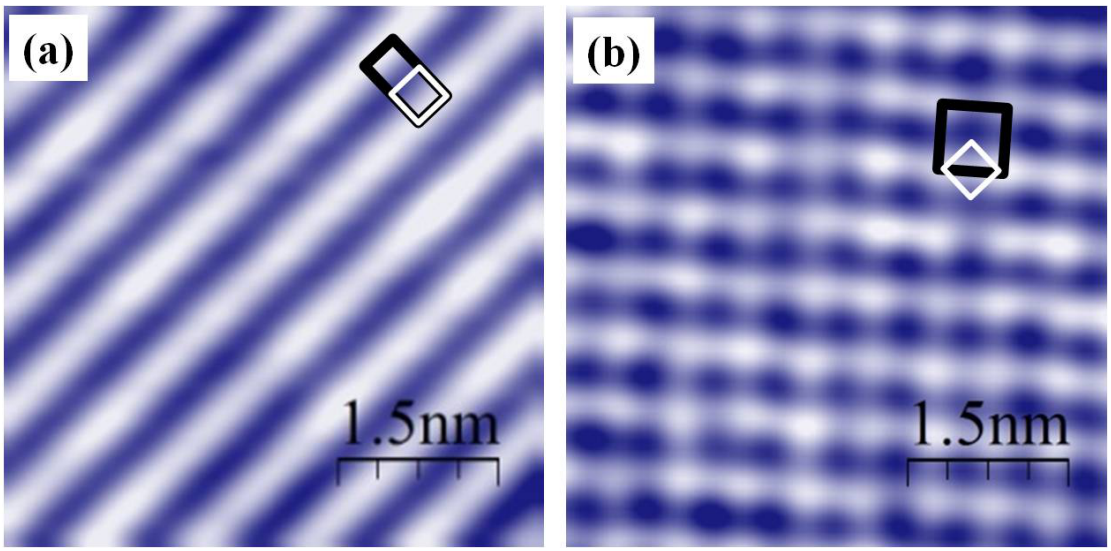

FIGURE 5.4. Atomic resolution of STM topographies on ordered surface of $BaFe_2As_2$ surface. (a): (1×2) phase (b): $(\sqrt{2}\times\sqrt{2})$R45° phase. Black rectangular and square indicate the unit cells.

When cleave, Ba layer will either be divided partially on each surface. The way the Ba atoms distribute on the As surface leads to the diversity of the STM

topographies[115, 89, 117, 116, 109]. The obvious way is diving into half and half, thus each surface avoids being polar. A full-monolayer of either Ba or As termination is a polar surface thus it is unlikely to be the stable phase without reconstruction, which has higher surface energy forcing structure or electronic reconstruction [139]. 0.5 ML Ba termination is a neutral surface and Ba atoms seems able to rearrange themselves at the top surface, appearing a diverse topographies observed at the surface including ordered (1×2), ($\sqrt{2}\times\sqrt{2}$)R45°, and disordered phases [89].

Figure 5.5 shows the varies structural models proposed for Ba-terminated surface [89, 140]. The black dots are the Ba lattice positions as they would be in the bulk and the green circles are actually occupied Ba atoms. Fig. 5.5a shows half-Ba terminated (1×2) order with alternatively missing Ba rows. Figure 5.5b shows half-Ba terminated ($\sqrt{2}\times\sqrt{2}$)R45° order where the nearest neighbors of Ba atoms are missing. Fig. 5.5c shows an interface of (1×2) and ($\sqrt{2}\times\sqrt{2}$)R45° order. Fig. 5.5d shows a surface with randomly distributed Ba atoms. Fig. 5.5e shows an anti-phase domain wall of (1×2) stripe phase. Figure 5.5f and 5.5g shows two types of anti-phase domain walls of ($\sqrt{2}\times\sqrt{2}$)R45° phase. At last, Fig. 5.5h shows half the area Ba atoms forming (1×1) order and the other half area without any Ba atoms - which is the As-terminated surface. All of these configurations guarantees a overall half monolayer of Ba atoms at the surface.

5.2.2 LEED pattern and I-V analysis

LEED experiments can detect the coherent structure of the surface. Initially, the $BaFe_2As_2$ sample was cleaved at room temperature and cooled down to 20 K, producing a (1×1) pattern (Fig. 5.6a) without fractional spots [117]. Subsequently, the sample was cleaved at 87 K, showing a LEED pattern (Fig. 5.6b) with additional fractional spots which are identified to be associated with ($\sqrt{2}\times\sqrt{2}$)R45° and (1×2) order. Note that the red arrows in Fig. 5.6 are pointing to the same

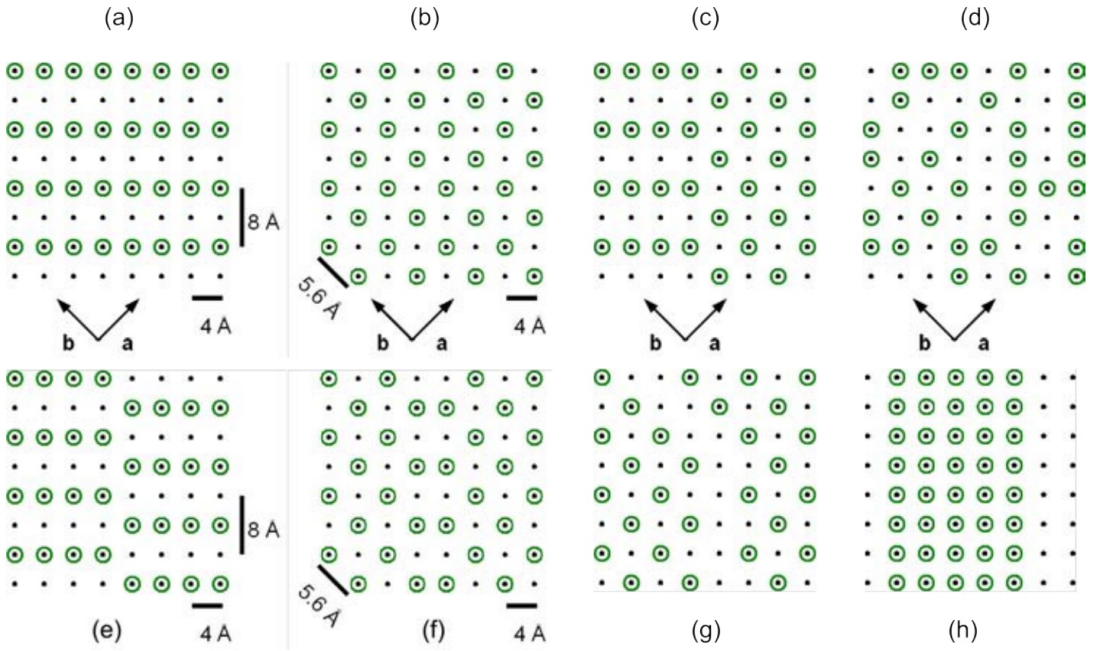

FIGURE 5.5. Structure models for Ba-terminated surface phases. It organizes to different ordered phases including $(\sqrt{2}\times\sqrt{2})$R45° and 1×2 phases. Figure is adapted from reference [140]

location which has $(\sqrt{2}\times\sqrt{2})$R45° fractional spot in Fig. 5.6b & c. Fig. 5.6b is identical to the LEED pattern in Fig. 5.6c, which is simulated from a surface with multiple phases (1×1), $(\sqrt{2}\times\sqrt{2})$R45° and (1×2) twin domains. The circled white dots are corresponding to integer spots associated to tetragonal (1×1) lattice. The white dots without circles are associated to $(\sqrt{2}\times\sqrt{2})$R45° order. The red dots are associated to (1×2) and blue dots to (2×1) domain. A sample cleaved at low temperature correctly produces all the fractional spots associated to the superlattice observed in STM images. Thus, the surface is a mixture of (1×2) twin domains, $(\sqrt{2}\times\sqrt{2})$R45°, and possible (1×1) ordered phases. Momentum space observation from LEED is consistent with the real space images by STM.

There are three structural models for $(\sqrt{2}\times\sqrt{2})$R45° phase, namely 1 ML As-termination with buckling, 1 ML Ba termination with buckling and 0.5 ML Ba-termination in Fig. 5.7. The full monolayer termination of either As or Ba has

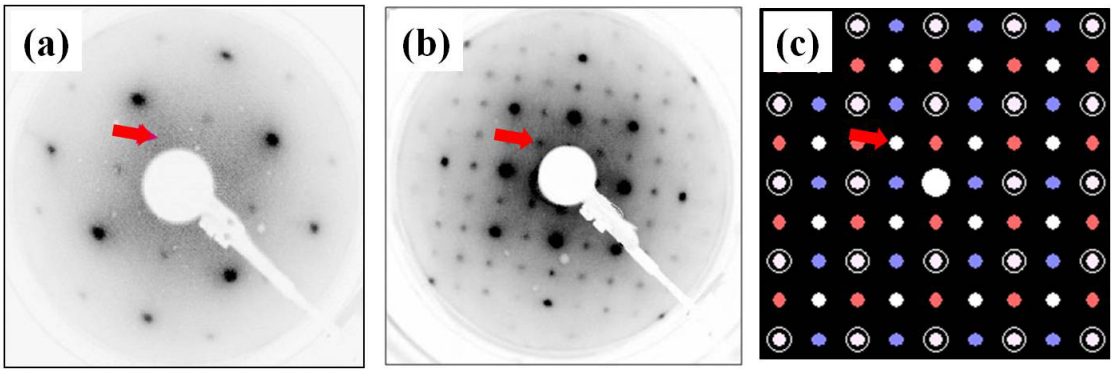

FIGURE 5.6. LEED pattern from $BaFe_2As_2$ surface. (a) is measured at 20K from the room temperature cleaved sample. (b) is measured at 87K from the sample cleaved at the same temperature. (c) Simulated LEED pattern from a mixed phases of 1×2 with twin domains and $(\sqrt{2}\times\sqrt{2})$R45° phase.

one atom buckled down at the center and one buckled up at the corner of the $(\sqrt{2}\times\sqrt{2})$R45° (or (1×1) in orthorhombic notation) unit cell. In half monolayer of Ba model, the center Ba is simply missing. All the three models have the same $(\sqrt{2}\times\sqrt{2})$R45° unit cell and could lead to a LEED pattern in Fig. 5.6b with (1×2) stripe twin domains.

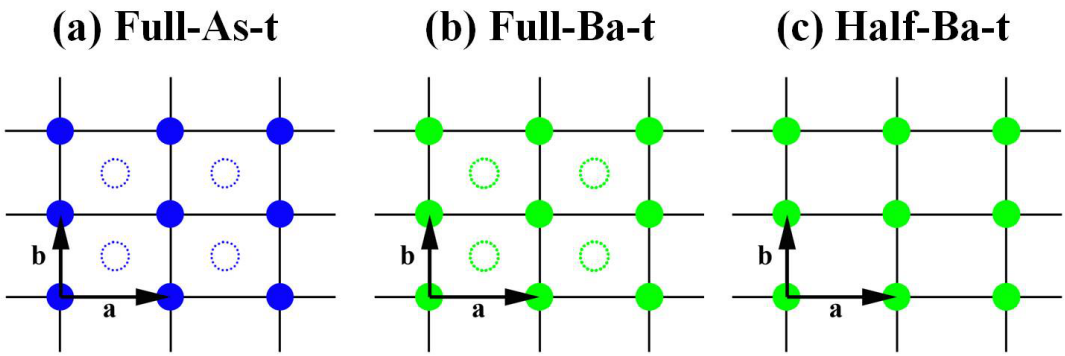

FIGURE 5.7. Three possible structural models for $(\sqrt{2}\times\sqrt{2})$R45° phase. (a): 1 ML of As termination buckled model. (b): 1 ML of Ba termination buckled model. (a): 0.5 ML of Ba termination model.

As shown in Fig. 5.6c, the white dots without circles correspond to $(\sqrt{2}\times\sqrt{2})$R45° periodicity. Thus the diffraction LEED spots at the same positions in Fig. 5.6b are solely related to the $(\sqrt{2}\times\sqrt{2})$R45° phase in STM images. They can be used for I-V analysis. Heumen et al [119] have collected these I-V curves on Co-doped Ba122 un-

der 20 K shown in Fig. 5.8 with total energy range 1782 eV. In half-Ba terminated model, if only relax the top Ba layer, the R_p is 0.31. If the first As-Fe_2-As layer was allowed to relax, the best R_p is 0.19. Other models gave a significant higher R_p. They thus concluded that the $(\sqrt{2}\times\sqrt{2})$R45° phase is half-Ba terminated surface.

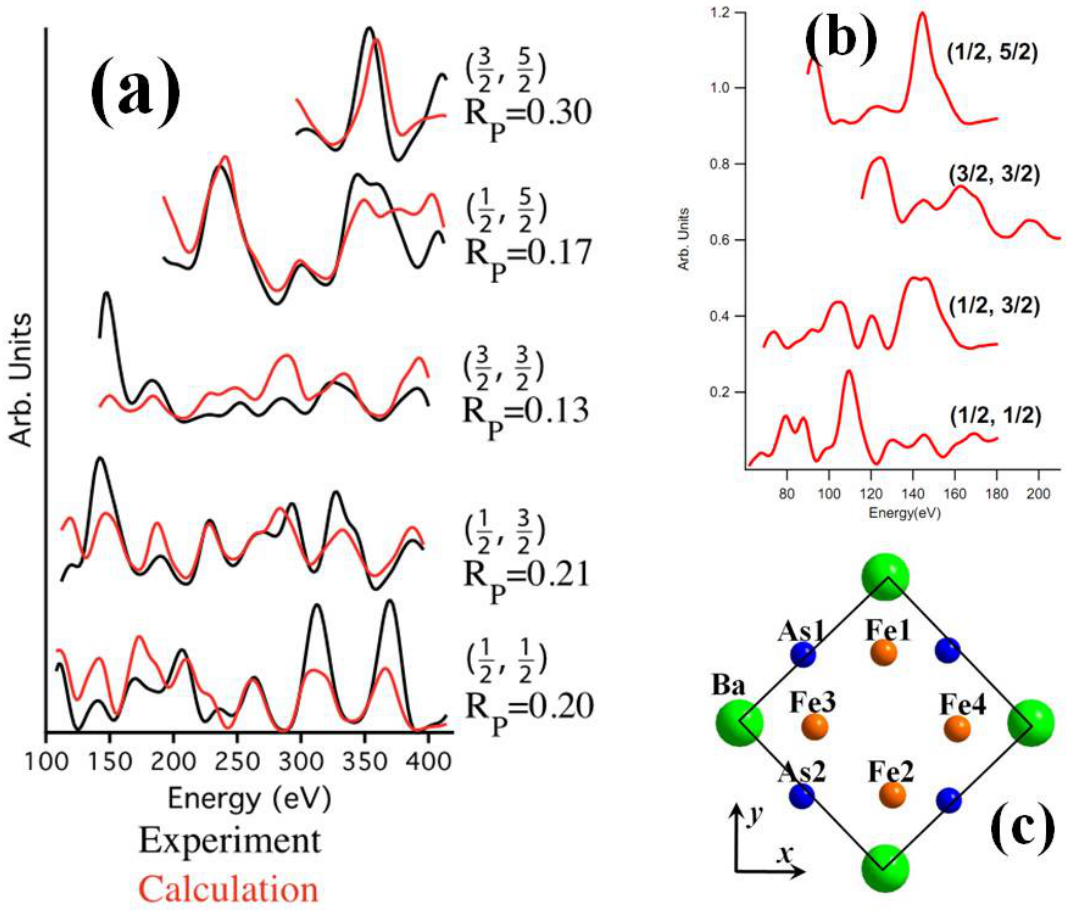

FIGURE 5.8. (a) Experimental and theoretical comparison of LEED I(V) curves for fractional spots associated to $(\sqrt{2}\times\sqrt{2})$R45° phase, Figure adapted from reference [119]. (b) Experimental LEED I(V) curves for fractional spots associated to $(\sqrt{2}\times\sqrt{2})$R45° phase from Fig. 5.6. (c) Top-view of $(\sqrt{2}\times\sqrt{2})$R45° structure determined by reference [119].

However, there is an important issue that needs to be pointed out. Traditionally, LEED calculation assumes the in-plane crystal symmetry during structure refinement for two purposes. One is that in reality the atoms in the unit cell follow certain symmetry operation, for example, two-fold in orthorhombic structure and

four-fold in tetragonal structure as well as the mirror operation, which are typically determined by the symmetry of bulk-truncated surface. The second purpose is that it allows refinement of less structural parameters thus it provides a more accurate structural determination. Failure to do so may lead to unrealistic results due to too many fitting parameters.

In Heumen et al's calculation [119] there is not any symmetry implied during the structural refinement in $(\sqrt{2}\times\sqrt{2})$R45° phase. Table 5.1 shows their determined structure of half-Ba terminated $(\sqrt{2}\times\sqrt{2})$R45° surface where more details can be found in the supplemental material of the reference [119]. Table 5.1 mainly shows the surface lattice distortion compared to bulk in x, y, z direction which are the axis directions of the tetragonal lattice. Note that Ba is in origin position. Because there is no symmetry restriction during the structural refinements, the optimized structure does not have the symmetry of the unit cell. As1 and As2 are all moved about $0.5\mathring{A}$ in plane and they do not stay in the middle of nearest Ba-Ba pair. All the four Fe atoms are different and one of them even moved 0.4 $\mathring{A}$ in plane. If considering the z direction, there is buckling of 0.14 $\mathring{A}$ at the Fe plane and all four Fe atoms and two As atoms buckled differently.

TABLE 5.1. Half-Ba terminated $(\sqrt{2}\times\sqrt{2})$R45° surface structure determined by LEED I-V analysis, derived from reference [119].

$BaFe_2As_2$	Bulk positions			Surface distortions		
Atom	x	y	z	Δx	Δy	Δz
Ba	0	0	0	-0.1834	-0.2012	0.1717
As1	1.978	1.978	1.8926	-0.4386	-0.3257	0.1085
As2	1.978	-1.978	1.8926	-0.4721	-0.2129	0.1335
Fe1	3.9559	1.978	3.2363	-0.2251	-0.2676	0.0931
Fe2	3.9559	-1.978	3.2363	0.0127	-0.1781	0.0506
Fe3	5.9339	0	3.2363	-0.2052	-0.3662	0.1415
Fe4	1.978	0	3.2363	-0.1192	-0.3138	0.1469

Our LEED I-V curves (Fig. 5.8b) for $(\sqrt{2}\times\sqrt{2})$R45° fractional spots at 87 K from the LEED pattern in Fig. 5.6b, covers insufficient energy range to obtain a structure. The estimated Debye temperature of Ba layer is low (60 K), this leads to irreversible fade out of the fractional spots above 150 K [119]. Thus, the I-V curves collected at 87 K in this thesis in Fig. 5.8b from fractional spots of $(\sqrt{2}\times\sqrt{2})$R45° are most in lower energy region and have a total energy range of 421 eV which is much less comparing to 1782 eV range in Heumen et al's data [119]. Initial LEED I-V analysis was done with the 2-fold and mirror symmetry restriction unfortunately leads to unacceptable Rp with all three structure models. We believe this could be solely due to the reduced energy range as well as the stability of the $(\sqrt{2}\times\sqrt{2})$R45° phase because the LEED pattern starts to fade out at 100 K which is just 13 K above our measurement temperature [89].

5.2.3 Theory

First-principles density function theory calculations were conducted on this surface to clarify the experimental controversial results about the surface termination. Gao et al [121] adopted the generalized gradient approximation (GGA) and found that energetically the most favorable cleaved $A\mathrm{Fe_2As_2}(001)$ surface is half A-terminated with either $(\sqrt{2}\times\sqrt{2})$R45° or 1×2 order. Table 5.2 has summarized the energy of each phases in $\mathrm{AFe_2As_2}(001)$ surface. These competing phases have energies close to each other, which seems depending on the choice of spacer atoms A. For $\mathrm{BaFe_2As_2}$, half-Ba terminated $(\sqrt{2}\times\sqrt{2})$R45° phase has the lowest energy thus the area of such phase dominates the surface. In contrast, for $\mathrm{CaFe_2As_2}$, the lowest energy phase is half-Ca terminated (1×2) order which is the most common phase at the surface of Ca122. The conclusion of a dominated $(\sqrt{2}\times\sqrt{2})$R45° phase in Ba122 and (1×2) phase in Ca122 is consistent with STM observation.

TABLE 5.2. Relative energies of two $(\sqrt{2}\times\sqrt{2})$R45° A-terminated sur- faces and two (1×2) A-terminated surfaces with respect to a (1×1) A-terminated plus a (1×1) As-terminated surfaces in the NM tetragonal phase and the AFM orthorhombic phase, respectively. The energy unit is meV/(1×1 cell).Here the surface atoms are set in the corresponding bulk positions. Considering reconstruction, only As-terminated surface takes further reconstruction with a very small energy gain of 3.9 meV/(1×1 cell).

AFe_2As_2	NM tetragonal		AFM orthorhombic	
(001)	$2\times(\sqrt{2}\times\sqrt{2})$R45°	2×(1×2)	$2\times(\sqrt{2}\times\sqrt{2})$R45°	2×(1×2)
$BaFe_2As_2$	-411.6	-217,8	-534.8	-312.0
$SrFe_2As_2$	-217.0	-167.8	-314.6	-219.0
$CaFe_2As_2$	-34.0	-97.0	-185.4	-189.2

Further, Gao *et al* [121] design an ideal adiabatic cleaving process, in which a sample is divided into two parts by separating two neighbor FeAs layers gradually away from each other. They found that a fast cleaving may readily remove the completely layer of A atoms on the surface and yield a metastable As-terminated surface with a few randomly assembled A atoms. If the cleaving is done at very low temperature, this metastable structure can remain on the surface for a long time. They found no reconstruction of this metastable As-terminated surface if the bulk is nonmagnetic phase. Moreover, at low temperature AFM ordered orthorhombic phase, there will be a $\sim 0.1\mathring{A}$ buckling of As-terminated surface to gain energy by lifting the degeneracy of energy band from the breaking of mirror symmetry. The buckling creates a $(\sqrt{2}\times\sqrt{2})$R45° order where there is a charge transfer between inward As atom and outward one. This leads to explanation that STM can observe the inward and outward atoms at a positive and negative bias, respectively. However, STM experiments do not seen any switchable bias-dependent STM images at $A122$ compounds except in in $K_{0.73}Fe_{1.67}Se_2$ [111]. It is argued to Se-terminated $(\sqrt{2}\times\sqrt{2})$R45° surface, which might be different from As-terminated surface [111].

Another DFT calculation using GGA revealed three possible terminations: full monolayer of As, full and half Ba coverage can all be stabilized in different chemical-potential ranges [141]. They studied the structural and magnetic properties of

each phase and revealed a surface phase diagram as well as termination-dependent changes in the work functions. The results of surface phase diagram are summarized in Fig. 5.9. The surface with 1ML layer Ba coverage is energetically stable at rather large Ba concentrations, or when the chemical potential of Ba is about 1 eV smaller than the Ba-bcc cohesive energy. 0.5 ML layer of Ba coverage becomes energetically favored at intermediate range of the chemical potential of Ba. At rather low Ba concentrations, the As-terminated becomes the most stable. The coexistence of three different phases in a rather limited range of Ba chemical potential seems responsible for complex surface phases observed in A122 compounds.

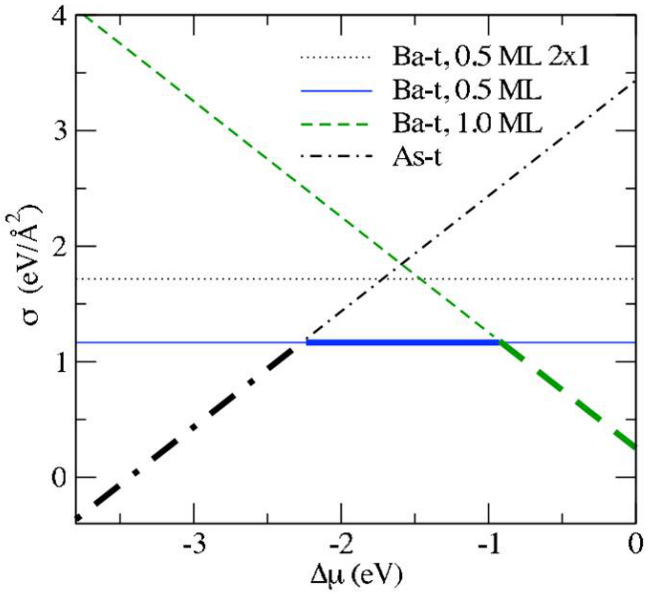

FIGURE 5.9. Surface energy per unit surface area for the different surface terminations considered as a function of Ba chemical potential. Thick lines represent the stability path.

They analyzed the electronic properties of each phase. First, their calculated magnetic moments [141] show an enhancement of the Fe magnetic moments at the surface layer for all the Ba-terminated surfaces while a much smaller magnetic moment is found on the As-terminated surface, $\sim$0.4 u_B. The lower magnetic moment at the As-terminated surface is argued to be related to the shift toward lower

binding energy experienced by the Fe minority states because of the connection between structural Fe-As distance and magnetic properties. Note that experimentally an enhanced orthorhombicity was observed at Ba122 surface, indicating no reduction of magnetic moments at the surface, which is in contrast As-terminated surface.

They further simulated the constant-current STM images on the three different terminations of the $BaFe_2As_2$ surface within the Tersoff-Hamann approach. The simulated STM images at As-terminated surface are (1×1) ordered and show no bias dependence at positive and negative 0.2 *V*. The ones at half-Ba terminated surface show $(\sqrt{2}\times\sqrt{2})$R45° order and interestingly the image shows a 2-fold symmetry rather than 4 fold. This implies that the surface LDOS is greatly affected by the lattice orthorhombic lattice symmetry. The full monolayer of Ba-terminated surface is interesting that the electronic effects dominates over the structural ones and the bright protrusions do not correspond to the top most Ba species rather to the subsurface As and Fe atoms. This provides another example that the assumption that the bright protrusions corresponds to the top surface atoms is questionable if using only STM topography to identify the surface termination.

Importantly, their DFT calculations showed surface termination-dependent work functions, allowing the local work function measurement by STM be used to determine the surface termination. It turns out the As-terminated surface has a higher work function of 5.0 V while half-Ba covered $(\sqrt{2}\times\sqrt{2})$R45° surface strongly reduce the work function to 1.4 V due to the dipole layer forming at the surface. 1 ML of Ba layer coverage increase the work function to 2.8 V, close to the Ba bulk element work function. Massee et al found a work function of 1.5 eV at both $(\sqrt{2}\times\sqrt{2})$R45° and (1×2) phase, suggesting the same termination layer for both phases in the Co-doped Ba122 compounds [142]. Our DFT calculation of work

function on the stripe phase of Ba122, if with a half-Ba terminated model as our Chapter 4 discussed, is 1.56 eV. (More details of work function comparison can be found in Appendix B.) Thus, the $(\sqrt{2}\times\sqrt{2})$R45° is the half-Ba terminated surface.

5.3 Coupled Structural-Magnetic Antiphase Domain Walls on $BaFe_2As_2$

5.3.1 Broken mirror symmetry

In this section, we detailed studied the $(\sqrt{2}\times\sqrt{2})$R45° phase. Applying a small bias (tip closer to sample) produces an atomically resolved image in a region with no defects in the Fig. 5.4b. This image shows a square-like lattice with unit cell $\sim$ (5.6 $\mathring{A}$ × 5.6 $\mathring{A}$), which is the $(\sqrt{2}\times\sqrt{2})$R45° phase in the tetragonal notation[117]. The difference in the $(\sqrt{2}\times\sqrt{2})$R45° unit cell seen with STM and the bulk truncated surface is that there is only one bright protrusion in each unit cell in the STM image in contrast to two atoms in the (1×1) unit cell in the bulk, for a complete surface layer of As or Ba. Fig. 5.1b and 5.1c show top-view of bulk-truncated surface with two atoms in $(\sqrt{2}\times\sqrt{2})$R45° unit cell as expected while Fig. 5.7c shows only one atom and the other one in the center of $(\sqrt{2}\times\sqrt{2})$R45° unit cell is invisible. The exact termination for this phase is controversial in the literature. It could be a half monolayer of Ba, a full layer of Ba or As with a distortion that makes one of the two surface atoms invisible. We discussed in previous section that it is likely a half-Ba terminated surface. However, any of these terminations would have the bulk C_{2v} symmetry. Thus, it makes no difference on the observed broken symmetry addressed later in this section. Note that the blue atoms in figures of this section can also be Ba atoms as well.

Fig. 5.10a shows a low-bias (23mV) atomically resolved image, but with a larger field of view (355 $\mathring{A}$× 355 $\mathring{A}$). The randomly distributed (large and fuzzy) spots were previously reported as Ba atoms[117]. Note, in addition to the clear

($\sqrt{2}\times\sqrt{2}$)R45^o ordered structure, there are periodic white blobs forming zigzag lines. Also, there are dark spots, which appear to be randomly distributed and are most likely defects/vacancies on the surface, but the zigzag line changes direction at a dark spot. When the bias voltage is increased to 483 mV (or $1V$ as in Fig. 5.3b) there is a dramatic change in the contrast in the STM image, as shown in Fig. 5.10b. Under these higher bias voltages atomic resolution is lost but the zigzag lines become dark, while the dark defects seen in the low-bias image remain dark. The large-scale images show that the zigzag lines form closed loops which separate the surface into different regions, i.e., domains. Figure 5.11 shows a series of STM images at 23 mV but colored adjacent domains. A contrast reversal as seen at the domain walls from Fig. 5.10 means that the origin of the image is primarily electronic, since STM only "sees" charge density. This observation is not due to a change of the tip or sample condition because the contrast reversal is reproducible by changing the bias from 23 mV to 483 mV back to 23 mV.

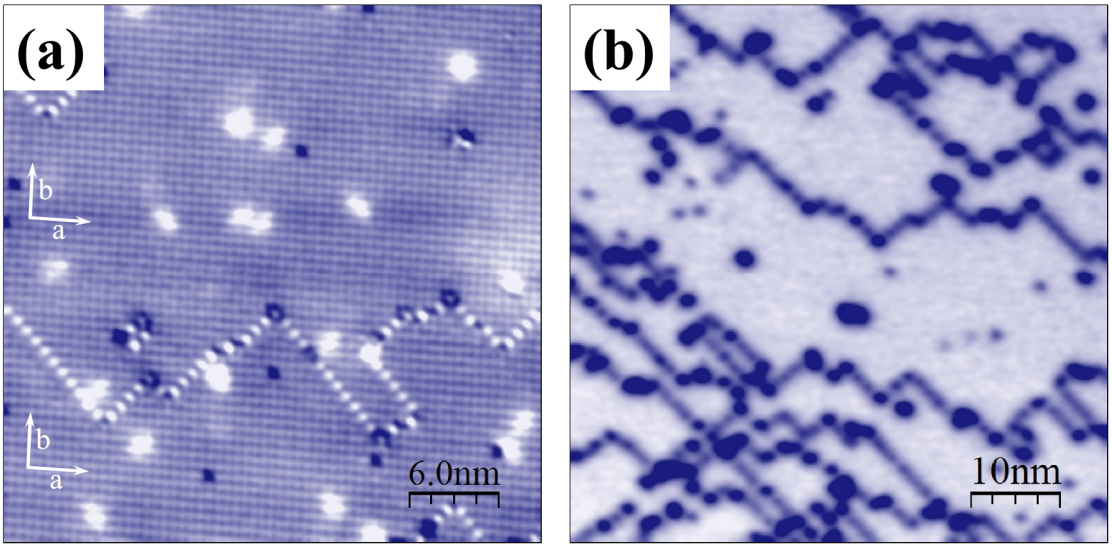

FIGURE 5.10. Two typical constant-current (I_{tip} = 200 pA) STM topographic images with different positive bias voltages on the square-like ($\sqrt{2}\times\sqrt{2}$)R45^o (001) surface at 80 K: (a) A 35.5 nm × 35.5 nm image at low-bias (23 mV) and (b) 70 nm × 70 nm image at high-bias (483 mV), respectively.

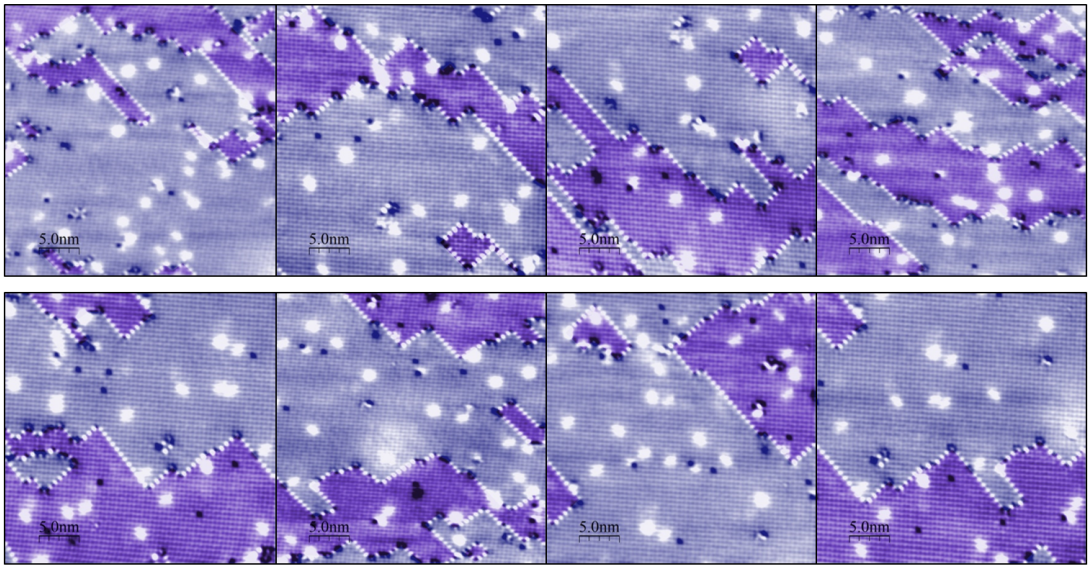

FIGURE 5.11. A series of constant-current (I_{tip} = 200 pA, V_{Bias} = 23 mV) STM topographic images on the square-like ($\sqrt{2}\times\sqrt{2}$)R45^o (001) surface at 80 K. The purple color represents the adjacent domains.

Figures 5.12a and 5.12b show two images of different domain walls that change directions at a defect. In each image there are two boundaries along different diagonal directions, one $\sim$ 45° and the other $\sim$ - 45° (Fig. 5.12a) or $\sim$ 135° (Fig. 5.12b) with respect to the *a* direction. As can be seen in both figures, the adjacent ($\sqrt{2}\times\sqrt{2}$)R45° domains are shifted by half orthorhombic unit cell as indicated by arrows, i. e., an antiphase domain wall. All of the bright white blobs residing on both boundaries have elliptical shape, but a closer examination reveals that the white blobs along the - 45° direction are less elliptical. A quantitative difference is seen in the line profiles along these two boundary directions as shown in Fig. 5.12c and 5.12d, respectively. The line profile oscillates with the same periodicity along both directions, but the amplitude for the blobs in 45° direction (red lines) is about double compared to that along - 45° direction (green lines). We emphasize that such difference is not due to anisotropic tip effect as the same result is obtained by different tips in different regions.

If one examines the symmetry carefully it is clear that the domain walls exhibit only C_2 symmetry. Rotating the image in Fig. 5.12b by 180° transforms the 135° boundary into a - 45° boundary which is identical to the - 45° boundary in Fig. 5.12a, as expected if the boundary direction is unchanged. But if we reflect the Fig. 5.12a and Fig. 5.12b about the structural mirror plane ac- and bc-plane respectively, the 45° boundary is different from the - 45° boundary in Fig. 5.12a and the 135° boundary is different from the 45° boundary in Fig. 5.12b. This means that the mirror symmetry is broken at the domain wall.

5.3.2 Coupled structural and magnetic antiphase domain walls

In bulk, the simplest structural domain wall would be a twin boundary, where the directions of a and b are swapped. We were able to determine that the directions of a and b do not change across the boundaries, as indicated in Fig. 5.10a. If the directions of a and b were changed so that a was vertical in the upper domain and horizontal in the lower domain, there would be a mismatch in the alignment of the vertical columns along the domain wall, since $a \neq b$. To illustrate this, one may assume that, at the point on the domain wall farthest to the left in Fig. 5.12a, the vertical column on the upper domain is aligned half way between the two columns on the lower domain. Since this is an antiphase domain boundary there is a π phase change between the two sides. In this situation, if one moves over n vertical columns to the right in the upper domain the distance traveled is $n \times b$. On the other hand, the corresponding position on the lower domain is $(n-\Delta)a$, where Δa is the mismatch alignment due to $a > b$. Using the definition of the orthorhombicity, $\delta = (a-b)/(a+b) \approx (a-b)/(2a)$ the value of the mismatch Δ can be determined: $\Delta = 2n\delta$. For the antiphase domain walls when $\Delta = 0.5$ the bright columns on the top will be aligned to the bright columns on the bottom. For the

measured orthorhombicity of the bulk (∼0.4%), this happens when n=62. However, if we use the enhanced orthorhombicity reported for the surface (∼2%)[108] only ∼12 vertical columns are required to align the vertical columns in the upper and lower domain. The complete domain, partially shown in Fig. 5.10a, contains more than ∼123 vertical columns. A comparison of the match between the columns in the two domains from the extreme left to the extreme right shows no change, i.e. the two domains are not a result of twinning. Therefore, the domains reported here are not bulk twin boundaries but instead surface antiphase boundaries between two domains of the reconstructed surface.

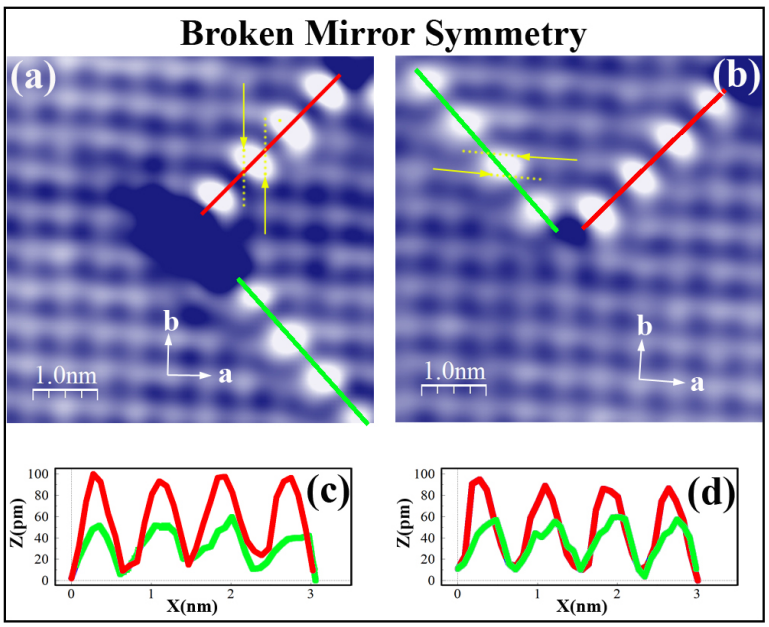

FIGURE 5.12. (a and b) Two 5.6 nm × 5.6 nm low-bias constant-current STM topographies (V_{bias} = 23 mV, I_{tip} = 200 pA) showing boundary structures at 80 K. The arrows with dash lines indicate the half unit cell shift in a and b direction respectively. (c and d) Line profiles along domain boundaries shown in (a and b). Green and red colors represent two types of domain walls in terms of shapes and intensity. (e) A schematic structure model of closed domain surrounded by another domain. The thin lines indicate the orthorhombic (1×1) unit cells. Solid and open circles represent "visible" sites and "invisible" sites in STM images, respectively. Four domain walls (45°, - 45°, 135°, - 135° refer to longer a-axis) are shown by blue thick lines, connected by dark holes (defects). On each domain wall, there are two ellipses which represent the bright blobs seen on the domain wall in STM image.

While excluding the possibility of twin domain boundaries, can the structural mismatch cause the domain walls with reduced symmetry? Figure 5.13 shows a pure structure model. To make the picture as simple as possible, the domain inside the closed boundary contains only $\sim$ 12 (1×1) orthorhombic unit cells (thin lines). The phase of the domain inside is shifted by π, both the rows and columns, with respect to the outside domain. We will refer to this as a structural antiphase domain but there is no bulk structural boundary associated with this surface domain wall. These surface structural boundaries maintain C_{2v} symmetry, so that the line profiles for the four boundaries in Fig. 5.13 would be identical. This demonstrates that a pure structure model cannot explain our observation.

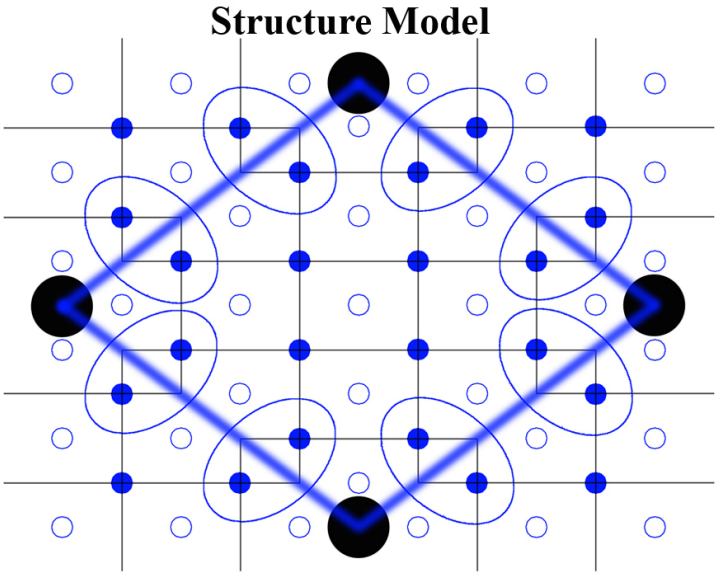

FIGURE 5.13. A schematic structure model of closed domain surrounded by another domain. The thin lines indicate the orthorhombic (1×1) unit cells. Solid and open circles represent "visible" sites and "invisible" sites in STM images, respectively. Four domain walls (45°, - 45°, 135°, - 135° refer to longer a-axis) are shown by blue thick lines, connected by dark holes (defects). On each domain wall, there are two ellipses which represent the bright blobs seen on the domain wall in STM image.

We recall that both structural and magnetic transitions occur concomitantly in $BaFe_2As_2$ [26]. Therefore, spin arrangement has to be taken into account in

any model, due to strong spin-lattice coupling. Spin, like angular momentum and torque, is known as a pseudo-vector (or an axial vector), opposed to a true or polar vector such as velocity [145]. The property of a pseudo-vector is that its mirror image is equal in magnitude but flipped in direction because a pseudo-vector has a chirality. Fig. 5.14 illustrates this feature for three different spin directions with respect to the mirror plane. The mirror images of a polar vector such as velocity are also shown. The first case is the most general situation where the spin vector is in an arbitrary direction with respect to the mirror plane. It is easy to see from this picture what happens when the spin is perpendicular to the mirror plane (case 2) or parallel (case 3). Given the bulk AFM structure of $BaFe_2As_2$ as shown in Fig. 5.15a, it is obvious that there is no mirror symmetry for either of the structural mirror planes: horizontal (along the a axis) or vertical (along the b axis). First-principle calculations show that, at the surface, the lowest energy configuration has the same spin structure as the bulk [121]. Therefore, the model shown in Fig. 5.15a is well justified to represent the surface situation. Inspection of this single-phase spin domain shows that the symmetry has been reduced to C_2 [144]. The top-left wall is the same as the bottom-right wall but different from the other two (which are identical to each other). Rotation by 180° takes the top-left wall into the bottom-right, and the bottom-left into the top-right, but there is no mirror symmetry, i. e. C_2 symmetry. Still, there are several experimental facts that would seem to rule out this single-phase spin domain picture. First, the STM images of a region without a wall for both ordered structures have C_{2v} symmetry. Second, there is no evidence in the literature from angle-resolved photoemission measurements of detwinned samples that the spin/charge coupling breaks the mirror symmetry [146]. Finally, although we know that the spin ordering breaks mirror symmetry, the spin configuration itself on domain walls is identical to the one within the clean

domain. For example, it is hard to believe the white blob on 45° domain wall can be different from the one on - 45° domain wall since the surroundings show an almost identical spin configuration.

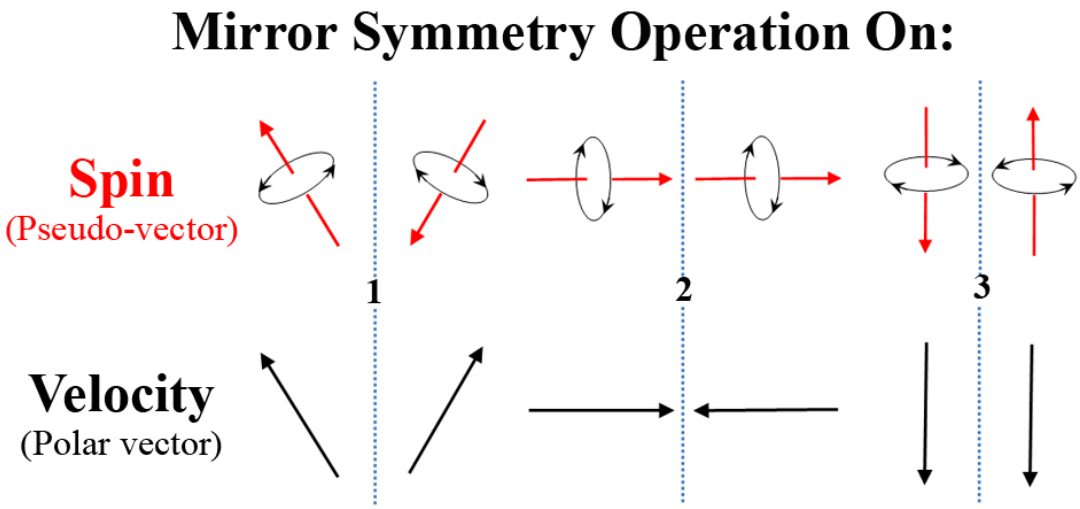

FIGURE 5.14. Mirror symmetry operation on spin (pseudo-vector) and velocity (polar vector) for a vertical mirror plane (out of page) shown by the dashed lines.

One plausible scenario is that spin antiphase domain wall coexists with the structural antiphase domain wall due to enhanced spin-lattice coupling at the surface. Figure 5.15b shows such a coupled spin and lattice domain wall. The essential ingredient in this picture is that the spin ordering is locked to the structure or visa versa through the spin-lattice coupling. In Figure 5.15b, the nearest four spins of Fe atoms are always pointing inward to the "visible" solid blue circle sites in any domain. The other possible case is that the spins are always pointing outward to the "invisible" site. This is demonstrated in Fig. 5.16 where Fig. 5.16a is the structure view showing no difference of the As atoms and Fig. 5.16b&c show the two cases. As a result, when crossing structural antiphsae domain walls, there is an accompanying antiphase shift of spin ordering.

Given the coupled (locked) structural-magnetic domain model, it is possible to explain many of the experimental observations. The half orthorhombic unit

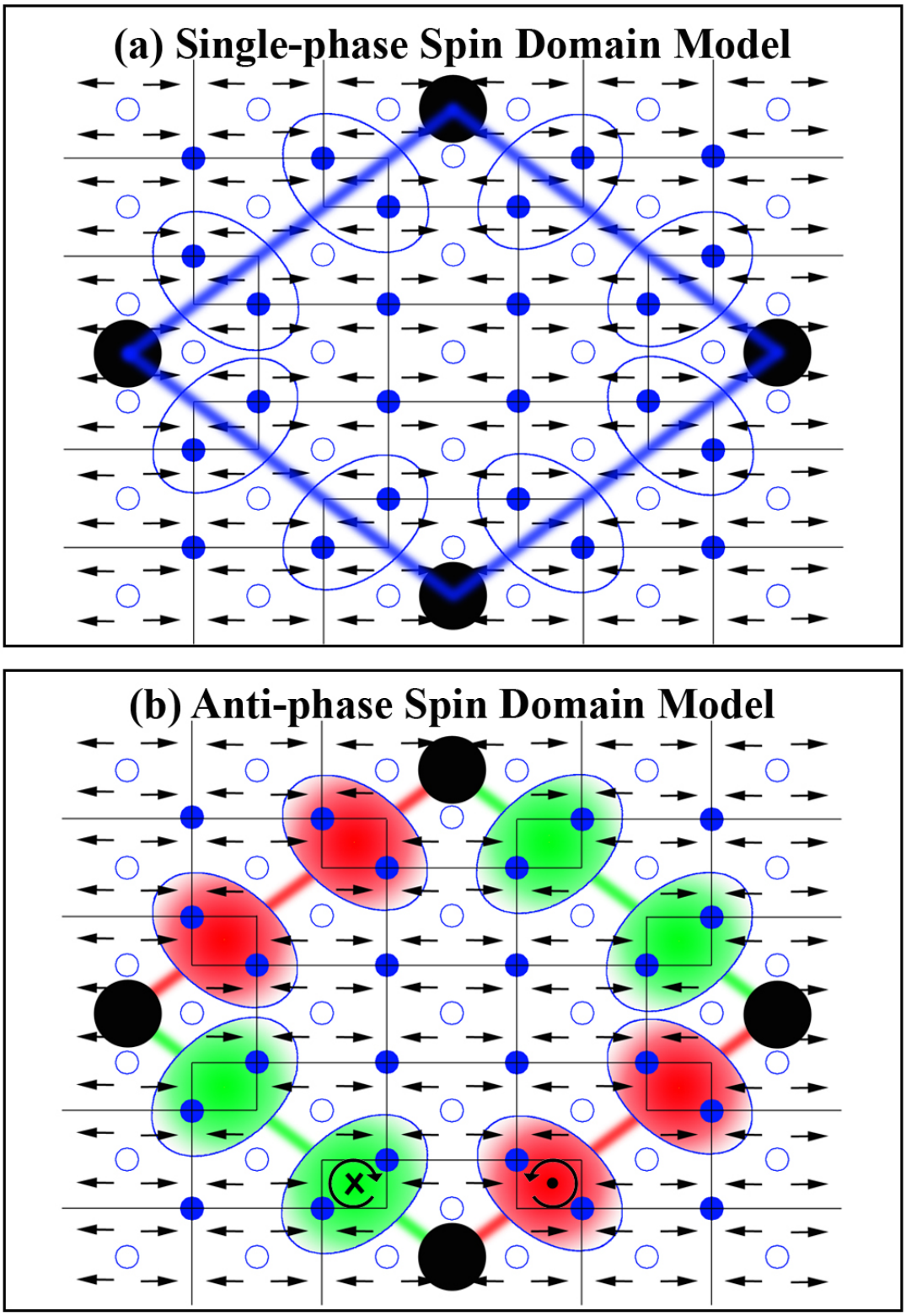

FIGURE 5.15. (a) Structural antiphase, spin single-phase domain model: bulk spin structure domain with no spin phase change crossing structural boundary. The black arrow indicates the magnetic moment on Fe atoms and its direction. (b) Coupled structural and spin antiphase domain model: bulk spin structure domains with π phase change across domain walls. The green and red colors represents two types of domain walls.

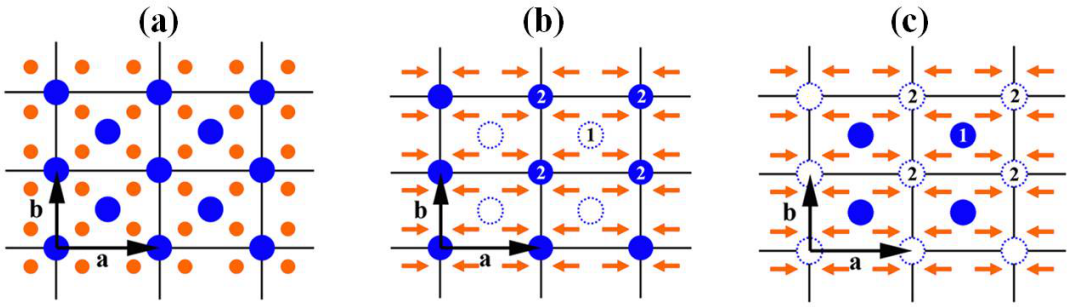

FIGURE 5.16. (a) Structural model of bulk truncated surface. Spin and structure is locked in (b) and (c) where (b): "visible" atom is the one at corner with four spin pointing towards it. (c)"visible" atom is the one at the center with four spin pointing away from it.

cell shift between adjacent structural domains is accompanied by an antiphase shift of the spin order along both AFM a axis and FM b axis when crossing boundaries. Right at the walls where adjacent antiphase spin domains meet, the spins of Fe atoms cannot fit into either domain thus are frustrated with no clear spin orientations (see the missing arrows along the walls in Fig. 5.15b compared to Fig. 5.15a). The blobs seen at the boundaries are the enhanced local density (occupied near the Fermi energy) of states due to the orbital overlap between two bright protrusions from adjacent domains. The fluctuating magnetic moments on the Fe atoms on the domain walls create two types of spin vortex arrangements around the white blobs. The red color on the ($\sim 45°$ and $\sim$ - 135°) boundaries in the Fig. 5.15b have right-hand spin chirality (indicated by the oriented circle in the bottom-right blob), while on the green color blobs on the ($\sim 135°$ and $\sim$ - 45°) boundaries have left-hand chirality (indicated by the oriented circle in the bottom-left blob). Specifically, the different chirality can be described as spin toroidal moment chirality [148]. Through the orbital-spin coupling, the parity of the spin arrangement can give rise to a deference in electronic structure which results in the different distributions of electron density of states at the domain walls as seen by STM. To understand the nature of this coupling will require a determination of

the exact structure of the surface coupled with a theory that includes the enhanced spin/lattice coupling at the surface.

Both static and dynamic antiphase spin domains have been discussed theoretically [149, 150]. In the bulk these domains seem to be dynamic. Mazin and Johannes proposed that these fluctuating domain boundaries can provide an explanation for many experimental observations that otherwise seem to be incongruent [149]. Apparently, as these experiments show, the surface can stabilize these dynamic fluctuations at an antiphase domain boundary. Never the less, it is impossible to tell how deep into the bulk this surface-driven magnetic antiphase boundary penetrates through STM measurements.

Last we pointed out that such mirror symmetry broken in this chapter was the first time been reported at the surface of iron pnictides and up to when this thesis written still been the only report. Many of the surface techniques including STM and ARPES works have observed a 2-fold symmetry but without a clear conclusion about the mirror symmetry. Thus most of them termed their observation as C_2 rather than C_{2v}. For example, quaiparticle interference was reported to 2-fold in $Ca(Fe_{1-x}Co_x)_2As_2$ [64], LaFeAsO [151], and FeSe [152] compounds. ARPES experiments also reported a 2-fold Fermi surface in $Ba(Fe_{1-x}Co_x)_2As_2$ [146] and $CaFe_2As_2$ [147].

In summary, we have shown that the surface gives us an opportunity to explore a new balance between spin and structure in $BaFe_2As_2$. An antiphase structural domain wall between different regions of the reconstructed surface stabilizes an antiphase spin domain wall, resulting in an observed reduction in the symmetry from C_{2v} to C_2. There appears to be an enhanced spin-charge-lattice coupling at the surface. This is further supported by the recent measurements of the temperature dependence of the phonon modes at the surface of $BaFe_2As_2$, which display

a gigantic enhancement in the spin/lattice coupling in the low temperature AFM orthorhombic phase [28].

Chapter 6
Surface Properties of $Sr_3(Ru_{1-x}Mn_x)_2O_7$

6.1 Introduction

Ruddleden-Popper (RP) ruthenates $Sr_{n+1}Ru_nO_{3n+1}$ ($n = 1$ to ∞) have attracted much attention because the strong coupling between charge, lattice, orbital, and spin degrees of freedom produces many exotic phenomena [9, 16]. The coupling strength can be adjusted by changing the number (n) of layers formed by RuO_6 octahedra. Among the RP series, the bi-layered $Sr_3Ru_2O_7$ ($n = 2$) is of particular interest, because of magnetic field-induced quantum criticality related to its metamagnetic transition and strong magnetic fluctuations [6]. Similar to many other transition-metal compounds, partial chemical doping on either Sr or Ru site can generate huge response in physical properties [153, 154, 155], while there may be little change in crystallographic structure. For instance, while doping with a few percent of non-magnetic ions such as Ti suppresses the metamagnetic transition [156, 157], partial replacement of Ru by another transition-metal ion like Mn, results in a metal-insulator transition (MIT) at T_{MIT} from metallic character at high temperatures to insulating behavior at low temperature (see Fig. 6.1a) [154, 155]. The X-ray absorption spectroscopy reveals that the MIT drives the onset of local anti-ferromagnetic (AFM) correlations around the Mn impurities [158]. Indeed, the system undergoes a magnetic phase transition from paramagnetic at high temperatures to long-range AFM ordering at T_M as shown in Fig. 6.1a [155]. While these two transitions diverge with increasing Mn doping, the rotation angle of octahedra decreases as well, from 8° in the parent compound ($x = 0$) to vanish at $\sim x = 0.2$ at 90 K (red dotted curve in Fig. 6.1a) [155]. Thus, the phase diagram of the

bulk $Sr_3(Ru_{1-x}Mn_x)_2O_7$ consists of several distinct regions, demonstrating that the physical properties of such a system are easily tuned by chemical doping.

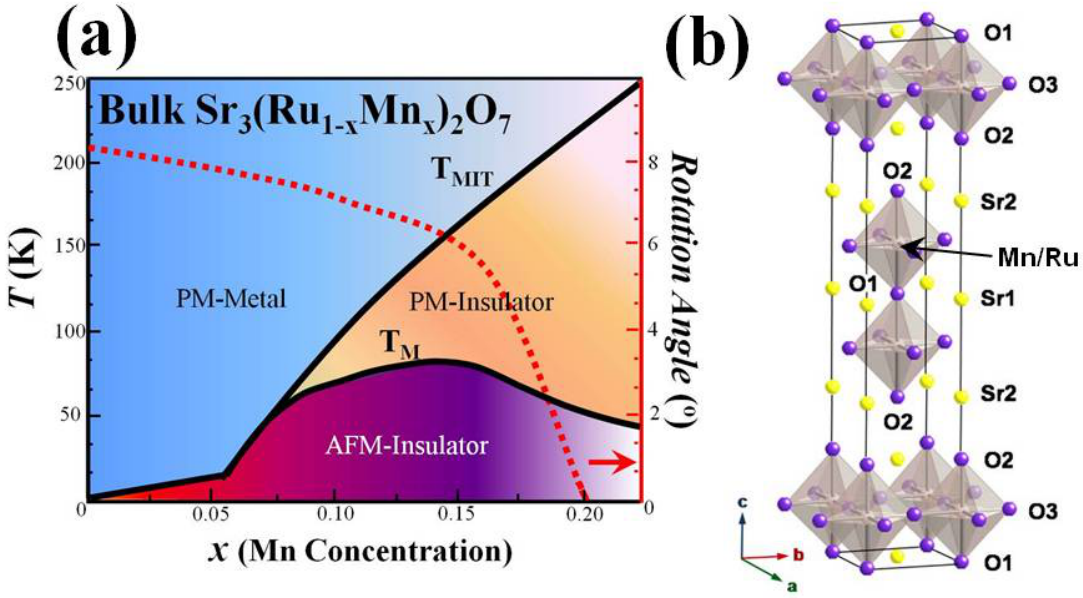

FIGURE 6.1. (a) Phase diagram of $Sr_3(Ru_{1-x}Mn_x)_2O_7$ (x<0.25), figure is reproduced from [155]. The black lines are separating each phase. The red dots curve is the bulk rotation angle of octahedra, whose scale is on the right axis. (b) Unit-cell representation of $Sr_3(Ru_{1-x}Mn_x)_2O_7$ using space group *I4/mmm*. The Ru atoms are located in the center of each octahedron and Mn substitute Ru as doping.

The grand challenge is to understand how complex phenomena emerge from chemical doping. For the RP ruthenates, first-principles calculations suggest that the electron occupation at the Fermi level is determined by the structure of RuO_6 octahedron [160]. Any change of the latter would impact the physical properties of the material [160]. For example, the rotation of RuO6 octahedron is in favor of ferromagnetic (FM) metallic behavior, and tilt distortion, on the other hand, can drive the system into an antiferromagnetic (AFM) insulating ground state [161]. Both rotation and tilt distortions of RuO_6 octahedron can be tuned by non-thermal parameters such as chemical doping, pressure, and strain [159]. For instance, strain generally is firstly relieved by the rotation of octahedra, which seems to saturate at

a certain angle. Therefore, further increased strain drives different lattice distortion in addition to rotation, i.e., the tilt of octahedra. For single-layered Sr_2RuO_4 (n = 1), there is a rotational instability [162], while octahedra in the bulk have no rotation and the crystal structure remains tetragonal at all temperatures. Indeed, such a rotational instability is frozen into a rotational distortion at the surface [32]. For $Sr_3Ru_2O_7$, there is an 8° of rotation in the bulk at 90 K [155, 163]. For $Sr_4Ru_3O_{10}$ ($n = 3$), octahedra on the outer of two layers of each tri-layer are rotated in average by 5.6° but at the inner third layer are rotated 11° in opposite sense [164]. Overall, the $Sr_{n+1}Ru_nO_{3n+1}$ system exhibits a tendency towards octahedral distortion to reduce the strain when n is small, but no evidence for rotation or tilt for the three-dimensional system ($n = \infty$). The phase diagram shown in Fig. 6.1a indicates the electronic and magnetic properties are intimately coupled to the rotation of octahedra in bulk $Sr_3(Ru_{1-x}Mn_x)_2O_7$. Single-crystal X-ray diffraction refinements show that Mn doping on the Ru site in $Sr_3Ru_2O_7$ leads to the shrinkage of unit-cell volume, a continuous shrinkage of the lattice spacing perpendicular the planes, and the reduction of $(Ru/Mn)O_6$ rotation angle (going to zero at $x \sim$ 0.20) [155]. This implies that Mn doping removes strain, while the global structure remains unchanged.

Creating a surface by cleaving a layered material offers a controlled way to tip the balance between spin, charge, and lattice established in the bulk. For example, octahedra on the surface of Sr_2RuO_4 exhibit rotation to relieve the surface strain [159], while there is no rotation in the bulk [32]. A low energy electron diffraction (LEED) study of $Sr_3Ru_2O_7$ reveals an enhanced rotation ($\sim 12°$) of octahedra at the surface accompanied by a 2.5° of tilt at 80 K [163], while octahedra in its bulk display a $\sim 6.7°$ rotation at 300 K and 8.1° at 90 K without tilt [163]. So far, there

is no report for the surface of $Sr_4Ru_3O_{10}$, but there is good reason to expect both rotation and tilt (see later discussion).

In this article, we report the experimental investigation of chemical doping effect on both octahedron and local density of states (LDOS) on the surface of $Sr_3(Ru_{1-x}Mn_x)_2O_7$ single crystals with $x = 0$, 0.06 and 0.16. While the structure of octahedron is determined by low energy electron diffraction (LEED), scanning tunneling microscopy (STM) allows us to identify Mn sites. We find that, in addition to the rotational distortion of octahedron as seen in the bulk, there is tilt distortion at the surface. This indicates that the surface symmetry is reduced to C_{2v} compared to the C_{4v} in the bulk. With STM, we observe, for the first time, the "chirality" of LDOS Mn sites resulting from rotation, but becoming visible by tilt. These results serve as fingerprints of chemical doping at the atomic scale.

6.2 Surface tilt-induced C_{2v} symmetry

Due to their layered structure, $Sr_3(Ru_{1-x}Mn_x)_2O_7$ single crystals are cleaved at the weak bonding between the double layers of octahedral (Fig. 6.1b). Thus, the resultant surface is the Sr-O layer. Fig. 6.2a shows the top view of Sr-O terminated surface with the first sub-surface layer of octahedra which are rotated (represented by arrows) in the bulk. The tetragonal-(1×1) unit is shown by the red square. By taking into account of the rotation of octahedra, the surface unit cell is $(\sqrt{2}\times\sqrt{2})$R45° shown as the black dashed square, which is 5.6 $\mathring{A}$ × 5.6 $\mathring{A}$. There are four Sr atoms on the sides of the surface $(\sqrt{2}\times\sqrt{2})$R45° unit cell, i. e. including two Sr atoms. *These two Sr atoms are identical.* This surface unit cell also contains two octahedral sites: one at the center, and four shared at the corners. The center octahedron has *cw* rotation, while the corner octahedral has *ccw* rotation, as indicated by arrows in Fig. 6.2a. Figure 6.2b shows a STM topographic image

for $x = 0.06$ compounds at a bias of 0.9 V. Two different Sr atoms are imaged in one $\sqrt{2}\times\sqrt{2})$R45° unit cell and there is no feature associated with rotation.

We studied larger field of view of $(\sqrt{2}\times\sqrt{2})$R45° superstructure in Fig. 6.3. The STM topography for x=0.06 shows a larger contrast of $(\sqrt{2}\times\sqrt{2})$R45° resolution than x=0.16 Mn-doped samples. The inset Fourier transform (FT) of the STM images in Fig. 6.3a display the fractional spots (marked with circles) in additional to integer tetragonal-(1×1) unit cell. These fractional spots are associated with the $(\sqrt{2}\times\sqrt{2})$R45° real space unit cell. The low bias (0.6 V) STM image for x = 0.16 (Fig. 6.3b) does not clearly show two different Sr sites, but does show the same fractional spots in the FT-image. This is more evident in the simultaneously taken topo-mapping of dI/dV in Fig. 6.3c, which is proportional to the electronic local density of states. The additional $(\sqrt{2}\times\sqrt{2})$R45° fractional spots are clearer and brighter in the FT-image of Fig. 6.3c. This strongly suggests that the $(\sqrt{2}\times\sqrt{2})$R45° unit cell at the surface of $x = 0.16$ compound is more likely electronic in origin (< 0.8 V). The $(\sqrt{2}\times\sqrt{2})$R45° fractional spots at LEED pattern is due to the surface octahedra rotation but the $(\sqrt{2}\times\sqrt{2})$R45° FT-image is electronic in origin. Indeed, there is no report about possible surface geometric buckling [163] at the surface of both single and double layered ruthenates. Thus, even though the $(\sqrt{2}\times\sqrt{2})$R45° unit cell is consistent with the surface unit cell, these two Sr sites should be electronically equivalent. Actually, the two Ru octahedral sites, apical O sites are all equivalent. It is actually a long-standing puzzle that, with different sample biases, the surface Sr atoms have different contrasts on the surface of Sr_2RuO_4 [32] and $Sr_3Ru_2O_7$ [59, 48]. Here in Fig. 6.3 are the very similar observations in our x=0.06 and x=0.06 Mn-doped $Sr_3Ru_2O_7$ samples. We leave this puzzle for later discussion.

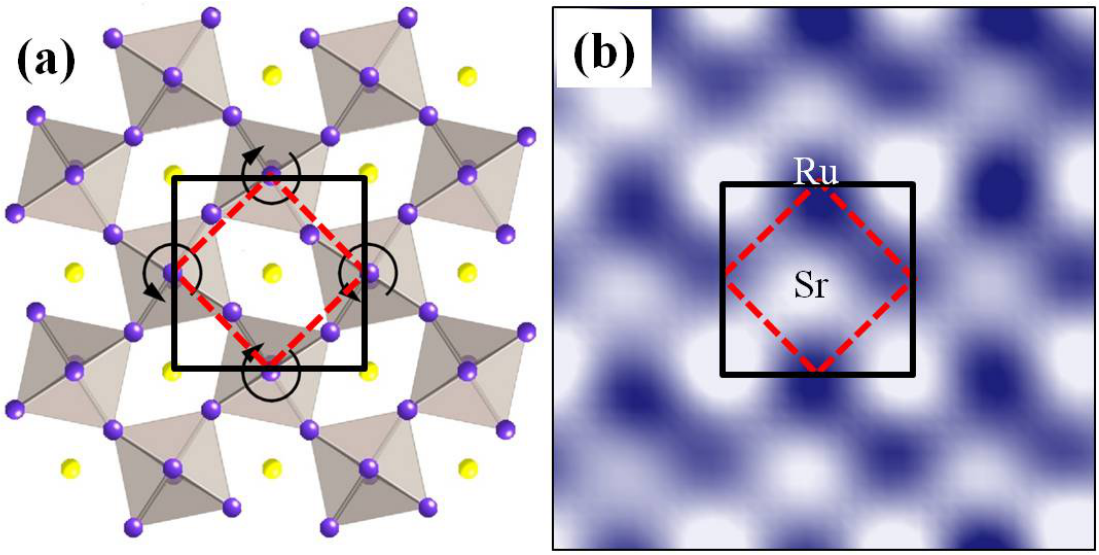

FIGURE 6.2. (a) Top-view from the cleavage plane showing the surface plane and the first sub-surface octahedra layer. The octahedra rotations are enhanced to the eye. The black dashed square shows surface ($\sqrt{2}\times\sqrt{2}$)R45° unit cell compared with bulk truncated tet-(1×1) as the red square unit cell. (b) A STM image from x=0.06 Mn doped $Sr_3Ru_2O_7$ shows $\sqrt{2}\times\sqrt{2}$)R45° and (1×1) unit cell with Sr in high protrusion sites and Ru in low protrusions sites.

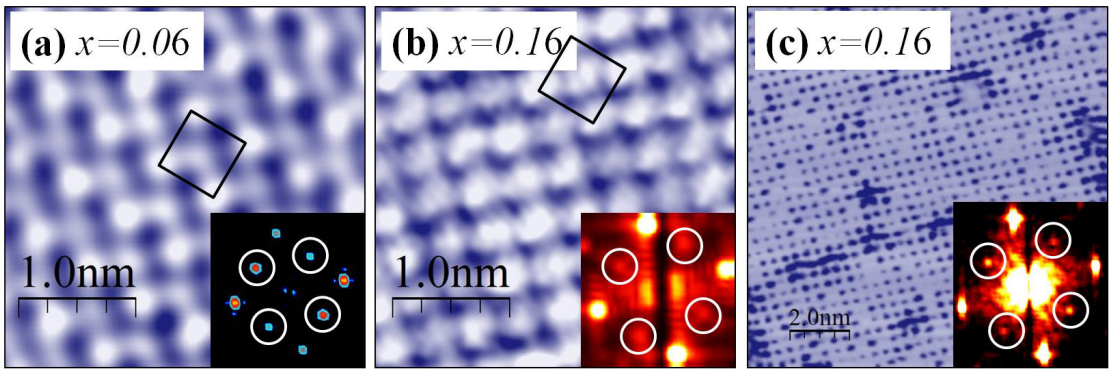

FIGURE 6.3. (a and b) STM and FT-STM images of ($\sqrt{2}\times\sqrt{2}$)R45° superstructure in $Sr_3(Ru_{1-x}Mn_x)_2O_7$ for x = 0.06 in (a) and x = 0.16 in (b). (c) Topo-mapping of dI/dV is taken simultaneously with (b).

If the surface has the same symmetry as the bulk (bulk-truncated), the LEED pattern should look like Fig. 6.4a [32, 163, 21]. Here, circled dots represent pattern expected from tet - (1 × 1) structure, and un-circled dots can only be seen with $(\sqrt{2}\times\sqrt{2})$R45° unit cell. Considering structure factor, some of un-circled spots are missing along the so-called glide lines, which are indicated by dash lines in Fig. 6.4a. This is what was observed on the surface of Sr_2RuO_4 with octahedral rotational distortion [32]. For $Sr_3Ru_2O_7$, the LEED pattern is shown in Fig. 6.4b. Note that there is no glide line, as all missing spots (indicated by arrows) exist. This indicates the symmetry of $Sr_3Ru_2O_7$ surface is broken. According to previous studies [163], such symmetry broken is caused by the additional distortion of RuO_6 octahedra by tilt. The disappearance of two glide lines suggests tilt-induced two domains.

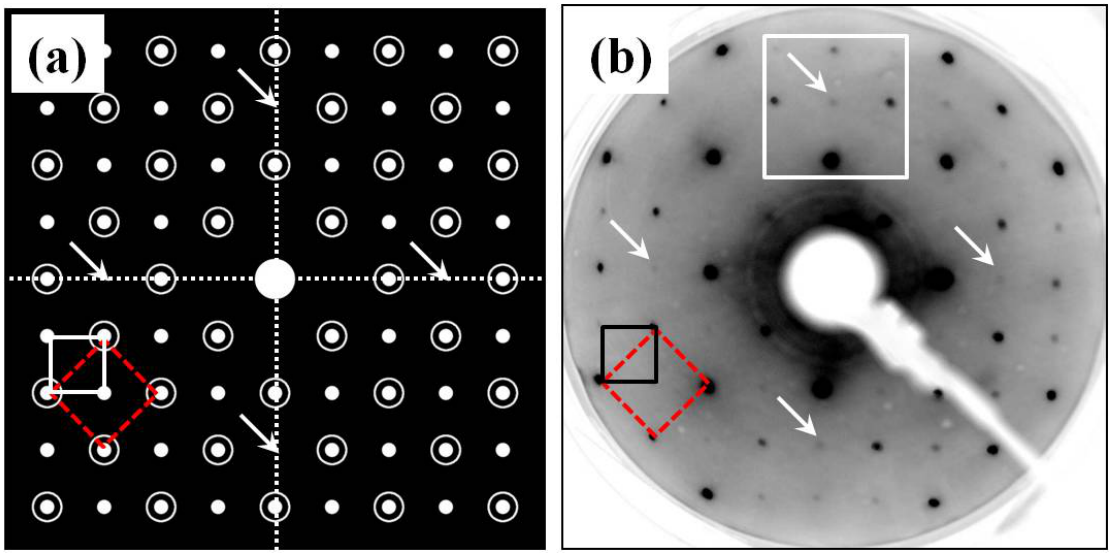

FIGURE 6.4. (a). A schematic view of LEED pattern expect from a rotated octahedral surface without tilt. The (1×1) real space periodicity generates the circled solid dots with a reciprocal unit cell marked in red square. The $(\sqrt{2}\times\sqrt{2})$R45° real space periodicity produces fractional spots (solid dots) as the reciprocal lattice with its unit cell marked in dashed square. Two glides are indicated by white lines along which fractional spots (marked by arrows) are extinct. (b). Experimental image of LEED pattern taken at 87 K at 225 eV for parent $Sr_3Ru_2O_7$.

One can quantify the tilt distortion of octahedra by analyzing the intensity of fractional spots with respect to the integral spots in LEED images. The observed intensity of fractional spots in LEED images shows that the tilt distortion at surface is gradually suppressed with increasing Mn doping, while the rotational distortion remains unchanged. Figure 6.5a shows an enlarged image of LEED pattern marked by the white square in Fig. 6.4b. The diffraction spot in the center is only present when the symmetry is broken by tilt (Fig. 6.5b).

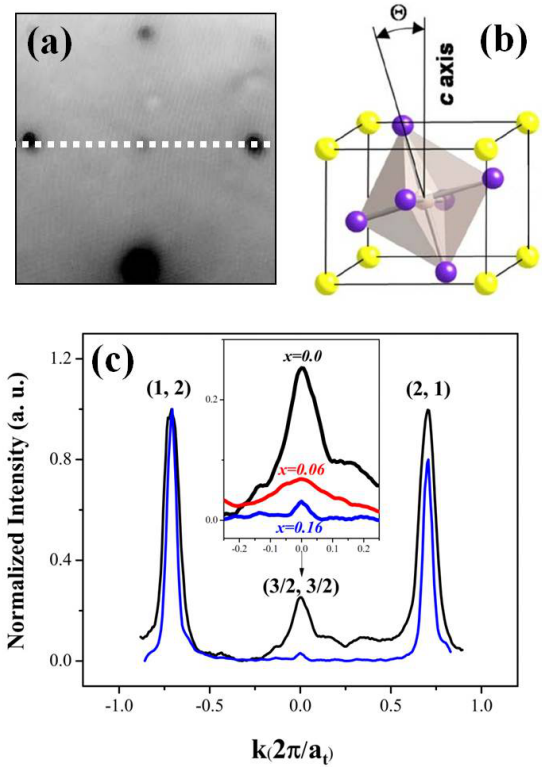

FIGURE 6.5. (a) The zoom-in image of the white square marked in LEED pattern in Fig. 6.4b, there is a clear spot at the center. (b) Schematic view of tilt distortion in the octahedral. (c) Normalized line profile along the dashed line for the x=0.16 Mn-doped sample. The inset shows the doping-dependence of zoom-in normalized line profile.

By normalizing the intensity of the fractional spot at the center with respect to the integral spot (1, 2) along the white dashed line in Fig. 6.5a, the line profiles are obtained for different dopings and plotted in Fig. 6.5c. Note that the intensity of the fractional spot is much weaker than that of integral ones. More remarkably,

the peak intensity of the fractional spot decreases with increasing x. As highlighted in the inset of Fig. 6.5c, it almost vanishes at $x = 0.16$, implying the tilt angle (see Fig. 6.5b) $\theta \rightarrow 0$. When making the same analysis for a fractional spot associated with rotation distortion, we find no evidence for the doping dependence of the surface rotation down to ~ 80 K. This indicates that the rotational distortion on the surface of $Sr_3(Ru_{1-x}Mn_x)_2O_7$ ($0 \leq x \leq 0.16$) remains unchanged. We had previously determined the rotational angle $\sim 12 \pm 3$ ° for $x = 0$ [163], which is greater than its bulk counter part (~ 8.1 at 90 K [163]). The doping independent rotation angle at the surface suggests that it cannot rotate further, thus requiring additional tilt distortion at the surface. The observation of tilt distortion of octahedra indicates that the surface of $Sr_3(Ru_{1-x}Mn_x)_2O_7$ has a C_{2v} symmetry, while its bulk has a C_{4v} symmetry due to the absence of tilt distortion.

With both rotation and tilt distortion, the surface of $Sr_3(Ru_{1-x}Mn_x)_2O_7$ provides a perfect platform to exam the structural distortion induced electronic property change. Fig. 6.6a shows a STM image for $x = 0$ compound. If drawing a $(\sqrt{2}\times\sqrt{2})$R45° unit cell, one may see that there are two different Sr and RuO_6 sites with the latter pointed by yellow arrows. Similar features are seen in $x = 0.06$ compound as depicted in Fig. 6.6b. If there were pure rotational distortion, one would expect a C_{4v} symmetry in STM image with identical Sr sites and RuO_6 sites. The observation of two inequivalent Sr sites and RuO_6 sites in a $(\sqrt{2}\times\sqrt{2})$R45° unit cell indicates a C_{2v} symmetry for $x = 0$ and 0.06. As shown in Fig. 6.6c, the features seen in low-doping compounds no longer exist for $x = 0.16$. This indicates the C_{4v} symmetry, which was seen in Sr_2RuO_4 (Fig. 6.6d), is corresponding to the case of pure rotational distortion. Thus, we believe that the lower symmetry in STM images of $x = 0$ and 0.06 are due to an additional tilt distortion, echoing

the LEED results. Fig. 6.6e illustrates such consequence (two inequivalent Sr and RuO_6 sites), by taking into account of tilt as indicated by red arrows.

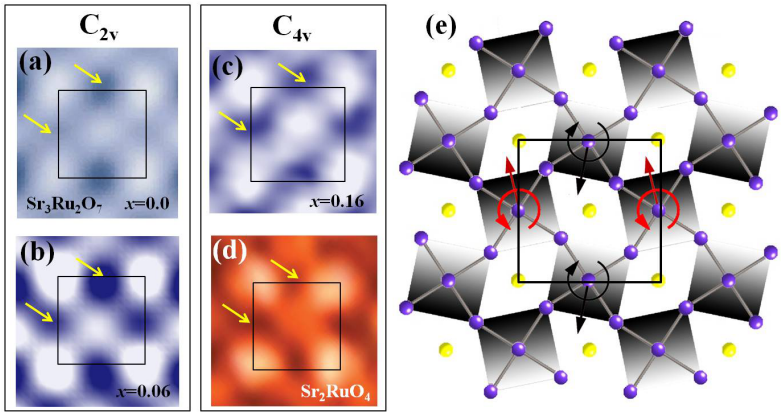

FIGURE 6.6. Zoom-in STM image and its symmetry for (a) Sr_2RuO_4, reproduced from [32]. (b) $Sr_3Ru_2O_7$, reproduced from [48] (c) x=0.06 Mn-doped (d) x=0.16 Mn-doped $Sr_3Ru_2O_7$. The dash square is the $(\sqrt{2}\times\sqrt{2})$R45° unit cell. The arrows are pointing to the left- and right- RuO_6 octahedra sites. When these two sites are different, the image is two-fold symmetry. The schematic model of $\sqrt{2}\times\sqrt{2}$)R45° unit cell with Sr sites at the (e) center and corner and (f) the sides. The yellow solid circles represent Sr atoms and the solid black and blue squares represent the RuO6 octahedra. (e) A schematic view of surface with both RuO_6 octahedra and tilting. The gradient color on RuO_6 indicates the tilt of the plane. Note that now the cw sites are marked with black color and ccw sites with red color.

To conclude, for the $(\sqrt{2}\times\sqrt{2})$R45° superstructure seen in the single and double layered rutheneates and Mn-doped $Sr_3Ru_2O_7$, it is a puzzle that two Sr sites are different. Now two different RuO_6 sites are only seen in parent and x=0.06 Mn-doped $Sr_3Ru_2O_7$. It maybe argued that RuO_6 sites (darker sites) may also forms $(\sqrt{2}\times\sqrt{2})$R45° but it is clear that $(\sqrt{2}\times\sqrt{2})$R45° sublattice of Sr sites and RuO_6 sites are shifted in one direction by half tetragonal lattice constant. This one directional shifting leads to the C_{2v} symmetry. This does not depend on the scenario of explaining two different sites puzzle. The obvious resolution of the broken symmetry is to include tilt, which is shown in Fig. 6.6e where the gradient color indicate how the plane tilts, i. e. the darker means going down and lighter means going up. This symmetry due to the tilt is obviously C_{2v}. As we know, there is no tilt

at the surface of Sr_2RuO_4 [32] and almost diminished tilt (from Fig. 6.5) on the $x = 0.16$ Mn-doped $Sr_3Ru_2O_7$. Thus, it is consistent with their STM topography with C_{4v} symmetry. On the other hand, there is a tilt on the surface of parent and slightly Mn-doped ($x = 0.06$) $Sr_3Ru_2O_7$. Thus their STM topographies show C_{2v} symmetry.

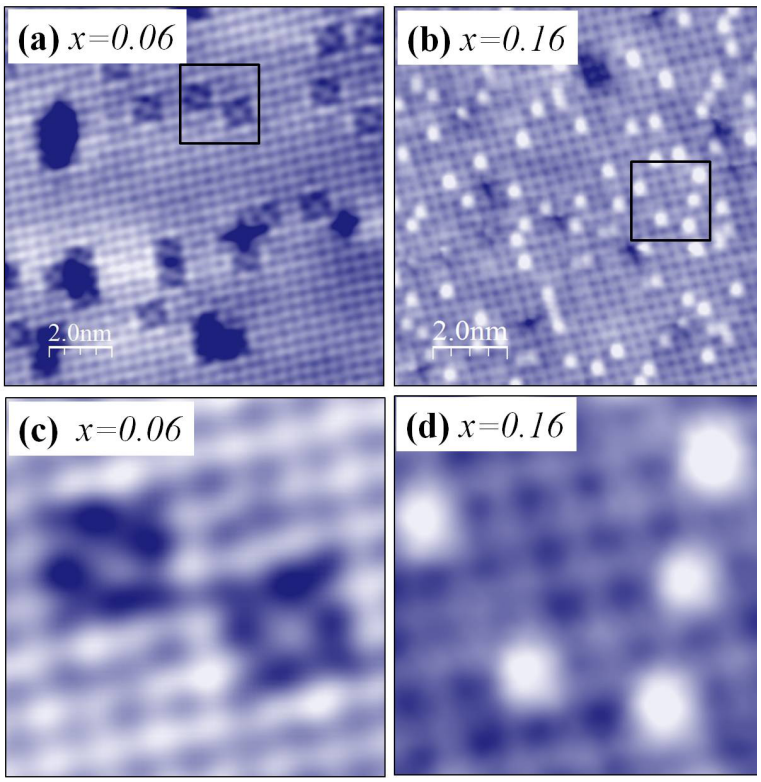

FIGURE 6.7. (a)STM topography of Mn-dopings on the surface of $Sr_3(Ru_{1-x}Mn_x)_2O_7$ for (a) x = 0.06 (bias: 1.2 V, current: 50 pA) and (b)x = 0.16 (Bias: 1.0 V, current 150 pA). Zoom-in STM topographies from black square in (a and b) are shown in (c and d), respectively.

This leads to two different RuO_6 sites. The question is how tilt could explain their difference because tilt, structurally, does not create two different RuO_6 sites. But how about electronically? Obviously, tilt should lead to electronic anisotropy in-plane, namely different electronic transport properties parallel and perpendicular to the tilt plane. It is a simple structure C_{2v} leading to electronic C_{2v} symmetry. Now comparing the surface unit cell presented in STM topographies in

Fig. 6.6(a,b,c,d) with the one in schematic view of tilted surface in Fig. 6.6e, the darker sites correspond to the RuO_6 *cw* sites while the light sites to the *ccw* sites. The closest bright Sr sites to the RuO_6 *cw* sites are in its horizontal direction (parallel to tilt plane). In contrast, the closest bright Sr sites to the RuO_6 *ccw* sites are in its vertical direction (perpendicular to tilt plane). Thus, due to the electronic antitropic of the proximity effect, origin from tilt, the RuO_6 *cw* and *ccw* sites will be electronic different, giving a C_{2v} symmetry.

6.3 Mn-doping dependence of the surface properties

For the doped samples, it is possible to identify Mn doping sites from STM topographical images. Figures 6.7a & 6.7b show STM topographies at $\sim 100\ K$ for $x = 0.06$ and 0.16 compounds using a high bias ≥ 1 V. Note that in a lower bias the STM shows $(\sqrt{2}\times\sqrt{2})$R45° (Fig. 6.2b) but here it shows a (1×1) resolution, indicating the superstructure induces/chnages the local density of states below 1 *V*. In addition to periodic Sr lattices, features associated with Mn dopant are observed: the sub-surface Mn dopant appears as dark squares for $x = 0.06$ (Fig.6.7c), but bright spots for $x = 0.16$ (Fig.6.7b). Since neither of these features is seen at the surface of the parent compound ($x = 0$), and the density of these features scales with the doping level, they cannot be attributed to surface adsorption or contamination. The fact that the images are so different for the two different doping levels implies that their surface local electronic properties are different.

By implying a structure model on the zoom-in STM topographies indicates that there are two sites for the Mn-dopings, *cw* and *ccw* octahedral rotation sites, see Fig. 6.8a and 6.8b. Note that in Fig. 6.8a, the left square button is *cw* site marked with black color and the right square button is *ccw* sites marked with red color. There are two *cw* sites and three *ccw* sites in Fig. 6.8b. All of the *cw* sites of

$(Ru/Mn)O_6$ have the same tilt and ccw sites have the opposite tilt, thus the tilt and rotation are locked in a single domain. One would expect that tilt and rotation can locked in the other way in their twin domain. Fig. 6.8a and 6.8b again proves what we see the square button features and bright spots are MnO_6 sites because of the match of the location.

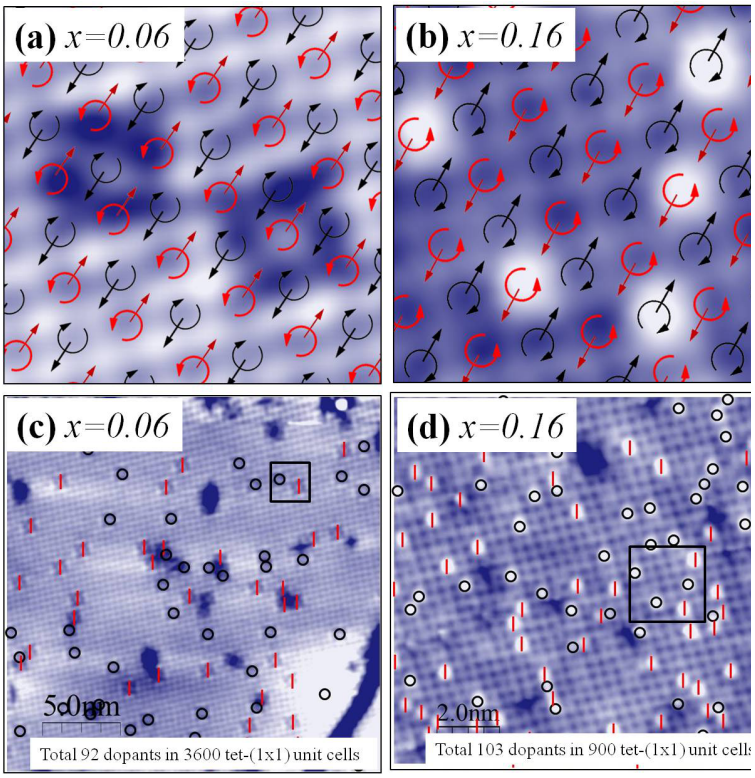

FIGURE 6.8. Applying a schematic structure model in zoom-in STM topography where cw and ccw of Mn sites in (a) x = 0.06 and (b) x = 0.16 Mn-doped $Sr_3Ru_2O_7$. The arrows and circles (same as used in Fig. 6.6) represent tilt and $(Ru/Mn)O_6$ octahedral rotation, respectively. (c & d) Statistic analysis on the two locations (cw vs. ccw) of Mn-dopints on the STM topography for x = 0.06 (c) and x = 0.16 (d) Mn-doped $Sr_3Ru_2O_7$.

Next question would be the interaction between Mn-dopings. An alternative way to ask is whether the *cw* and *ccw* location of the Mn-dopings couples and what their distributions are. Figure 6.8b and 6.8c show the spatial distribution of Mn at the surfaces of $x = 0.06$ and 0.16, respectively. Now the black circles and red bars identify *ccw*- or *cw*-rotated sites in the unit cell, respectively. The

rotational directions in the black square in Fig. 6.8c and 6.8d can be identified in the enlarged image shown in Fig. 6.8a and 6.8b, respectively. Statistical counting of the circles and bars results in almost equal number of *ccw*- and *cw*- sites in each image. Therefore, there is no preferred rotational site for Mn in both $x = 0.06$ and 0.16 compounds. Further, the total number of Mn sites is 2.6% for $x = 0.06$ and 11.4% for $x = 0.16$. Statistically, the variance on the average number (n) of doping sites in an area is ($\sqrt{n}$) assuming that they are randomly distributed. Thus, for a confidence level of 95%, the doping level should fall to $(2.6 \pm 0.6)\%$ for $x = 0.06$ and $(11.4 \pm 2.2)\%$ for $x = 0.16$ from STM images in Fig. 6.8c & 6.8d, respectively. Thus, it appears to smaller number of Mn sites at the surface than in the bulk. An early STM study on 1% Ti doped $Sr_3Ru_2O_7$ showed only $\sim 0.5\%$ sites for the top octahedral layer and $\sim 0.8\%$ sites in the second octahedral layer [59], all less than the bulk doping level 1%. It is not clear why both STM measurements give a less doping level at the surface.

Further statistic analysis shows that the Mn is randomly distributed at the surface without any sign of short range clustering. We counted and histogrammed all Mn-Mn pairs within Fig. 6.8c & 6.8d as function of the Mn-Mn distances, then divided this observed histogram by a histogram of a random model with the same number of doping sites [136]. (The random model was simulated 1000 times to reduce the error.) Such curve obtained is so-called radial distribution ratio (RDR) which is equal to 1 when there is no clustering. Fig. 6.9 shows RDR curves for the statistical results on both $x = 0.06$ & 0.16 and they are all close to 1. It indicates there is no clustering of Mn at both doping levels samples.

The distribution is also random and homogeneous with respect to *ccw*- and *cw*-rotated MnO_6 sites. We studied the dependence of octahedral rotation direction

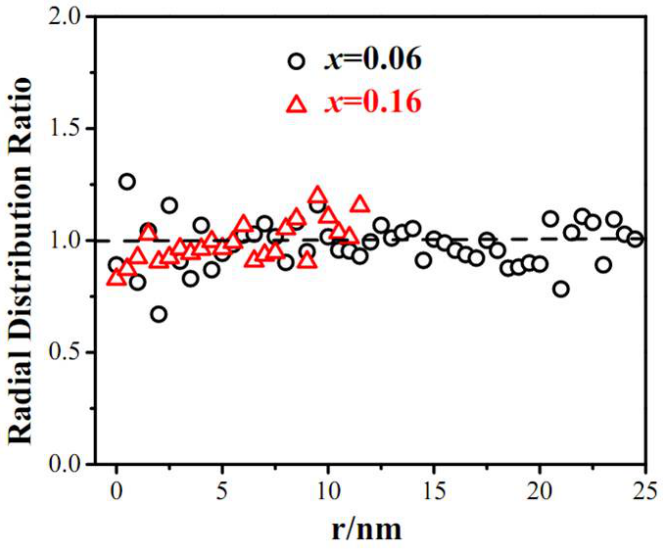

FIGURE 6.9. Radial distribution ratio curves for x = 0.16 (red triangular) Mn doped and x = 0.06 (black circles) $Sr_3Ru_2O_7$ samples.

from one Mn sites to its nearest neighbor. The model we applied is to define the dependence coefficient by

$$\sum_{i=0}^{n} f(M, M^*) / \sum_{i=0}^{n} f(M, M\prime) where f(m1, m2) = (m1 == m2) \qquad (6.1)$$

We used a binary value of 0 or 1 to represent the rotation direction. M is the rotation direction of a typical point, M* is the rotation direction of its nearest neighbor, and M′ is an independent copy of M with the same distributionce [165]. A value 1 suggests the complete lack of dependence where the rotation direction of one Mn dopant is independent of its neighbors. This dependence coefficient obtained from our data on $x = 0.06$ and 0.16 compounds are all ~ 0.92, thus the location of a *ccw*-rotated sites does not correlate with *cw*-rotated sites. The slightly smaller of RDR than 1 may due to the finite size of the field of view. Thus, the Mn-dopings in $Sr_3(Ru_{1-x}Mn_x)_2O_7$ is quite homogenous in nanoscale. However, the less doping at the surface compared to bulk indicates that in a larger scale, probably in macroscopic view, the doping is inhomogeneous.

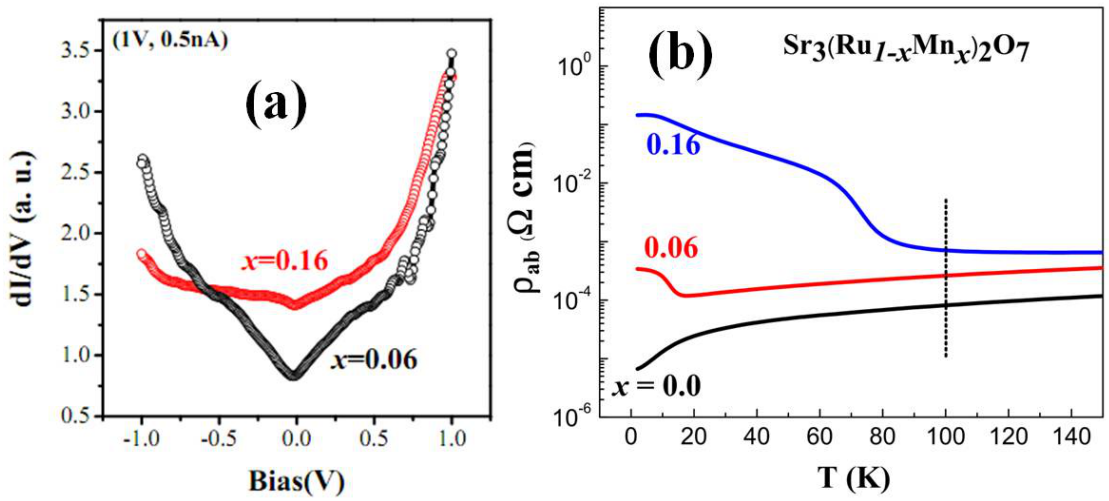

FIGURE 6.10. (a) STS measured from the the surface of x = 0.06, 0.16 Mn-doped $Sr_3Ru_2O_7$ (b) Bulk transport measurement of in-plane resistivity for parent and x = 0.06, 0.16 Mn-doped $Sr_3Ru_2O_7$ samples.

This will have profound effect on measuring the bulk properties because of possible phase separation [167]. A local surface measurement maybe more accurately represents the electronic properties due to the Mn doping. Thus, STS measurement was done at the surface of both $x = 0.06$ and 0.16 Mn-doped $Sr_3Ru_2O_7$ samples, see Fig. 6.10a. Both STS curves are measured with the same tunneling junction of (bias: 1 V, current: 0.5 nA). There are no clear features but one would see a better conductivity in $x = 0.16$ sample because of the higher local density of states near the Fermi level. This is surprising because the bulk shows the opposite. Fig. 6.10b shows the bulk transport properties for parent and $x = 0.06$ and 0.16 Mn-doped $Sr_3(Ru_2O_7$ samples. There are several possible reasons for this difference of the surface and the bulk. One scenario would be that the surface is reconstructed with tilt and possible larger rotation thus leads to the conductivity properties reversed. The other one would be the possible phase separation [155, 167] which the interpretation of the transport properties in the bulk should take into account of. We think both need to be considered to fully understand their difference.

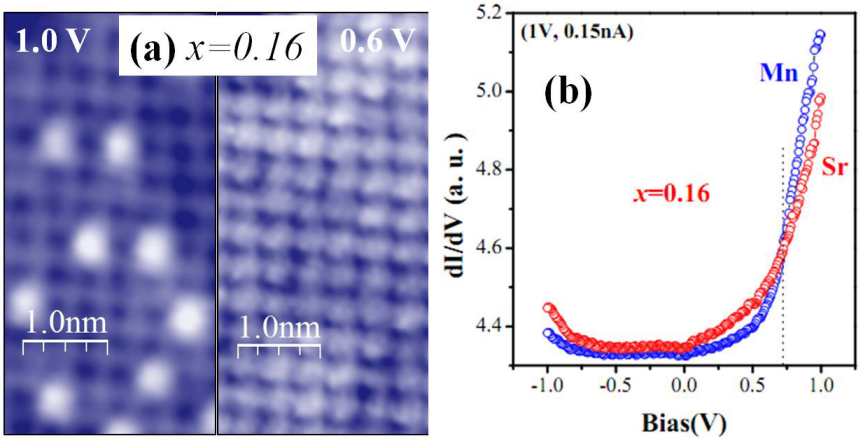

FIGURE 6.11. (a) Bias-dependent STM topography for x = 0.16 Mn-doped $Sr_3Ru_2O_7$. Left image is taken at bias 1.0 V while the right one at 0.6 V. (b) Comparison of STS measured from MnO_6 site and Sr site.

Since the Mn-doping sites in our field of view are homogeneously distributed, we can focus on the electronic property of individual MnO_6 which may represents all of other Mn dopings in Fig. 6.11. First, bias-dependent STM topographies at the same location of surface of $x = 0.16$ Mn-doped $Sr_3Ru_2O_7$ clearly show two very different appearance of Mn-dopings: one shows bright spots at 1.0 V and the other one shows these bright spots disappear at 0.6 V. It indicates the features of the bright spots are dominated by electronic rather than geometric contribution. Note that the Mn-dopings are actually one layer below the top Sr-O lattice. The STS shown in Fig. 6.11b shows that the density of states for Mn-doping site is higher than Sr-sites from bias at around 0.75 V. Thus, it explains that the Mn-doping site is visible at bias higher than 0.75 V in the STM topography in the left panel of Fig. 6.11a but invisible below 0.75 V at the right panel. A theoretical calculation is needed to understand which band contributes to the change on the local density of states on the dopings.

Last, we would like to point out that the square-button like features, which are due to the doping of Mn, shows a chirality shape, see Fig. 6.12. The red and yellow bars placed where two darker sites connected. The red bars on the *cw*-sites form

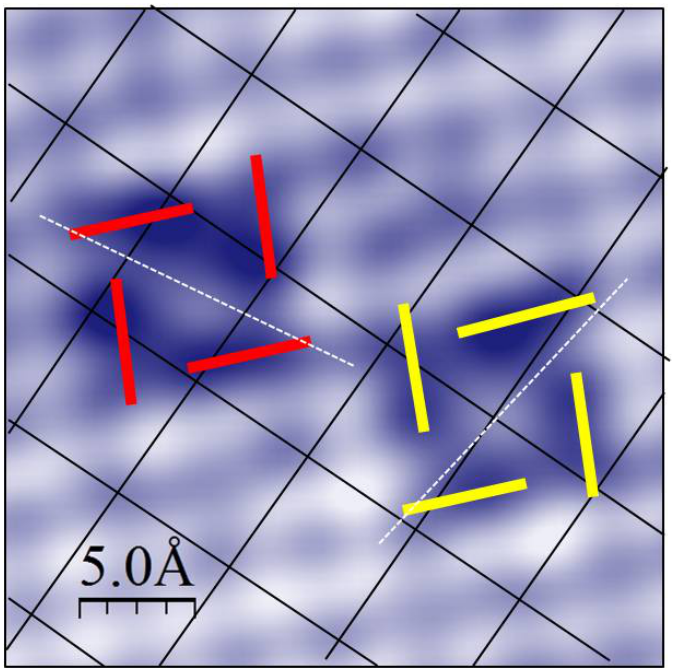

FIGURE 6.12. Left- and right-hand chirality of MnO_6 octahedra. Additional red and yellow bars are guiding the eyes to see the structural chirality. The rotation angle was estimated from the dashed white lines.

a shape of left-hand chirality, is consistent with the *cw* rotation. The yellow bars on the *ccw*-sites form a shape of right-hand chirality, is also consistent with the *ccw* rotation. There is no observable difference of the intensity at the center of the Mn-dopings even though one is associated with a depressed local density of states (see Fig. 6.6e). However, the shape of the center do offer a way to approximately estimate the rotation angle. The measured rotation angle from the rotated shape of the button center is $\sim (9\ ^\circ \pm 3^\circ)$, which is close to that obtained from the bulk ($\sim 8^\circ$ at 90 K). However, this does not imply the rotation of MnO_6 octahedra. Rather, it should reflect the consequence of rotation of nearest RuO_6 octahedra, as demonstrated in Fig. 6.6e. Unfortunately, other STM data for $x = 0.16$ does not allow us to determine the magnitude of rotation. A qualitative analysis of LEED intensity verse voltage (I-V) curves are needed in order to know the rotation angles at the surface.

In summary, the surface of Mn-doped $Sr_3Ru_2O_7$ exhibits both a tilt and rotation of the octahedral, with the tilt at the surface diminishes as Mn doping increases. We examined the bias dependence of the symmetry of the STM images and FFT, and argued that the observed C_{2v} symmetry observed at the surface of double layered ruthernate is related to surface tilt. The chirality of the Mn-dopants has been identified and statistic analysis indicates they are randomly distributed. This is a homogenous system in microscopic but it might be inhomogeneous in macroscopic. Spectroscopy measured at the MnO_6 and Sr sites are consistent with the bias-dependent STM topography. The surface of higher ($x = 0.16$) Mn-doping $Sr_3Ru_2O_7$ has a better conductivity than the lower one (($x = 0.06$)), reflecting the spatial resolved electronic properties affected by the Mn-dopings.

References

[1] P. J. Ford, The Rise of the Superconductors. CRC Press, (2005).

[2] Y. Kamihara, T. Watanabe, M. Hirano, and H. Hosono, J. Am. Chem. Soc. **130**, 3296 (2008).

[3] Elbio Dagotto, Takashi Hotta, and A. Moreo, Physics Reports **344**, 1 (2001).

[4] Q. Si and F. Steglich, Science **329**, 1161 (2010).

[5] Y. maeno, H. Hashimoto, K. Yoshida, S. Nishizaki, T. Fujita, J. G. Bednorz, and F. Lichtenberg, Nature **372**, 532 (1994).

[6] S. A. Grigera, et al., Science **294**, 329 (2001).

[7] A. Kreyssig, et al., Physical Review B **78**, 184517 (2008).

[8] M. S. Torikachvili, S. L. Bud'ko, N. Ni, and P. C. Canfield, Physical Review Letters **101**, 057006 (2008).

[9] E. Dagotto, Science **309**, 257 (2005).

[10] J. C. Chapman Ph.D thesis (2005)

[11] S. Nakatsuji and Y. Maeno, Physical Review Letters **84**, 2666 (2000).

[12] S. Nakatsuji, V. Dobrosavljevi, D. Tanaskovi, M. Minakata, H. Fukazawa, and Y. Maeno, Physical Review Letters **93**, 146401 (2004).

[13] O. Friedt, M. Braden, G. Andr, P. Adelmann, S. Nakatsuji, and Y. Maeno, Physical Review B **63**, 174432 (2001).

[14] S. C. Wang, et al., Physical Review Letters **93**, 177007 (2004).

[15] A. Schilling, M. Cantoni, J. D. Guo and H. R. Ott, Nature **363**, 56-58 (1993)

[16] G. Cao, C. S. Alexander, S. McCall, J. E. Crow, and R. P. Guertin, Materials Science and Engineering B **63**, 76 (1999).

[17] D. Kalkstein and P. Soven, Surface Science, **26**, 85(1971).

[18] R. haydock and M. J. Kelly, Surface Science **38**, 139 (1973).

[19] D. Mills, Physical Review B **3**, 3887 (1971).

[20] J. M. Carpinelli, H. H. Weitering, E. W. Plummer, and R. Stumpf, Nature **381**, 398 (1996).

[21] R. G. Moore, J. Zhang, V. B. Nascimento, R. Jin, J. Guo, G. T. Wang, Z. Fang, D. Mandrus, and E. W. Plummer, Science **318**, 615 (2007).

[22] S. Nandi, et al., Physical Review Letters **104**, 057006 (2010).

[23] M. G. Kim, et al., Physical Review B **83**, 134522 (2011).

[24] A. I. Goldman, et al., Physical Review B **78**, 100506R (2008).

[25] A. Jesche, et al., Physical Review B **78**, 180504 (2008).

[26] S. D. Wilson, Z. Yamani, C. R. Rotundu, B. Freelon, E. Bourret-Courchesne, and R. J. Birgeneau, Physical Review B **79**, 184519 (2009).

[27] T. Egami, B. V. Fine, D. Parshall, A. Subedi, and D. J. Singh, Adv. Cond. Matt. Phys. **2010**, 164916 (2010).

[28] J. Teng, C. Chen, Y. Xiong, J. Zhang, R. Jin, and E. W. Plummer, Proceedings of the National Academy of Sciences of the United States of America **110**, 898 (2013).

[29] . Fischer, M. Kugler, I. Maggio-Aprile, C. Berthod, and C. Renner, Reviews of Modern Physics **79**, 353 (2007).

[30] A. Damascelli, Z. Hussain, and Z.-X. Shen, Reviews of Modern Physics **75**, 473 (2003).

[31] H. Ibach and D. L. Mills, Electron Energy Loss Spectroscopy and Surface Vibration, (1982).

[32] R. Matzdorf, Z. Fang, Ismail, J. Zhang, T. Kimura, Y. Tokura, K. Terakura, and E. W. Plummer, Science **289**, 746 (2000).

[33] M. Braden et al., Physical Review B **57**, 1236 (1998).

[34] C. Lupien, S. K. Dutta, B. I. Barker, Y. Maeno, and J. C. Davis1, ArXiv 0503317v1 (2008).

[35] R. Moore, Ph.D thesis, The University of Tennessee at Knoxiville, (2007)

[36] F. Wang and D.-H. Lee, Science **332**, 200 (2011).

[37] J. Paglione and R. L. Greene, Nature Physics **6**, 645 (2010).

[38] A. Cho, Science **320**, 870 (2008).

[39] D. C. Johnston, Advances in Physics **59**, 803 (2010).

[40] A. S. Sefat, R. Jin, M. A. McGuire, B. C. Sales, D. J. Singh, and D. Mandrus, Physical Review Letters **101**, 117004 (2008).

[41] M. Rotter, M. Tegel, and D. Johrendt, Physical Review Letters **101**, 107006 (2008).

[42] D. N. Basov and A. V. Chubukov, Nature Physics **7** (2011).

[43] Q. Huang, Y. Qiu, W. Bao, M. A. Green, J. W. Lynn, Y. C. Gasparovic, T. Wu, G. Wu, and X. H. Chen, Physical Review Letters **101**, 257003 (2008).

[44] T. Shimojima, et al., Physical Review Letters **104**, 057002 (2010).

[45] A. Mourachkine, High Temperature Superconductivity in Cuprates (Springer, 2002).

[46] R. A. Borzi, S. A. Grigera, J. Farrell, R. S. Perry, S. J. S. Lister, S. L. Lee, D. A. Tennant, Y. Maeno, and A. P. Mackenzie, Science **315**, 214 (2007).

[47] R. S. Perry, et al., Physical Review Letters **86**, 2661 (2001).

[48] K. Iwaya, et al., Physical Review Letters **99**, 057208 (2007).

[49] M. Imada, A. Fujimori, and Y. Tokura, Reviews of Modern Physics 70, 1039 (1998).

[50] K. Ishida, H. Mukuda, Y. Kitaoka, K. Asayama, Z. Q. Mao, Y. Mori, and Y. Maeno, Nature **396**, 658 (1998).

[51] F. S. Bergeret, A. F. Volkov, and K. B. Efetov, Reviews of Modern Physics **77**, 1321 (2005).

[52] T. Kimura, Y. Tomioka, H. Kuwahara, A. Asamitsu, M. Tamura, and Y. Tokura, Science **274**, 1698 (1996).

[53] G. Binnig and H. Rohrer, Surface Science **126** (1983) 236-244.

[54] G. Binnig and H. Rohrer. Reviews of Modern Physics, **71**:S324S330, 1999.

[55] F. Ancilotto, A. Selloni, and a. R. Car, Physical Review Letters **71**, 3685 (1993).

[56] J. A. Stroscio, R. M. Feenstra, and a. A. P. Fein, Physical Review Letters **57**, 2579 (1986).

[57] A. N. Pasupathy, et al., Science **320**, 196 (2008).

[58] P. A. Colin V. Parker, Eduardo H. da Silva Neto, Aakash Pushp,Shimpei Ono, Jinsheng Wen, Zhijun Xu, Genda Gu and Ali Yazdani, Nature **468** (2010).

[59] J. Lee, M. P. Allan, M. A. Wang, J. Farrell, S. A. Grigera, F. Baumberger, J. C. Davis, and A. P. Mackenzie, Nature Physics **5**, 800 (2009).

[60] J. E. Hoffman, K. McElroy, D.-H. Lee, K. M. Lang, H. Eisaki, S.Uchida, and J. C. Davis, Science **297**, 1148 (2002).

[61] P. Aynajian, E. H. da Silva Neto, A. Gyenis, R. E. Baumbach, J. D. Thompson, Z. Fisk, E. D. Bauer, and A. Yazdani, Nature **486**, 201 (2012).

[62] P. Roushan, et al., Nature **460**, 1106 (2009).

[63] M. P. Allan, et al., Science **336**, 563 (2012).

[64] T. M. Chuang, M. P. Allan, J. Lee, Y. Xie, N. Ni, S. L. Bud'ko, G. S. Boebinger, P. C. Canfield, and J. C. Davis, Science **327**, 181 (2010).

[65] P. T. Sprunger, L. Petersen, E. W. Plummer, E. Laegsgaard, and F. Besenbacher, Science **275**, 1764 (1997).

[66] S. H. Pan, E. W. Hudson, and J. C. Davis, Rev. Sci. Instrum **70**, 1459 (1999).

[67] B. C. Stipe, M. A. Rezaei, and W. Ho, Rev. Sci. Instrum 70, 137 (1999).

[68] M. E. Maximilian Assig, Axel Enders, Wolfgang Stiepany, Christian R. Ast et al., Rev. Sci. Instrum **80** (2013).

[69] S. Y. Tong, Process in surface science **7**, 1 (1975).

[70] M. A. V. Hove, W. H. Weinberg, and C.-M. Chn., Low-Energy Electron Diffraction (Springer, Verlag Berlin Heidelberg New York London Paris Tokyo, 1986).

[71] M. Henzler and W. Gpel, Oberflchenphysik des Festkrpers, Teubner, Stuttgart, (1991).

[72] P. J. Rous, J. B. Pendry, D. K. Saldin, K. Heinz, K. Mller, and N. Bickel, Physical Review Letters **57**, 2951 (1986).

[73] J. B. Pendry, Journal of Physics C: Solid State Physics **13**, 937 (1980).

[74] A. Barbieri and M. A. V. Hove (private communication).

[75] J. Rundgren, Physical Review B 68, 125405 (2003).

[76] A. Zangwill, Physics at Surfaces (Cambridge University Press, Cambridge, 1988).

[77] The major work of nanoscale chemical phase separation in $FeTe_0.55Se_0.45$ is done by Xiaobo He. The LEED experiments and I-V analysis were done by Guorong Li, as well as the liquid helium temperature STM experiments.

[78] X. He, G. Li, J. Zhang, A. B. Karki, R. Jin, B. C. Sales, A. S. Sefat, M. A. McGuire, D. Mandrus and E. W. Plummer, Physical Review B **83**, 220502R (2011).

[79] F. C. Hsu et al, Proceedings of the National Academy of Sciences of the United States of America **105**, 14262 (2008).

[80] Y. Kawasaki, K. Deguchi, S. Demura, T. Watanabe, H. Okazaki, T. Ozaki, T. Yamaguchi, H. Takeya, and Y. Takano, Solid State Communications **152**, 1135 (2012).

[81] W. Bao, Y. Qiu, Q. Huang, M. A. Green, P. Zajdel, M. R. Fitzsimmons, M. Zhernenkov, S. Chang, M. Fang, B. Qian, E. K. Vehstedt, J. Yang, H. M. Pham, L. Spinu, and Z. Q. Mao, Phys. Rev. Lett **102**, 247001 (2009).

[82] S. Li, et al., Physical Review B **79**, 054503 (2009).

[83] A. V. Balatsky and D. Parker, Physics **2**, 59 (2009).

[84] T. J. Liu et al, Nature Materials **9**, 718 (2010).

[85] N. Ni, M. E. Tillman, J.-Q. Yan, A. Kracher, S. T. Hannahs, S. L. Bud'ko, and P. C. Canfield, Phys. Rev. B **78**, 214515 (2008).

[86] C. Dong, H. Wang, Z. Li, J. Chen, H. Q. Yuan, and M. Fang, Physical Review B **84**, 224506 (2011).

[87] B. C. Sales, A. S. Sefat, M. A. McGuire, R. Y. Jin, and D. Mandrus, Physical Review B **79**, 094521 (2009).

[88] H. A. Mook et al, Physiscal Review Letters **104**, 187002 (2010).

[89] F. Massee, S. de Jong, Y. Huang, J. Kaas, E. van Heumen, J. B. Goedkoop, and M. S. Golden, Phys. Rev. B **80**, 140507 (2009).

[90] T. Kato, Y. Mizuguchi, H. Nakamura, T. Machida, H. Sakata, and Y. Takano, Phys. Rev. B **80**, 180507(R) (2009).

[91] T. Hanaguri, S. Niitaka, K. Kuroki, and H. Takagi, Science **328**, 474 (2010).

[92] L. Zhang, D. J. Singh, and M. H. Du, Physical Review B **79**, 012506 (2009).

[93] Z. Q. Zou, Z. C. Dong, A. S. Trifonov, and H. Nejo, J. Vac. Sci. Technol. B **20**, 1567 (2002).

[94] I. Horcas, R. Fernandez, J. M. Gomez-Rodriguez, J. Colchero, J. Gomez-Herrero, and A. M. Baro, Rev. Sci. Instrum. **78**, 013705 (2007).

[95] B. Joseph, A. Iadecola, A. Puri, L. Simonelli, Y. Mizuguchi, Y. Takano, and N. L. Saini, Phys. Rev. B **82**, 020502(R) (2010).

[96] M. Tegel, C. Lohnert, and D. Johrendt, Solid State Commun. **150**, 383 (2010).

[97] D. Louca et al, Physical Review B **81**, 134524 (2010).

[98] M. Rotter, M. Tegel, D. Johrendt, I. Schellenberg, W. Hermes, and R. Pttgen, Physical Review B 78, 020503 (2008).

[99] L. Harnagea, et al., Physical Review B **83**, 094523 (2011).

[100] E. Colombier, S. L. Bud'ko, N. Ni, and P. C. Canfield, Physical Review B **79**, 224518 (2009).

[101] J. Zhao, et al., Nature Materials **7**, 953-959 (2008).

[102] Y. Kawasaki et al, Solid State Communications **152**, 1135 (2012).

[103] S. Avci, et al., Physical Review B 85, 184507 (2012).

[104] D. Pratt, et al., Physical Review Letters 103 (2009).

[105] E. Wiesenmayer, H. Luetkens, G. Pascua, R. Khasanov, A. Amato, H. Potts, B. Banusch, H.-H. Klauss, and D. Johrendt, Physical Review Letters **107**, 237001 (2011).

[106] Z. Li, R. Zhou, Y. Liu, D. L. Sun, J. Yang, C. T. Lin, and G.-q. Zheng, Physical Review B **86**, 180501 (2012).

[107] E. W. Plummer, Ismail, R. Matzdorf, A. V. Melechko, J. P. Pierce, and J. Zhang, Surface Science **500**, 1 (2002).

[108] S. Pan, APS bulletin (Dallas, Texes) (2011).

[109] G. Li, X. He, J. Zhang, R. Jin, A. S. Sefat, M. A. McGuire, D. G. Mandrus, B. C. Sales, and E. W. Plummer, Physical Review B **86**, 060512R (2012).

[110] S. Pan, et al., APS bulletin (Portland, Oregon) (2010).

[111] P. Cai, C. Ye, W. Ruan, X. Zhou, A. Wang, M. Zhang, X. Chen, and Y. Wang, Physical Review B 85, 094512 (2012).

[112] P. Cai, X. Zhou, W. Ruan, A. Wang, X. Chen, D.-H. Lee, and Y. Wang, APS bulletin (2013).

[113] M. C. Boyer, Kamalesh Chatterjee, W. D. Wise, G. F. Chen, J. L. Luo, N. L. Wang, and E. W. Hudson, ArXiv 0806.4400 (2008).

[114] F. C. Niestemski, V. B. Nascimento, B. Hu, W. Plummer, J. Gillett, S. Sebastian, Z. Q. Wang, V. Madhavan, ArXiv:0906.2761.

[115] Y. Yin, M. Zech, T. L. Williams, X. F. Wang, G. Wu, X. H. Chen, and J. E. Hoffman, Phys. Rev. Lett. **102**, 097002 (2009).

[116] H. Zhang, J. Dai, Y. Zhang, D. Qu, H. Ji, G. Wu, X. F. Wang, X. H. Chen, B. Wang, C. Zeng, J. Yang and J. G. Hou, Phys. Rev. B **81**, 104520 (2010).

[117] V. B. Nascimento, A. Li, D. R. Jayasundara, Y. Xuan, J. O. Neal, S. H. Pan, T. Y. Chien, B. Hu, X. B. He, G. Li, A. S. Sefat, M. A. McGuire, B. C. Sales, D. Mandrus, M. H. Pan, J. Zhang, R. Jin, and E. W. Plummer, Phys. Rev. Lett. **103**, 076104 (2009).

[118] J. E. Hoffman, Rep. Prog. Phys. **74** 124513 (2011).

[119] E. van Heumen, et al., Physical Review Letters **106**, 027002 (2011).

[120] F. Ronning, T. Klimczuk, E. D. Bauer, H. Volz, and J. D. Thompson, Journal of physics. Condensed matter : an Institute of Physics journal 20 (2008).

[121] M. Gao, F. Ma, Z. -Y. Lu, and T. Xiang, Phys. Rev. B **81**, 193409 (2010).

[122] G. Kresse and J. Furthmller, Computational Materials Science **6**, 15 (1996).

[123] G. Kresse and J. Furthmller, Physical Review B **54**, 11169 (1996).

[124] J. P. Perdew, K. Burke, and M. Ernzerhof, Physical Review Letters **77**, 3865 (1996).

[125] P. E. Blchl, Physical Review B **50**, 17953 (1994).

[126] H. J. Monkhorst and J. D. Pack, Physical Review B **13**, 5188 (1976).

[127] T. Yildirim, Physical Review Letters **102**, 037003 (2009).

[128] T. Yildirim, Physical Review Letters **101**, 057010 (2008).

[129] K. Proke, S. Mat'a, L. Harnagea, S. Singh, S. Wurmehl, D. N. Argyriou, and B. Bchner, Physical Review B **83**, 104414 (2011).

[130] H. Yao-Bo, et al., Chinese Physics Letters **30**, 017402 (2013).

[131] R. M. Fernandes and J. Schmalian, Physical Review B **82**, 014521 (2010).

[132] H. Luo, et al., Physical Review Letters **108**, 247002 (2012).

[133] M. A. Tanatar, et al., Physical Review B **81**, 184508 (2010).

[134] I. R. Fisher, L. Degiorgi, and Z. X. Shen, Reports on Progress in Physics **74**, 124506 (2011).

[135] M. Rahlenbeck, G. L. Sun, D. L. Sun, C. T. Lin, B. Keimer, and C. Ulrich, Physical Review B **80**, 064509 (2009).

[136] Ilija Zeljkovic, Dennis Huang, Can-Li Song, Bing Lv, Ching-Wu Chu, and J. E. Hoffman, ArXiv 1301.4942v1 (2013).

[137] C.-L. Song, et al., ArXiv:1212.5164 (2013).

[138] Shuheng Pan et al, APS bullentin, Baltimore,(2013).

[139] P. W. Tasker, Journal of Physics C: Solid State Physics **12**, 4977 (1979).

[140] J. Kaas, Master thesis, University of Amsterdam, (2010).

[141] G. Profeta, C. Franchini, K. A. I. L. W. Gamalath, and A. Continenza, Physical Review B 82 (2010).

[142] F. Massee, Ph.D thesis, University of Amsterdam, 2011.

[143] R. Jin, M. H. Pan, X. B. He, G. Li, D. Li, R. -W. Peng, J. R. Thompson, B. C. Sales, A. S. Sefat, M. A. McGuire, D. Mandrus, J. F. Wendelken, V. Keppens and E. W. Plummer, Supercond. Sci. Technol. **23**, 054005 (2010).

[144] S. A. J. Kimber , D. N. Argyriou, and I. I. Mazin, ArXiv: 1005.1761v1.

[145] R. Feynman, R. Leighton, and M. Sands, The Feynman Lectures on Physics. Vol. 1, Chaper. 52 (2011).

[146] They refer their observation to C_2 symmetry but actually it is C_{2v}. M. Yi, D. Lu, J. Chu, J. G. Analytis, A. P. Sorini, A. F. Kemper, B. Moritza, S. Mo, R. G. Moore, M. Hashimoto, W. Lee, Z. Hussain, T. P. Devereaux, I. R. Fisher, and Z. X. Shen, Proc. Natl. Acad. Sci **108**, 6878 (2011).

[147] Q. Wang, Z. Sun, E. Rotenberg, F. Ronning, E. D. Bauer, H. Lin, R. S. Markiewicz, M. Lindroos, B. Barbiellini, A. Bansil, D. S. Dessau

[148] C. Ederer and N. A. Spaldin, Phys. Rev. B **76**, 214404 (2007).

[149] I. I. Mazin and M. D. Johannes, Nat. Phys. **5**, 141 (2009).

[150] Z. P. Yin and W. E. Pickett, Phys. Rev. B **80**, 144522 (2009).

[151] X. Zhou, C. Ye, P. Cai, X. Wang, X. Chen, and Y. Wang, Phys. Rev. Lett. **106** 087001(2011).

[152] C.-L. Song, et al., Science **332**, 1410 (2011).

[153] O. Friedt, M. Braden, G. Andr, P. Adelmann, S. Nakatsuji, and Y. Maeno, Physical Review B **63**, 174432 (2001).

[154] R. Mathieu, et al., Physical Review B **72**, 092404 (2005).

[155] B. Hu, G. T. McCandless, V. O. Garlea, S. Stadler, Y. Xiong, J. Y. Chan, E. W. Plummer, and R. Jin, Physical Review B **84**, 174411 (2011).

[156] J. Hooper, et al., Physical Review B **75**, 060403 (2007).

[157] P. Steffens, J. Farrell, S. Price, A. P. Mackenzie, Y. Sidis, K. Schmalzl, and M. Braden, Physical Review B **79**, 054422 (2009).

[158] M. A. Hossain, et al., Physical Review Letters **101**, 016404 (2008).

[159] Q. Huang, J. W. Lynn, R. W. Erwin, J. Jarupatrakorn, and R. J. Cava, Physical Review B **58**, 8515 (1998).

[160] Z. Fang, N. Nagaosa, and K. Terakura, Physical Review B **69**, 045116 (2004).

[161] Z. Fang and K. Terakura, Physical Review B **64**, 020509 (2001).

[162] M. Braden, Y. Sidis, P. Bourges, P. Pfeuty, J. Kulda, Z. Mao, and Y. Maeno, Physical Review B **66**, 064522 (2002).

[163] B. Hu, G. T. McCandless, M. Menard, V. B. Nascimento, J. Y. Chan, E. W. Plummer, and R. Jin, Physical Review B **81**, 184104 (2010).

[164] M. K. Crawford, R. L. Harlow, W. Marshall, Z. Li, G. Cao, R. L. Lindstrom, Q. Huang, and J. W. Lynn, Physical Review B **65**, 214412 (2002).

[165] R: A language and environment for statistical computing. (R Foundation for Statistical Computing, Vienna, Austria., 2008).

[166] R. Matzdorf (private communication).

[167] T.-H. Kim, M. Angst, B. Hu, R. Jin, X.-G. Zhang, J. F. Wendelken, E. W. Plummer, and A.-P. Li, Proceedings of the National Academy of Sciences **107**, 5272 (2010).

Appendix A: Calibration of thermal drift in STM images

STM scanner can move with sub-angstrom steps both in x-axis and y-axis in cartesian coordinates. People use piezoelectric effect to drive the sub-angstrom movements of scanner by applying electrical field. Nowadays, many STM experiments are done at low temperature and the system needs to be extremely stable to avoid thermal drift whose presence distorts the STM image. Because we measure the parameters of surface lattice structure from STM images, it is important to take out the thermal drift to achieve an accurate measurement if necessary.

This appendix provides a simple way to take out the thermal drift of STM image under certain conditions. First of all, we define the scanning speed in x-axis and y-axis as V_x and V_y respectively. Apparently, V_x is much bigger than V_y. Second, we define a constant thermal drift speed as T_x and T_y. Third, our sample has an orthorhombic lattice structure, and the lattice constants are a and b, with a slightly different with b. Fourth, we will successively get two pairs of images which are scan-up-forward/-backward and scan-down-forward/-backward images. Notice that the V_x and V_y are known in STM scanning software, and T_x and T_y are unknown parameters. The lattice constant will be measured from Fourier transform STM images.

We start from a simple case. We assume the thermal drift is only along y direction, T_x=0, $T_y \neq 0$. We are scanning along crystal axis direction. So the possible scan-up and scan down images are shown in Fig. A.1b and A.1c compared to perfect lattice in Fig. A.1a.

So basically we can measure the distorted lattice spacing from Fig. A.1b and A.1c. Let me assign the sign of $\uparrow$, $\downarrow$, $\rightarrow$, $\leftarrow$ as a scan up, scan down, forward, and backward, respectively.

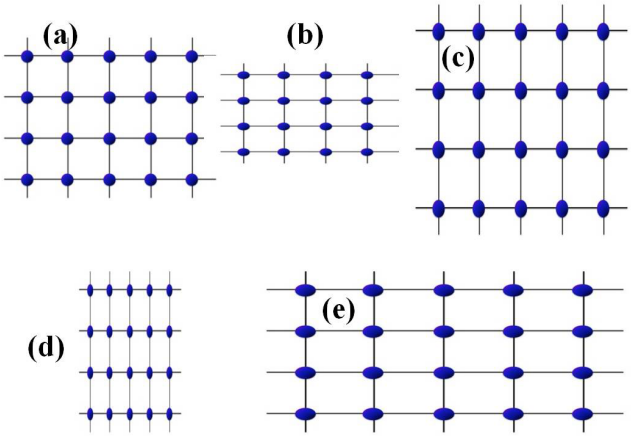

FIGURE A.1. (a) A schematic view of (a) a perfect lattice and distorted lattice when (b) scan-up (c) scan-down (d) scan-forward (e) scan-backward.

If we get the lattice constant in x-axis in forward and backward images are the same, then we can tell that the assumption of no thermal drift in x-axis is true. Actually, in reality, we always get the same lattice spacing in x-axis even with thermal drift of x-axis because the V_x is always much bigger than T_x. So we will get:

$$a = a_{\rightarrow} = a_{\leftarrow} \tag{6.2}$$

While in y direction, the case of that V_y is comparable with T_y is very common in STM scanning. So calculations need to done along y axis.

$$\frac{1}{b_{\uparrow}} = \frac{1}{b} \times (1 - \frac{T_y}{V_y}) \tag{6.3}$$

$$\frac{1}{b_{\downarrow}} = \frac{1}{b} \times (1 + \frac{T_y}{V_y}) \tag{6.4}$$

So we will get

$$b = \frac{2 \times b_{\uparrow} \times b_{\downarrow}}{b_{\uparrow} + b_{\downarrow}} \tag{6.5}$$

If T_x is comparable with V_x, which is very rare, the situation will be like Fig. A.1d and A.1e. However, the problem remains the same with y-axis. So we will get:

$$a = \frac{2 \times a_{\leftarrow} \times a_{\rightarrow}}{a_{\leftarrow} + a_{\rightarrow}} \tag{6.6}$$

Then we are able to tell the precise parameters from distorted images due to the thermal drift. However, that is the simplest case. The next question will be that if we did not scan along crystal axis directions, how we tell the precise lattice parameters from distorted image. So first of all, let us assume a perfect lattice with thermal drift as in Fig. A.2a, the distorted scan-up and -down images are shown in Fig. A.2b and A.1c respectively.

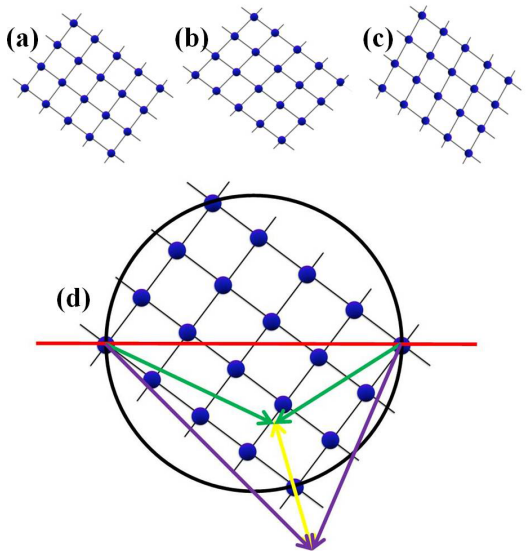

FIGURE A.2. A schematic view of (a) a perfect lattice and distorted lattice when (b) scan-up (c) scan-down. (d) demonstration of the angles of the lattice in scan-up and scan-down STM images.

The first question we are going to ask is how we know the angles between a-axis and a-axis are 90° just based on measurements from Fig. A.2b and Fig. A.2c. The answer is not clear. If we get one obtuse angle and one sharp angle, either in scan-up or -down images, it is hard to tell whether the angle is 90 degrees or not. However, if we get two obtuse angles or two sharp angles, then it is definitely not 90°. The reason can be illustrated as following Fig. A.2d.

The red line is the horizontal line which is the scanning x-axis. The yellow arrows indicate the thermal drift vectors, the one point into or out the black circle can either the scan-up or scan-down thermal drift vector. So if the lattice angle is 90°, the scan-up and scan-down images will give an obtuse angle and a sharp angle. It is important to notice that this explanation is based on $V_x \gg T_x$ which is the common case in scanning. The next problem will be how to get precise a and b. Now we have to turn to mathematically calculations. This calculation will involve lots of angles which will make it complicated. We need to use math software to compute to solve several equations. In reality, we are always able to follow the crystal axis to scan, or rotate the scanning directions. Another method will be direct measuring the thermal drift based on two successive scans. So T_x and T_y will be known. However, in experiments, we cannot guarantee that we will get the chance to rotate the scanning direction or direct measuring thermal drift. We will have to follow above discussion to take out the thermal drift.

Appendix B: Work function measurement

In surface science, the work function is the minimum energy needed to remove one electron from the surface to the vacuum. It is close related to the fermi energy of the system but it is not the same due to the surface effect. For instance, a electron also need energy to overcome the energy barrier of effective surface dipole. Thus, the work function of a surface do not simply equal to the work function of the element. A theoretical calculation with correct surface structure is needed to determine the work function of a surface.

Experimentally, STM *dI/dZ* curve offers a way to measure the apparent barrier height, which is intimately related to the work function of a surface. The details are presented in Chapter 2. However, the apparent barrier height measurement is sensitive to the tunneling junction, which includes the element of the tip atoms, the geometric configuration of tip, the tip-surface angle, the surface geometric structure, and the surface electronic structure.

In an attempt to determine the surface termination layer of surface phases in $Pr_xCa_{1-x}Fe_2As_2$, a comparison of work functions is done by Zeljkovic *et al* [1]. They mapped the apparent barrier heights of (1×2) and (1×1) phase with the same tunneling junction in one STM image scanning of the interface. The (1×2) surface has relative smaller apparent barrier height thus it is associated to Ca-terminated surface because of the smaller work function of element Ca, see Table B.1. In chapter 5, we described that Massee et al [2] found a work function of 1.5 eV at both $(\sqrt{2}\times\sqrt{2})$R45° and (1×2) phase, suggesting the same termination layer in the Co-doped $BaFe_2As_2$ compounds. Note that the work function from DFT calculation on $BaFe_2As_2$ [3] for the stripe phase, if with a half-Ba terminated model as our

chapter 4 discussed, is 1.56 eV. Thus, the $(\sqrt{2}\times\sqrt{2})$R45° is the half-Ba terminated surface.

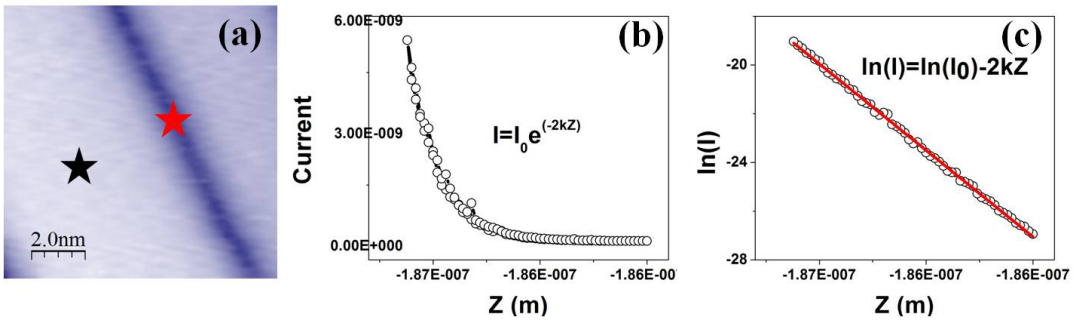

FIGURE B.1. Work function measurement by STM at the surface of $CaFe_2As_2$ stripe phase. (a) The measurements are done at two locations where stars located. (b) & (c) The experiments data of exponential relationship of the current with the tip sample distance z for the stripe surface.

Here we present our work function measurement on the stripe phase of $CaFe_2As_2$. We used a tungsten tip and measured the work function at two locations: one is the black star at the clean stripe surface while the other is the red star at the missing Ca atoms line. Using Equation 2.17 with slope derived from the fitting in Fig. B.1, we can get the apparent barrier height. After subtracting the tungsten work function of 4.5 eV and considering the bias in Eq.2.18, the work function of the stripe phase is estimated to (1 ± 0.3)eV while the missing lines has a little bit higher work function of(1.5 ± 0.6)eV. Table B.1 has summarized the work function of different phases both by experiments and DFT calcuation. The work functions we measured are smaller than the theoretical value (2.45 eV) for stripe Ca layer by DFT calculation (See table B.1). Especially it is far smaller than work function of As-terminated surface (4.97 eV). As discussed previously, the measurement is sensitive on the tunneling junction. Our measurements on $CaFe_2As_2$ with a smaller magnitude of the work function is possible, for example, due to a deviation from

90° on the tip-surface angle. Thus, we believe our work function measurement is consistent with half-Ca terminated stripe surface.

TABLE B.1. Work function of elements (adapted from reference [4]) and surface phases at (Ba, Ca)Fe_2As_2.

Element	ϕ(eV)	Element	ϕ(eV)	Element	ϕ(eV)
Ba	2.52	Fe	4.67-4.81	Ir	5.42-5.67
Ca	2.87	Te	4.95	Pt	5.12-5.93
As	3.75	Se	5.9	W	4.32-5.22
Phase	ϕ(eV)-DFT	ϕ(eV)-STM	Phase	ϕ(eV)-DFT	ϕ(eV)-STM
0.5ML-Ba	1.56(1.35)	∼1.5[2]	0.5ML-Ca	2.45	1.0
1ML-Ba	2.8[3]		1ML-Ca	2.69	
1ML-As	4.97				

[1] Ilija Zeljkovic, Dennis Huang, Can-Li Song, Bing Lv, Ching-Wu Chu, and J. E. Hoffman, ArXiv 1301.4942v1 (2013).

[2] F. Massee, Ph.D thesis, University of Amsterdam, 2011.

[3] G. Profeta, C. Franchini, K. A. I. L. W. Gamalath, and A. Continenza, Physical Review B 82 (2010).

[4] C. R. Hammond, THE ELEMENTS, IN HANDBOOK OF CHEMISTRY AND PHYSICS (CRC press, 2004).

Appendix C: LEED I-V analysis of (1×1) phase

Because of the low Debye temperature, the top ordered Ba surface may become disorder,exposing an ordered As layer. Indeed, the room temperature cleavage or after the irreversible fade out of the fractional spots, the LEED pattern shows (1×1) pattern, for example, see Fig. 5.6a for Ba122 in Chapter 5 and Fig. 4.4 for Ca122 in Chapter 4. If we assume that the $\sqrt{2}\times\sqrt{2})R45^o$ or (1×2) phase all become disorder, the I-V curves of the integer spots may reflect the structure of As-terminated surface after the top Ba layer becomes disorder. Thus, we conducted LEED I-V analysis on the integer spots of both (1×1)patterns from Ba122 and Ca122, shown in Fig. C.1 and Fig. C.2, respectively.

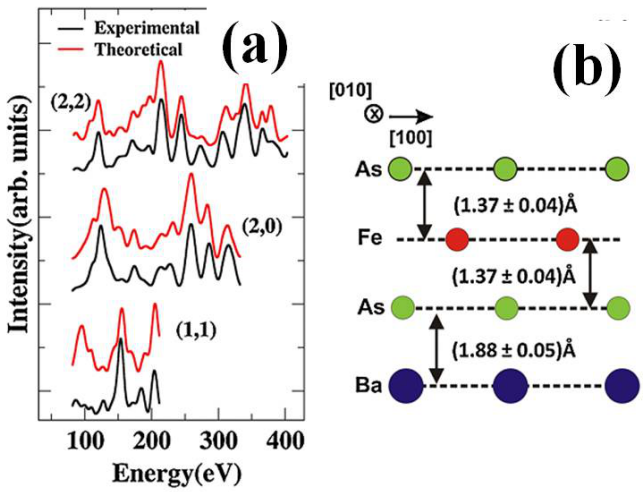

FIGURE C.1. (a) The measured I(V) curves of the diffracted beams (1,1), (2,0), and (2,2) from Fig. 5.6a compared with the theoretical ones for the final As terminated surface structure. (c) The (001) surface structure obtained from LEED structural analysis. The bulk As-Fe and As-Ba interlayer distances are 1.3437$\mathring{A}$. Figures are adapted from reference [1].

Full monolayer of As-terminated model works well, i. e. the R_p is 0.24 for Ba122 and 0.34 for Ca122. We could not get Rp factor lower than 0.5 for Ba/Ca terminated (1×1) phase. Both calculations show that the surface after the disappearance

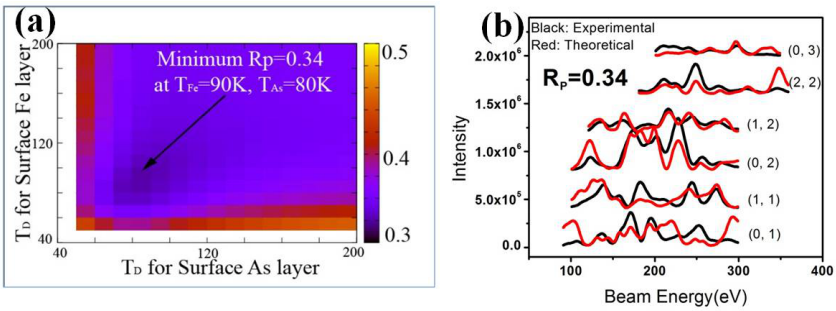

FIGURE C.2. With a As-termination model, (a) The grid of Rp factor with Debye temperature for top Fe layer as y axis and Debye temperature for top As layer as x axis. The color bar on the right represents the value of R_p. As indicated by black arrow, there is a minimum of R_p with optimized Debye temperature (T_{Fe}, T_{As})=(90 K, 80 K). (b) Comparison of theoretical I-V curves (red color) to experimental I-V curves (black color) for the optimized Debye temperature.

of fractional spots, is a bulk truncated As-terminated surface. The refined thickness (2×1.37 $\mathring{A}$) of the As-Fe_2-As tri-layer in Ba122 is slightly larger than that (2×1.34 $\mathring{A}$) in the bulk, suggesting a possible small surface relaxation, but no reconstruction of the As surface.

For Ca122, the mapping of R_p with As-termination is shown in Fig. C.2a with the minimum R_p indicating the optimized Debye temperature. For top As layer, Debye temperature is 80K while top Fe layer is 90 K. It is consistent with our expectation that the surface has low Debye temperature. Figure C.2b shows the comparison between the experimental curves and theoretical calculations. The surface is a As-terminated surface without any buckling or compressing within error ~ 0.05 $\mathring{A}$. Although $R_p = 0.34$ is slightly higher than a good fit, considering the fact that we have such complex surface and the surface have also suffered two thermal cycles, the results were acceptable. Last, the LEED I-V analysis on $SrFe_2As_2$ exhibit similar conclusion [2]. Thus, we concluded that the surface can turn to As-terminated (1×1) phase after removing the superlattice order through external perturbation.

[1] V. B. Nascimento, et al., Physical Review Letters 103 (2009).

[2] F. C. Niestemski, Von Braun Nascimento, Biao Hu, Ward Plummer, J. Gillett, Suchitra Sebastian, Ziqiang Wang, and V. Madhavan, ArXiv 0906.2761 (2009).

Vita

Guorong Li was born in August 1984, in a small village near MiLuo river or the famous Dongting Lake in MiLuo city, Hunan province, China. He finished his undergraduate studies in physics from Peking University in China in July 2007. In August 2007, he came to University of Tennessee at Knoxville to pursue graduate studies in condensed matter physics under the supervise of Dr. Ward Plummer. In October 2008, Dr. Ward Plummer joined Louisiana State University (LSU) to develop materials science efforts thus Guorong Li also moved to LSU in December 2008 to continue his graduate studies. He is currently a candidate for the degree of Doctor of Philosophy in physics, which will be awarded in August 2013.